

7-2-2020

Structure Function Relationship in Hexacoordinate Heme Proteins: Mechanism of Globin X Interactions with Exogenous Ligands and Ligand Accessibility in Cytoglobin and Neuroglobin

Ruipeng Lei
rlei001@fiu.edu

Follow this and additional works at: <https://digitalcommons.fiu.edu/etd>



Part of the [Biochemistry Commons](#), and the [Biophysics Commons](#)

Recommended Citation

Lei, Ruipeng, "Structure Function Relationship in Hexacoordinate Heme Proteins: Mechanism of Globin X Interactions with Exogenous Ligands and Ligand Accessibility in Cytoglobin and Neuroglobin" (2020). *FIU Electronic Theses and Dissertations*. 4470.
<https://digitalcommons.fiu.edu/etd/4470>

This work is brought to you for free and open access by the University Graduate School at FIU Digital Commons. It has been accepted for inclusion in FIU Electronic Theses and Dissertations by an authorized administrator of FIU Digital Commons. For more information, please contact dcc@fiu.edu.

FLORIDA INTERNATIONAL UNIVERSITY

Miami, Florida

STRUCTURE-FUNCTION RELATIONSHIPS IN HEXACOORDINATE
HEME PROTEINS: MECHANISM OF GLOBIN X INTERACTIONS WITH
EXOGENOUS LIGANDS AND LIGAND ACCESSIBILITY IN CYTOGLOBIN
AND NEUROGLOBIN

A dissertation submitted in partial fulfillment of the

requirements for the degree of

DOCTOR OF PHILOSOPHY

in

BIOCHEMISTRY

by

Ruipeng Lei

2020

To: Dean Michael R. Heithaus
College of Arts, Sciences and Education

This dissertation, written by Ruipeng Lei, and entitled Structure-Function Relationships in Hexacoordinate Heme Proteins: Mechanism of Globin X Interactions with Exogenous Ligands and Ligand Accessibility in Cytoglobin and Neuroglobin, having been approved in respect to style and intellectual content, is referred to you for your judgement.

We have read this dissertation and recommend that it be approved.

Yuk-Ching Tse-Dinh

Irina Agoulnik

Xiaotang Wang

Jaroslava Miksovska, Major Professor

Date of Defense: July 2, 2020

The dissertation of Ruipeng Lei is approved.

Dean Michael R. Heithaus
College of Arts, Sciences and Education

Andrés G. Gil
Vice President for Research and Economic Development
and Dean of the University Graduate School

© Copyright 2020 by Ruipeng Lei

All rights reserved.

DEDICATION

I dedicate this work to my parents. Without their patience,
understanding, support, and selfless love,
the completion of this work would not have been possible.

ACKNOWLEDGMENTS

I would like to express my gratitude to my major Professor, Dr. Jaroslava Miksovska, for giving me the opportunity to join her lab and to work on this project, for providing me with knowledge and techniques to pursue my project, and for encouraging independent study and professional development. I greatly appreciate all her mentoring and encouragement to let me present my work on several national and international conferences which I believe has greatly expand my horizon in the field of scientific research.

I would like to thank my committee members, Dr. Yuk-Ching Tse-Dinh, Dr. Irina Agoulnik, and Dr. Wang, for taking time to provide me with insightful suggestions to improve my research as well as generous support to continue and finish my Ph.D. career steadfast.

I wish to thank my former and current lab mates-Dr. Antonija Tanger, Dr. Khoa Pham, Dr. David Butcher, Dr. Walter Gonzalez, Maria Santiago, and Setareh Sakhdari, for their dedications, support and great times in the lab. In particular, I would like to thank all the undergraduate students who work with me, Maria Jose Santiago, Manuel Picon and Isa Sabir, for their contributions to both published and unpublished results.

I especially appreciate my family for all their encouragement and support during all these years. I am indebted to my parents for all their unconditional love, dedication and sacrifice to give me the best education to their most, which makes me fearless and energetic in pursuing the career I like.

I will also give special thanks to my wife Li Mo. Without her help, love and encouragement to keep me moving forward, I can't make it so far.

I also would like to thank the Department of Chemistry and Biochemistry at FIU for accepting me into their graduate program, and for their financial support as Teaching Assistant. In addition, I would like to acknowledge the financial support provided by FIU graduate school for the Dissertation Year Fellowship, which greatly helped me preparing for my graduation.

ABSTRACT OF THE DISSERTATION

STRUCTURE-FUNCTION RELATIONSHIPS IN HEXACOORDINATE
HEME PROTEINS: MECHANISM OF GLOBIN X INTERACTIONS WITH
EXOGENOUS LIGANDS AND LIGAND ACCESSIBILITY IN CYTOGLOBIN
AND NEUROGLOBIN

by

Ruipeng Lei

Florida International University, 2020

Miami, Florida

Professor Jaroslava Miksovska, Major Professor

Cytoglobin (Cygb), neuroglobin (Ngb), and globin X (GbX) belongs to recently discovered members of the vertebrate globin family, they carry a heme prosthetic group that can reversibly bind exogenous ligands such as CO, NO and O₂. Although the physiological functions of Cygb, Ngb and GbX are still under debate, several possible physiological functions for these proteins were proposed. Cytoglobin was reported to participate in lipid-based signaling and to stabilize the tumor suppressor p53 upon DNA damage, which imply its anti-cancer role. Neuroglobin was shown to interact with α -subunit of the heterotrimeric G protein as well as cytochrome c which indicate a role in cell apoptosis. Both proteins were also proposed to participate in NO metabolism. Compared to the well-known vertebrate globin, hemoglobin and myoglobin, the new members have several distinct structural characteristics. First, unlike Hb and Mb, the

distal histidine coordinates with the heme iron at the sixth axial position in Cygb, Ngb and GbX, forming a hexa-coordinated heme iron and thus regulating kinetics and equilibrium constants for exogenous ligand binding to heme. Second, an oxidation/reduction of an intramolecular disulfide bridge which is found in all three hexa-coordinated globins, also modulates affinity for diatomic ligands such as O₂ and CO. Additionally, both Cygb and GbX are found to have extended N- and C- terminals with unclear function, although the N-terminal in GbX is proposed to be involved in the protein binding to the membrane.

The work presented in this dissertation focuses on investigation of the role of internal ligand (distal histidine) and disulfide bridge on structure-function relationships in GbX, in terms of regulating affinity and kinetics for small diatomic ligands. Indeed, we have shown a very weak ligand binding to heme iron in GbX, suggesting its distinct role among hexa-coordinated vertebrate globins. In addition, the study of conformational dynamics that affect the heme cavity accessibility of Cygb and Ngb by incorporating heme fluorescent analog ZnPPiX into the protein is also performed. These data show a high conformational heterogeneity of the distal pocket in hexa-coordinated globins as well as increased accessibility of the heme pocket in Ngb.

TABLE OF CONTENTS

CHAPTER		PAGE
1	INTRODUCTION	1
1.1	Metallo-porphyrin and Heme proteins	1
1.2	Globin: Hemoglobin and Myoglobin.....	2
1.3	Novel vertebrate globins	5
1.4	Neuroglobin and Cytochrome b5.....	7
1.5	GbX: a membrane-bound vertebrate globin	11
1.6	Heme coordination.....	13
1.7	Disulfide bridge modulate protein-ligand interaction and protein stability.	14
1.8	Distal histidine: gate of the distal pocket.....	16
1.9	Extended N- and C-terminals.....	18
1.10	Heme disorder and sliding.	19
1.11.	Globin interactions with exogenous ligands	21
2	OBJECTIVES	23
3	MATERIAL AND METHODS.....	25
3.1	Materials	25
3.2	Methods.....	25
3.2.1	Protein expression and purification.	25
3.2.1.1	Neuroglobin and Cytochrome b5 isolation and purification.	25
3.2.1.2	Globin X isolation and purification	26
3.2.2	Sodium dodecyl sulfate electrophoresis.....	27
3.2.3	UV-vis Spectroscopy.....	29
3.2.4	Circular Dichroism.....	31
3.2.5	Transient absorption spectroscopy.....	34
3.2.5.1	Introduction.....	34
3.2.5.2	TA set up	36
3.2.5.3	TA sample preparation	37
3.2.6	Photoacoustic calorimetry (PAC).....	42
3.2.6.1	Introduction.....	42
3.2.6.2	PAC set up.....	44
3.2.6.3	Quantum yield determination	45
3.2.6.4	PAC data analysis.....	46
3.2.7	Stability studies.....	50
3.2.8	Cyanide affinity test.....	51
3.3	Methods: Chapter 2.....	52
3.3.1	Preparation of ZnPPIX reconstituted hexacoordinate globin	52
3.3.2	Fluorescence spectroscopy.....	53

3.3.2.1	Steady-state fluorescence spectroscopy	54
3.3.2.2	Steady-state frequency-domain fluorescence lifetime	55
3.3.2.3	Time-resolved fluorescence lifetime measurement	57
3.3.3	Phosphorescence	57
3.3.3.1	Phosphorescence measurement.....	58
4	IMPACT OF THE DISULFID BRIDGE AND DISTAL HISTIDINE ON LIGAND MIGRATION IN GLOBIN X.....	59
4.1	Introduction.....	59
4.2	Result	61
4.2.1	Oligomerization state of purified GbX	61
4.2.2	Steady-state UV-vis spectra and far-UV CD spectra	63
4.2.3	Stability of GbX towards pH unfolding.....	65
4.2.4	CN ⁻ binding to GbX.....	68
4.2.5	GbX CO binding kinetic	70
4.2.6	CO dissociation from GbX	77
4.3	Discussion.....	83
5	CHARACTERIZATION OF THE CONFORMATION, REGULATION, ORIENTATION, AND HEME ACCESIBILITY IN HEXACOORDINATE GLOBINS BY USING FLUORESCENT HEME ANALOG.	86
5.1	Introduction.....	86
5.2	Results.....	88
5.2.1	Steady-state UV-vis absorption spectroscopy	88
5.2.2	Steady-state fluorescence emission spectra	90
5.2.3	Fluorescence and phosphorescence lifetime	92
5.2.4	Quenching study	96
5.3	Discussion	100
5.4	Summary	104
6	THE O ₂ BINGING KINETIC AND IMPACT ON HEME CAVITY STABILITY IN GLOBIN X.	106
6.1	Introduction.....	106
6.2	Result	108
6.2.1	Steady-state UV-vis spectra	108
6.2.2	Stability of O ₂ bound GbX towards pH unfolding.....	109
6.2.3	GbX O ₂ binding kinetic	111
6.2.4	Photoacoustic calorimetry result of O ₂ dissociation	113
6.3	Discussion.....	116

SUMMARY	119
LIST OF REFERENCES	120
VITA	138

LIST OF TABLES

TABLE	PAGE
Table 3.1. Ingredient of 1L 10X SDS running buffer for electrophoresis.	28
Table 3.2. Ingredient of loading buffer for electrophoresis.	28
Table 3.3. Ingredient of Coomassie blue staining buffer.	29
Table 3.4. Ingredient of de-staining buffer.....	29
Table 3.5. The electromagnetic spectrum (Worsfold & Zagatto, 2005).....	30
Table 3.6. The visible spectrum (Worsfold & Zagatto, 2005).	31
Table 4.1 UV-vis absorption spectra wavelength of Soret and α/β band of each GbX variants.....	64
Table 4.2. Parameters of the pH-induced GbX variants unfolding (* (Picotti et al., 2009)).....	68
Table 4.4. Rate constants for CO binding to GbX variants obtained by fitting the experimental data by exponential decay model and MEM analysis at 20°C. (* (Belogortseva et al., 2007), † (Butcher et al., 2017), ‡ (Astudillo et al., 2013))	72
Table 4.5. Activation energy, log pre-exponential factor, activation enthalpy, and activation entropy of temperature dependent CO rebinding to GbX variants. (* (Butcher et al., 2017), † (Mikšovská et al., 2003)).....	73
Table 4.6. Rate and equilibrium constants for CO binding to GbX variants.	

(#(Rohlfis et al., 1990), *(Smaghe et al., 2006))75

Table 4.7. Reaction (ΔH and ΔV) and activation (ΔH^\ddagger and ΔV^\ddagger) parameters associated with the photo-dissociation of Fe-CO bond and subsequent ligand escape from the protein matrix in GbX variants. (*(Astudillo et al., 2013)).....80

Table 4.8. Total volume and enthalpy changes associated with the CO dissociation from GbX variants as well as Cygb, Ngb, Mb, and Hb. (*(Astudillo et al., 2013), †(Peters et al., 1992)).....82

Table 5.1. Summary of UV-vis absorption maxima for ZnPPIX reconstituted hhMb, Cygb and Ngb variants. Specifically, CygbR84L shown a shoulder rather than a peak at ~ 595 nm.....90

Table 5.2. Summary of fluorescence emission maxima for ZnPPIX reconstituted hhMb, Cygb and Ngb variants.92

Table 5.3. Summary of fluorescence and phosphorescence parameters of ZnPPIX-reconstituted hexacoordinate globins.....93

Table 5.4. Summary of Stern-Volmer constant of ZnPPIX-reconstituted hexacoordinate globins.98

Table 5.5. Summary of quenching rate constant of ZnPPIX-reconstituted globins... 100

Table 6.1. Absorption spectra wavelength of Soret and Q-band of GbX WT and C64A mutant summarized in the table..... 108

Table 6.2. Parameters of the acid-induced oxygen bound GbX variants unfolding. . 111

Table 6.3. Rate constants for O₂ binding to GbX variants obtained using both

exponential decay model and MEM analysis at 20°C. 112

Table 6.4. Activation energy, log pre-exponential factor, activation enthalpy, and activation entropy of temperature dependent O₂ rebinding to GbX variants..... 113

Table 6.5. Thermodynamic parameters associated with O₂ photo-dissociation from GbXWT and GbXC65A. (*(Astudillo, 2014)) 116

LIST OF FIGURES

FIGURE	PAGE
<p>Figure 1.1. Examples of metallo-porphyrins. (A) iron protoporphyrin IX. (B) zinc protoporphyrin IX. (C) magnesium protoporphyrin IX. (D) copper protoporphyrin IX.</p>	2
<p>Figure 1.2 Ribbon representation of the three-dimensional structure of horse heart Hb with α subunits in yellow and β subunits in pink (left, PDB entry: 2HHB) and sperm whale myoglobin (right PDB entry: 1A6N,). The, heme group is shown in red.</p>	4
<p>Figure 1.3. Simplified phylogenetic relationships in vertebrate globins by using uniprot database along with their coordination type (GbY is yet determined).....</p>	6
<p>Figure 1.4. Ribbon representation of human neuroglobin (left, PDB: 4MPM chain A) and cytoglobin (right, remodeled by PDB: 2DC3). The proximal and distal histidine is shown in sticks, the heme is shown in red, two cysteine residues are in orange. The cytoglobin extended N terminal is shown in yellow and C terminal is shown in gray.</p>	7
<p>Figure 1.5. GbX sequence alignment with vertebrate globins and predicted secondary structures. Highly conserved amino acid residues are labeled with blue shadows.....</p>	11
<p>Figure 1.6. Ribbon representation of the heme binding site in vertebrate Mb (left, PDB entry 1A6N), Ngb (right, PDB entry 4MPM) demonstrating penta-coordination and hexa-coordination respectively, of the heme iron. The distal (magenta) and proximal (green) histidine residues are shown as sticks.....</p>	13
<p>Figure 1.7. The heme orientations in Mb (A) and rotated 180° about the α-γ-meso axis (B). The heme substituents are labeled M (methyl), V (vinyl), and P</p>	

(propionate) (Xu, Li, et al., 2009).....20

Figure 1.8. Heme sliding upon CO binding. Ferric murine Ngb (in green, PDB: 5EET), CO bound murine Ngb (in cyan, PDB: 1W92). Distal and proximal histidine, heme group as well as Phe-106 are also shown as sticks.....21

Figure 3.6. Sample electronic CD spectra of protein in α -helix, a β -sheet and a random coil. Simulated by PDBMD2CD.com with data from protein data bank.32

Figure 3.7. In transient absorption spectroscopy, time profiles of absorption changes that are associated with ligand binding/dissociation from proteins are measured. (A) Absorption spectrum of deoxy- and CO-GbX in the UV and visible (inset) region. (B) Simplified reaction diagram of CO photodissociation and rebinding to swMb. (C) Time resolved absorption trace for CO recombination to GbX on microsecond to millisecond timescale.....34

Figure 3.8. Top-view schematic of the transient absorption apparatus. TA components: the sample (red), temperature-controlled cuvette holder (TC), mirrors, pump beam (Nd:YAG532), beam blocker (B), lenses, probe beam (Xe lamp), monochromator (MC), photodiode (D) and Digitizer. Dashed line indicates pulsed light.36

Figure 3.9. Contour plots of the statistic parameter χ^2 and the entropy S for a two dimensional $f(\lambda)$. The maximum entropy solution equivalent to the point where the gradient of χ^2 is parallel to the gradient of S, where χ^2 is close to 1. Modified from Steinbach et al. (Steinbach et al., 1992).....38

Figure 3.10. An energy diagram for CO binding to Mb.42

Figure 3.11. Schematic diagram of a home-build PAC instrument setup (top view). .43

Figure 3.12. Schematic diagram of wave propagation from the sample to the

detector in PAC measurements.	44
Figure 3.13. Illustrative PAC acoustic traces for sample and reference compound. ...	47
Figure 3.14. Illustrative PAC acoustic traces for the sample acoustic trace is shifted in phase compare to the reference trace.	50
Figure 3.15. Simplified Jablonski diagram represent electronic transitions between different electronic states. A as absorption, IC as internal conversion, ISC as intersystem crossing, F as fluorescence, NR as nonradiative decay, P as phosphorescence, S as singlet state, T as triplet state.	53
Figure 3.16. The modulation of emission (red) is decreased by modulation of excitation light intensity (black) and result in phase shift. The dash line indicated average intensity for both waves. The modulation ratio (m) is determined by the amplitude of the average intensity (a, A) and the offset from the average intensity (b, B) of emission and excitation.	55
Figure 3.17. Phase delay (ϕ_ω) and modulation ratio (m) versus modulation frequency (ω) for POPOP reference compound.	57
Figure 4.1. SDS-PAGE gel for purified GbX variants in the presence/absence of β -me. B, SDS-PAGE gel for GbXWT fractions after separation of monomer and dimer using size exclusion chromatography.	62
Figure 4.2. Absorbance spectra of the oxidized (met), reduced (ferrous deoxy), and CO bound forms of GbX variants.	63
Figure 4.3. CD spectra in the far-UV region of GbX variants. All samples are aligned at Abs ₂₈₀ nm.	65
Figure 4.4. Acid-induced unfolding of GbXWT UV-vis absorption spectra.	

Measurements were performed in 5 mM phosphate-citrate buffer and 100 mM NaCl, under equilibrium conditions.....66

Figure 4.5. Acid-induced GbX variants unfolding. The solid line corresponds to the experimental data using Eq. 3.36. Measurements were performed in 5 mM phosphate-citrate buffer and 100 mM NaCl, under equilibrium conditions.....67

Figure 4.6. A, absorption difference spectra at various cyanide concentrations, relative to the ferric GbX form (without cyanide), the spectra were measured at room temperature in 50 mM TrisHCl at pH 7. B, cyanide binding to GbX variants, fraction bound was calculated by absorption at 410 nm as a function of cyanide concentration, only cysteine mutant shows possible two binding sites.69

Table 4.3. Parameters of the CN^- binding to GbX variants (\dagger (Tsujino et al., 2014), \ddagger (Dou et al., 1996)).....70

Figure 4.7. A, transient absorption traces for CO rebinding to GbX variants. B, Lifetime distribution associated with the CO rebinding to GbX variant determined by MEM approach. C, Arrhenius plot of temperature dependent CO rebinding to GbX variants, color represent different rate constant (black k1, red k2, blue k3, and purple k4) and symbol represent different GbX variants (square WT, round C65A, and triangle H90V). D, Eyring plot of temperature dependent CO rebinding to GbX variants.....71

Figure 4.8. Logarithmic plots of the rate constants for CO rebinding to GbXWT (A), GbXC65A (B), and GbXH90V (C) as a function of CO concentration, experiment was performed by 20 μ M protein in 50mM TrisHCl, pH 7, at 25°C.....74

Figure 4.9. CO quantum yield for bimolecular dissociation from GbX variants as a function of temperature.....77

Figure 4.10. Overlay of normalized acoustic traces of CO bound GbX variants with

reference.....78

Figure 4.11. Arrhenius (left) and Eyring (right) plot of slow phase for CO photo-dissociation from GbXWT and C65A mutant.79

Figure 4.12. Plot of $\phi_i E_{hv}$ versus $C_p\rho/\beta$ for the prompt phase (left) and the slow phase (right) for CO photo-dissociation from GbX variants.80

Figure 5.1. Normalized steady-state absorption spectra of ZnPPIX-hhMb and ZnPPIX-Cygb variants (A) and ZnPPIX-Ngb variants (B) in 50 mM TrisHCl pH 7.0.....89

Figure 5.1. Normalized steady-state fluorescence emission of ZnPPIX-Cygb variants (A) and ZnPPIX-Ngb variants (B), using $\lambda_{exc}= 421$ nm.....91

Figure 5.3. Time-resolved fluorescence in the frequency domain data determined for ZnPPIX-Cygb variants (A) and ZnPPIX-Ngb variants (B).93

Figure 5.4. Time-resolved fluorescence in the frequency domain data determined for ZnPPIX-Cygb variants (A) and ZnPPIX-Ngb variants (B).95

Figure 5.5. Phosphorescence decay determined for reconstituted globins. Phosphorescence decay was monitored at 447 nm.95

Figure 5.6. Example of UV-vis absorption spectra of ZnPPIX reconstituted protein with increasing concentration of methyl viologen. A decrease of Soret band absorbance is observed.96

Figure 5.7. Example of fluorescence emission spectra of ZnPPIX reconstituted

protein in the presence of increasing concentration of methyl viologen.97

Figure 5.8. The Stern-Volmer plot for the quenching of the steady-state fluorescence of ZnPPIX reconstituted globins by methyl viologen.....98

Figure 5.9. Triplet state lifetime traces of ZnPPIX-hhMb obtained by transient absorbance at varying concentration of oxygen. All traces are fitted by single exponential decay.....99

Figure 5.10. The Stern-Volmer plot for the quenching of the triplet-state phosphorescence of ZnPPIX reconstituted hhM by oxygen.....99

Figure 6.1. Absorption spectra of the oxidized (met), reduced (ferrous deoxy), and O₂ bound forms of GbX WT and C65A mutant. Measured in 50 mM TrisHCl pH 7.0..... 108

Figure 6.2. UV-vis absorption spectra of GBXWT in the oxygen bound form as function of pH. Measurements were performed in 5 mM phosphate-citrate buffer and 100 mM NaCl, under equilibrium conditions. 109

Figure 6.3. Fraction unfolding of oxygen bound GbX WT and C65A mutant plot as a function of pH. 110

Figure 6.4. A, transient absorption traces for O₂ rebinding to GbX variants. B, Lifetime distribution associated with the O₂ rebinding to GbX variant determined by MEM approach. C, Arrhenius plot of temperature dependent O₂ rebinding to GbX variants. D, Eyring plot of temperature dependent O₂ rebinding to GbX variants..... 111

Figure 6.5 Quantum yield of O₂ from GbXWT and C65A plot as a function of

temperature. 114

Figure 6.6 Photoacoustic traces for oxygen dissociation from GbXWT (left) and GbXC65A (right) together with the trace for the reference compound 4SP. Conditions: 20 μ M protein in 50 mM Tris buffer (pH 7.0). The absorbance of the reference compound is aligned with the absorbance of the sample at 532 nm. 114

Figure 6.7. Plot of ϕE_{hv} as a function of C_{pp}/β for O₂ photo-release from GbXWT (black), and GbXC65A (red). The associated volume and enthalpy changes were obtained from the slope and intercept of the linear fits, respectively. 115

LIST OF ABBREVIATIONS AND ACRONYMS

ABBREVIATION	FULL NAME
AA	Amino acid
CO	Carbon monoxide
CygbWT	Cytoglobin wild-type
DTT	Dithiothreitol
FePPIX	Iron protoporphyrin IX
GbXWT	Globin X wild-type
Hb	Hemoglobin
hhMb	Horse heart myoglobin
ΔH	Enthalpy change
ΔH^\ddagger	Activation enthalpy change
K_d	Dissociation constant
Mb	Myoglobin
NaCN	Sodium cyanide
NgbWT	Neuroglobin wild-type
NO	Nitric oxide
O ₂	Oxygen
PAC	Photoacoustic calorimetry
ΔS	Entropy change

ΔS^\ddagger	Activation entropy change
TA	Transient absorption
ZnPPIX	Zinc protoporphyrin IX

1 INTRODUCTION

1.1 Metallo-porphyrin and Heme proteins

Metallo-porphyrins represent a diverse class of coordination complexes with a cyclic structure. They are often found as prosthetic groups in various proteins as they can catalyze a remarkable number of catalytic reactions and carrying additional functions such as an electron transport or ligand binding (figure 1.1)(Chandra et al., 2000; Larsen & Mikšovská, 2007). Among all the metallo-porphyrins, the iron-protoporphyrin IX (Heme b) is found in numerous proteins with distinct functions (Poulos, 2014). Heme b is a porphyrin derivative that is composed of four pyrrole rings linked by methine bridges with an iron coordinated to the nitrogen atom of the four pyrrole rings. The porphyrin ring has several substituents: four methyl groups, two propionate groups, and two vinyl substitutional groups. In heme proteins, heme b is incorporated into a protein matrix and stabilized through covalent, in case of cytochrome c, or noncovalent hydrophobic interactions between the prosthetic group and the amino acid residues. In addition, a coordination bond(s) between the heme iron and heteroatoms from amino acid sidechains contribute to the heme binding to the apoprotein (Voet & Voet, 2010).

Heme proteins are extraordinary versatile and perform various functions such as catalysis (catalases), peroxidases (horseradish peroxidase), respiratory functions like oxygen storage and transport (myoglobin and hemoglobin), electron transfer (cytochromes), and oxygen sensors (HemAT) (Larsen & Mikšovská, 2007). Although

the heme group is in the active center of the protein, its properties including catalytic functions are fine-tuned by the amino acid residues surrounding heme and/or by residues participating in a coordination bond with the heme iron (histidine, methionine, or tyrosine) or additional structural properties such as hydrogen bonds and salt bridges between the amino acid side chains in the heme pocket and the propionate groups of the heme impact the stability of the heme group as well as interactions with diatomic ligands. (Anderson & Chapman, 2005; Larsen & Mikšovská, 2007).

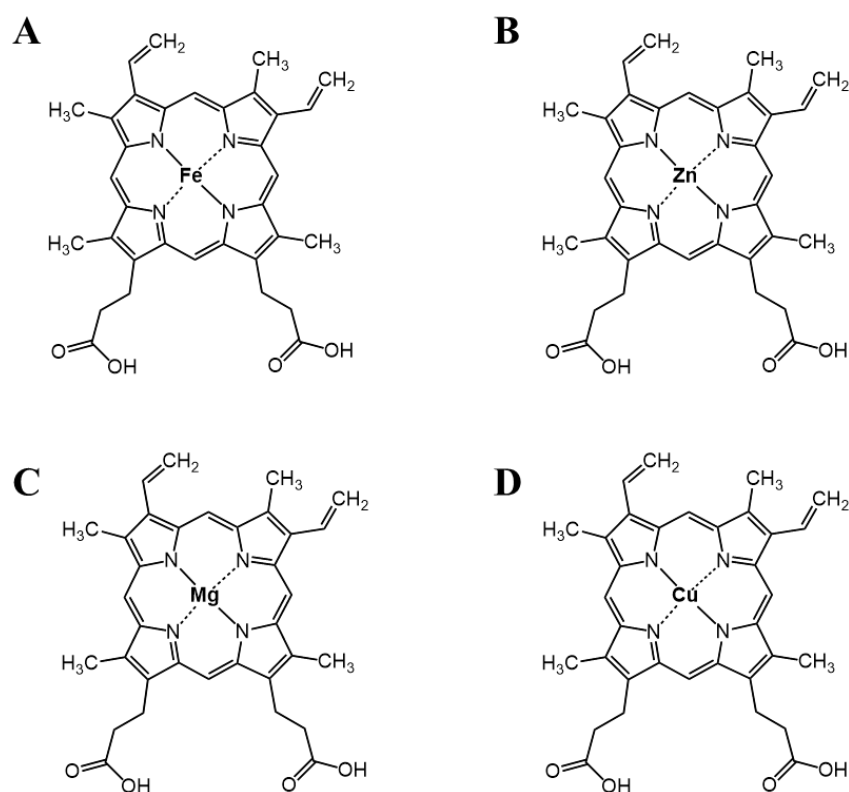


Figure 1.1. Examples of metallo-porphyrins. (A) iron protoporphyrin IX. (B) zinc protoporphyrin IX. (C) magnesium protoporphyrin IX. (D) copper protoporphyrin IX.

1.2 Globin: Hemoglobin and Myoglobin

Globins are a sub superfamily of the heme-proteins. They represent one of the most extensively studied group of proteins and serve as model for cooperative binding

and allosteric regulation as they reversibly bind small diatomic ligands such as CO, NO, and O₂ (Burmester & Hankeln, 2014). Most globins consist of eight α -helices (named A to H) with a typical 3-over-3 α -helical sandwich structure with the heme prosthetic group inside named globin fold. Globins was discovered in a variety of taxa, including bacteria, plants and animals. Among all the globins discovered to date, hemoglobin (Hb) and myoglobin (Mb) are the two globins that have been extensively studied and characterized (figure 1.2). Hemoglobin was discovered in 1840 by Friedrich Ludwig Hunefeld, and it is identified in different species—nearly all vertebrates, some invertebrates as well as some plants and fungi (Sheftel et al., 2011). In general, hemoglobin is a heterotetramer with a molecular weight of 65 kDa consisting of two different subunits α and β . The red color of the vertebrate blood is the result of the high concentration of Hb in the erythrocytes. The main function of hemoglobin is to transport O₂ from the respiratory surfaces (such as lungs, gills or skin) to the inner organs through the circulatory system (Voet & Voet, 2010). The reason why large or complex organisms need hemoglobin is because the diffusion rate of O₂ through tissue thicker than ~1 mm is too slow and the solubility of O₂ in blood plasma is too low to carry sufficient amounts of O₂ to support large life forms (Voet & Voet, 2010). Fortunately, with the help of hemoglobin, blood can carry O₂ at a concentration up to 0.01 M which is about the same concentration of O₂ in the air (Voet & Voet, 2010). Other than O₂ transportation, nitric oxide (NO) metabolism is another important aspect of vertebrate Hb function. In the oxygen bond form, hemoglobin can scavenge excess

of toxic NO and convert it to nitrate. In the deoxy form, hemoglobin can produce NO from nitrite reservoir which can initiate blood vessel dilatation during hypoxia (Burmester & Hankeln, 2014). Although the hemoglobin is functionally similar between different species, hemoglobins isolated from different species are structurally distinct and have different ligand binding cooperativity and allosteric regulation. Comparison of sequence/structure/function relationship among hemoglobins provides valuable information on how protein evolved to assist animal adaptation to physiologically challenging habitats such as high altitude or cold weather (Burmester & Hankeln, 2014; Storz & Moriyama, 2008).

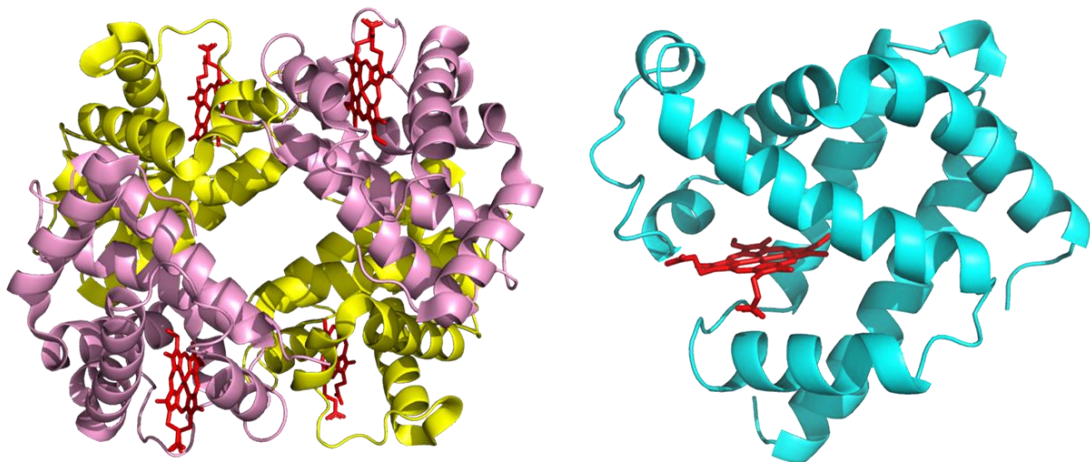


Figure 1.2 Ribbon representation of the three-dimensional structure of horse heart Hb with α subunits in yellow and β subunits in pink (left, PDB entry: 2HHB) and sperm whale myoglobin (right PDB entry: 1A6N,). The, heme group is shown in red.

Unlike hemoglobin, myoglobin is a monomeric protein with a molecular weight around 16 kDa. This protein is mainly expressed in the striated muscle (skeletal muscle and heart) but Mb was also found in neurons, endothelial, smooth muscle, and tumor cells (Burmester & Hankeln, 2014). Myoglobin exhibits one order of magnitude higher

affinity for oxygen than hemoglobin. In the venous blood, where the concentration of O₂ is low, only half of the hemoglobin will be O₂ saturated while over 90% of myoglobin will be in O₂ bound form this allows the myoglobin to extract O₂ from the blood when hemoglobin release them (Voet & Voet, 2010). Similar to Hb, Mb was also found to scavenge NO in its oxygenated form. On the other hand, deoxy Mb can produce NO by converting nitrite ion that can suppresses the reactive oxygen species (ROS) producing mitochondrial electron transport chain and subsequently protects against tissue damage caused by ischemia (Hendgen-Cotta et al., 2008). In addition, myoglobin can mediate hypoxic vasodilatation which is independent of the nitric oxide synthase pathway (Totzeck et al., 2012). Nevertheless, Mb-knockout mice did not show obvious physiological defects and exhibited normal exercise capacity due to the several physiological compensatory mechanisms, such as the increase of the hematocrit, that ensure the mouse survival (Garry et al., 1998). Importantly, Mb's mRNA and protein expression are significantly upregulated in the tumor cells (such as breast, prostate, and colon) which imply its possible role as a biomarker for cancer diagnose (Flonta et al., 2009; Gorr et al., 2010).

1.3 Novel vertebrate globins

In the last century, hemoglobin and myoglobin were considered the only globins in vertebrates. However, in the last two decades, with the help of sequencing of expressed sequence tags, six other globin types have been discovered in vertebrates: neuroglobin (Ngb), cytoglobin (Cygb), globin X (GbX), globin Y (GbY), globin E or

eye-globin (GbE) and androglobin (Adgb) (figure 1.3)(Burmester & Hankeln, 2014). While the globin fold is conserved among vertebrate globins, most newly identified globins are different in taxa and tissue distribution. Globin X is found in “lower” vertebrate such as amphibians, fish, and reptiles but missing in bird and mammals, its expression patterns varies significantly across different species (Blank & Burmester, 2012; Roesner et al., 2004). Globin Y is found in certain frogs (*Xenopus*), some lizard (*Anolis carolinensis*), some fish (*Callobinchus milii*) but is missing in the genomes of so called higher mammals such as Placentalia and Marsupialia or

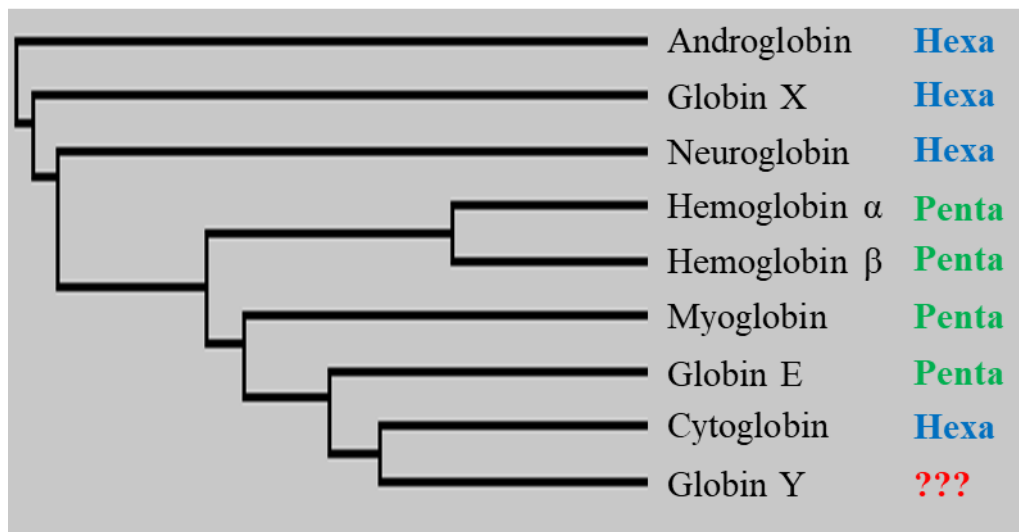


Figure 1.3. Simplified phylogenetic relationships in vertebrate globins by using uniprot database along with their coordination type (GbY is yet determined).

birds (Burmester & Hankeln, 2014). On the other hand, GbE was first found in chicken and later discovered in the coelacanth. This protein was mainly expressed in the eye, suggesting its role in O₂ supply to metabolically active retina (Blank et al., 2011). The least studied member of hexa-coordiante globoins is Adgb. This protein is widespread in Metazoan and predominantly expressed in testis suggesting its role in reproduction

(Hoogewijs et al., 2011). So far, only a limited number of studies were performed on GbX, GbY, GbE, and Adgb and their intracellular function and underlying molecular mechanism remain elusive. However, Cygb and Ngb have attracted more attention in the scientific community and their structural and physiological properties were studied intensively, as they have exhibit cellular protective and tumor suppression role in human and vertebrates (Bholah et al., 2015; Burmester & Hankeln, 2009, 2014).

1.4 Neuroglobin and Cytoglobin

Neuroglobin is the first novel globin discovered by the Burmester group in 2000 (figure 1.4)(Thorsten Burmester et al., 2000). It is a small monomeric protein with a molecular mass around 17 kDa and consist of ~150 amino acid residues. Neuroglobin is primarily expressed in neurons of the central and peripheral nervous systems and in the endocrine tissues (Laufs et al., 2004; Reuss et al., 2002). Neuroglobin can reversibly bind diatomic ligands and shown an oxygen affinity (P_{50}) of 1.9 to 2.3 torr, which is higher than that of mammalian Hb (~26 torr), but lower than that of Mb (~1 torr)(Dewilde et al., 2001).

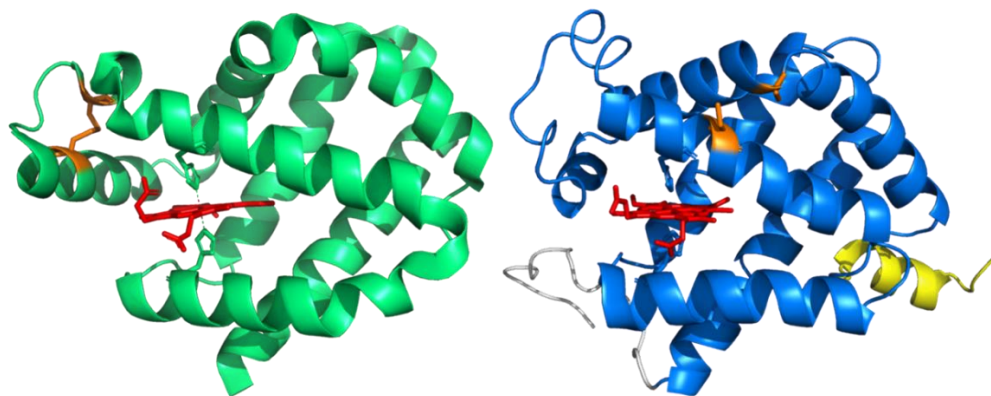


Figure 1.4. Ribbon representation of human neuroglobin (left, PDB: 4MPM chain A) and

cytoglobin (right, remodeled by PDB: 2DC3). The proximal and distal histidine is shown in sticks, the heme is shown in red, two cysteine residues are in orange. The cytoglobin extended N terminal is shown in yellow and C terminal is shown in gray.

The crystal structure of Ngb reveals several unique structural characteristics as shown in figure 1.4. It has an internal disulfide bridge formed between two of its cysteine residues (Cys 35 and Cys 65) located in a loop between C and D α -helices. In addition, the prosthetic group in Ngb is hexa-coordinated with distal histidine (His 64) binding to the heme iron in the oxidized (met form, Fe^{3+}) and reduced (deoxy, Fe^{2+}) form (Dewilde et al., 2001). Neuroglobin was initially considered to have similar function as Mb i.e. O_2 transport. However, considering a low amount of Ngb expressed in neuronal tissue, additional physiological functions were proposed for this protein. In the cultured neurons, an overexpression of Ngb reduces superoxide anion generation after hypoxia/reoxygenation and improves neuron survival (Liu et al., 2009). In addition, transgenic mice over-expressing Ngb showed reduced cerebral and myocardial infarction after middle cerebral artery (MCA) occlusion induced ischemia suggesting a neuroprotective role of Ngb (Khan et al., 2006). It has been demonstrated that Ngb reduces cytochrome c which can prevent apoptosis since the ferrous Cyt c cannot trigger apoptosis (Fago et al., 2006). On the other hand, oxidized human Ngb (Fe^{3+}) binds the α -subunits of heterotrimeric G proteins ($\text{G}\alpha$) and acts as a guanine nucleotide dissociation inhibitor (GDI) for $\text{G}\alpha$ (Wakasugi et al., 2003). This also imply an anti-apoptosis role of Ngb because the inhibition of the dissociation of GDP from $\text{G}\alpha$ and the release of $\text{G}\beta\gamma$, protects cells from apoptosis induced death. Interestingly,

Ngb is reported to interact with several other proteins such as voltage dependent anion channel (VDAC), cystatin C (a cysteine proteinase inhibitor), electron transferring flavoprotein alpha subunit (Etf α), Dvl1 (human homolog of the *Drosophila* disheveled gene), and flotillin-1 (a lipid raft microdomain-associated protein) pointing towards a potential role of Ngb in the cellular signaling pathways (Lechauve et al., 2009; Wakasugi, Nakano, & Morishima, 2004; Wakasugi, Nakano, Kitatsuji, et al., 2004; Yu et al., 2012).

Unlike Ngb, Cygb is a relatively large (20.9 kDa) protein due to the presence of the extended N and C terminals. This protein is ubiquitously expressed at variable levels with no tissue specificity in both human and mice (Figure 1.3)(Nakatani et al., 2003; Trent & Hargrove, 2002). To date, Cygb has been found in more than 20 tissues and cells such as thyroid, heart, adipose tissues, cervix, and coronary artery (Asahina et al., 2002; Thorsten Burmester et al., 2002). As a globin, Cygb is also able to reversibly bind diatomic ligands such as O₂ and compare to Ngb, it has a high affinity for this gaseous ligand (P₅₀ ~ 1 torr) which is similar to that found in Mb, suggesting a potential role as a respiratory protein (Hamdane et al., 2003). However, as in other hexa-coordinate proteins, the exogenous ligands must compete with the distal histidine that coordinates heme iron. In addition, the low level of Cygb cellular concentration (~1 μ M) and its localization make it less likely to have an analogous function as Mb (Li et al., 2012). Like Ngb, overexpression of Cygb under hypoxic conditions increase cellular survival (Zhang et al., 2017). Nevertheless, reduced or eliminated expression of Cygb can

hyperactivate a downstream effector of apoptosis, caspase-3, and promote cell death (Mathai et al., 2020). Also, several hypoxia responsive elements and hypoxia-inducible protein binding sites were found upstream of the *Cygb* gene, indicating a cellular protective role (Guo et al., 2007; Singh et al., 2009). As *Ngb*, *Cygb* was also reported to be involved in NO metabolism. A significant depression of cardiovascular functions, including a decrease in blood pressure and systemic vascular resistance, was observed in the mouse model with inactivated *Cygb* gene (X. Liu et al., 2017). This suggest that *Cygb* controls vascular reactivity through NO level regulation. *Cygb* expression is reduced in most cancer cells such as head and neck cancer, non-small cell lung cancers and a dramatic decrease (70%) was reported for oesophageal cancer (McRonald et al., 2006; Oleksiewicz et al., 2011; Shivapurkar et al., 2008). Such expression suppression can be associated with the loss of heterozygosity and hypermethylation of CpG islands in the *Cygb* gene promoter region in the cancer cells (Mathai et al., 2020). Base on this, *Cygb* could have a putative role as a biomarker for cancer diagnosis. Cytoglobin knock out transgenic mice have shown tumorigenesis and multiple organ abnormalities in one to two-year-old mice that indicate *Cygb* as a critical fundamental protein which maintain normal cellular activity of life (Thuy et al., 2016). Last but not least, *Cygb* is reported to serve as an oxygen carrier for collagen synthesis while it is up-regulated after fibrotic damaged kidney and can inhibit several fibrosis-associated components, pointing towards its anti-fibrosis function (Mathai et al., 2020).

1.5 GbX: a membrane-bound vertebrate globin

GbX is a phylogenetically ancient type of globin first discovered in fish (*Danio rerio*) and amphibians (*Xenopus*) (figure 1.5)(Roesner et al., 2004). GbX shows 18% to 26% sequence similarity with vertebrate Mbs, 22% to 26% similarity with Cygb, and 15% to 25% similarity with vertebrate Hbs. Higher sequence similarity was reported for vertebrate Ngbs, 26.0% to 34.6% (Roesner et al., 2004).

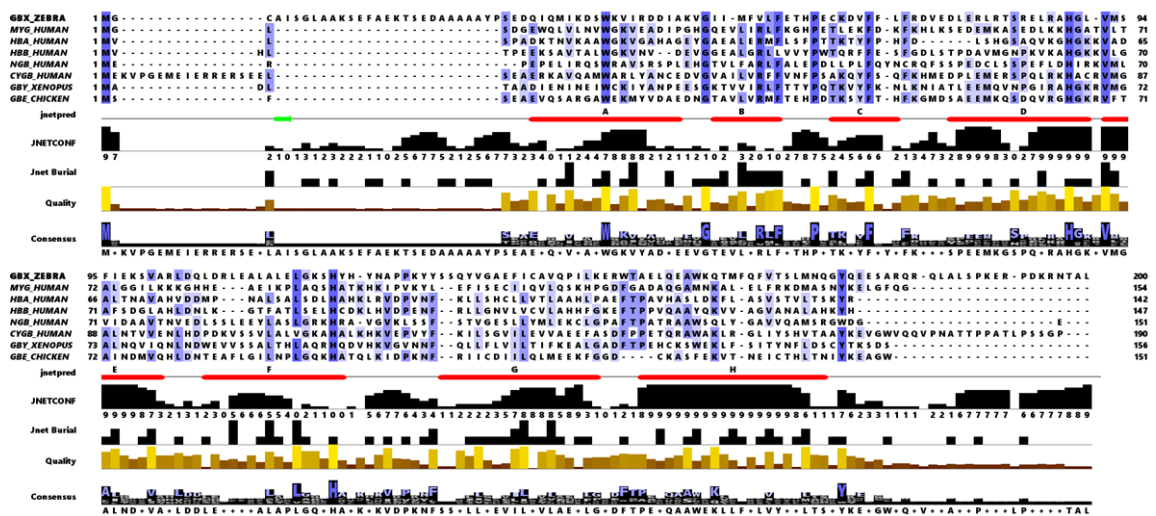


Figure 1.5. GbX sequence alignment with vertebrate globins and predicted secondary structures. Highly conserved amino acid residues are labeled with blue shadows.

The sequence of the globin core of GbX is highly conserved, with amino acid substitution rates as low as those observed in Ngb and Cygb. Therefore, the ancient divergence of GbX is probably the reason for the low similarity of GbX to other globins. Globin X has been identified in many metazoan animals while it is missing in birds and mammals (T Burmester & Hankeln, 2014). The distribution patterns of GbX across different species varies significantly, for example, it is widely expressed in goldfish tissues but more restricted in the brain and eye of *Xenopus* (Fuchs et al., 2006; Roesner et al., 2004). Burmester's group reported that GbX is the only vertebrate globin that has

the ability to bind to cell membrane. Gly2 and Cys3 were identified as the myristoylation and palmitoylation sites on the N-terminus of GbX and the post-translational acylation was proposed to be responsible for its cell membrane association capacity. Indeed, the removal of both residues, Gly2 and Cy3, abolishes the membrane association of GbX (Blank, Wollberg, et al., 2011). Subsequently, the impact of GbX on the survival of neuronal cells under hypoxic conditions or hydrogen peroxide induced stress was tested by Burmester's group in GbX and Mb transfected mouse neuron cells. Although both proteins, Mb and GbX, enhanced cell viability under hypoxia, only acylated GbX efficiently protected cells against H₂O₂-induced stress. The loss of acyl group diminished the efficiency of neuronal protection, indicating that the protective role of GbX against ROS-stress requires the protein association to the cell membrane (Koch & Burmester, 2016). Recently, Dr. Gladwin's group showed that GbX functions as a nitrite reductase with the catalytic constant of $26.7 \pm 2.0 \text{ M}^{-1} \text{ s}^{-1}$ which is 5 to 10 fold higher than the value measured for R-state Hb and Mb, 25 to 50 fold higher than the value observed in Ngb and Cygb, and even 200 fold higher than the value reported for T-state of Hb (Corti et al., 2016). The same group also reported that the recombinant GbX inhibits platelet aggregation more effectively than human Hb. In addition, cultured fish RBCs can prevent platelet activation in the presence of nitrite whereas knockdown of GbX in the RBCs will render this capability.

1.6 Heme coordination

In globins, the heme prosthetic group is located in the center of the typical 3 over 3 alpha helix structure (T Burmester & Hankeln, 2014). Although the heme propionate groups form hydrogen bonds or salt bridges with nearby amino acid residues, the most important interaction between the heme and protein matrix is the heme-histidine coordination bond (Figure 1.6). The proximal histidine located on the F helix is highly conserved among all globins and this residue binds heme iron at fifth-coordination site. When there is no other internal amino acid residue in the position of the sixth-coordination site of the heme, this type of globin is named penta-coordinate globin as seen in Hb and Mb. However, novel globins found in vertebrates (such as Cygb, Ngb, GbX, and Adgb) have additional distal histidine residue that coordinates to the heme iron in the sixth coordination site, forming the hexa-coordination (T Burmester & Hankeln, 2014).

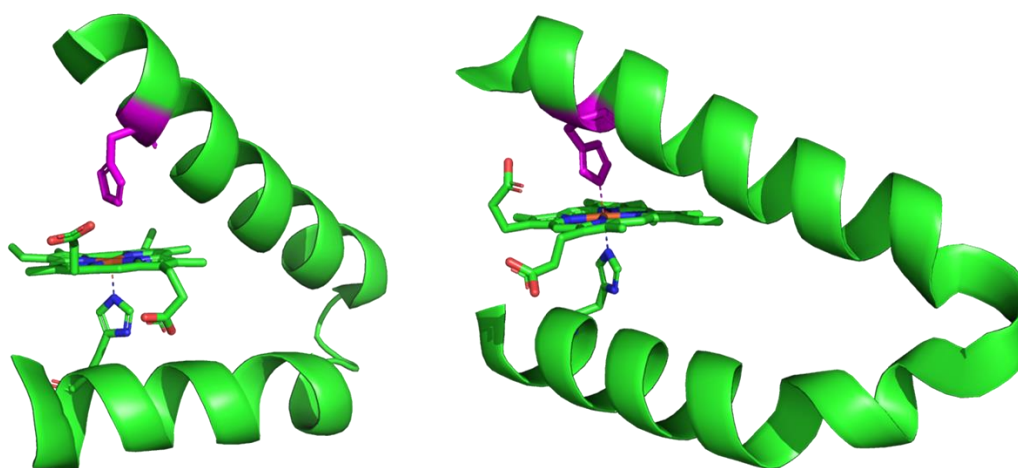


Figure 1.6. Ribbon representation of the heme binding site in vertebrate Mb (left, PDB entry 1A6N), Ngb (right, PDB entry 4MPM) demonstrating penta-coordination and hexa-coordination respectively, of the heme iron. The distal (magenta) and proximal (green) histidine residues are shown as sticks.

The hexa-coordination of the heme iron found in some vertebrate globins impacts the protein interactions with exogenous ligands, as the exogenous ligand such as O₂ has to compete with distal histidine in order to bind to the heme and the binding rate of the exogenous ligand is limited by the rate of the dissociation of the distal histidine from the heme iron. The hexa-coordination is also found in the globins of other taxa such as non-symbiotic plant, bacterial and invertebrate, however, the exact physiological function of these globins is still unclear (Kakar et al., 2010). Surprisingly, phylogenetic analysis of the globin superfamily indicates that penta-coordinate vertebrate globins (Mb, Hb, and GbE) possibly evolved from a hexa-coordinate ancestor because of the increasing demand of O₂ supply (Blank & Burmester, 2012). Interestingly, an unfolding study of Ngb and Cygb have shown an increased stability of both proteins compared to Mb implying that hexa-coordination of the heme iron might be a key feature in keeping the heme moiety bound to the globin structure at low pH (Picotti et al., 2009).

1.7 Disulfide bridge modulate protein-ligand interaction and protein stability

Other than hexa-coordination, Ngb, Cygb and GbX share another unique structural feature. Cys residues in Ngb (Cys46 and Cyg55), Cygb (Cys38 and Cys83) as well as GbX (Cys 65 and Cys 141) were reported to form internal and external disulfide bridges. Ngb and GbX are likely to adopt a monomeric form in the cell but formation of dimers with an intermolecular disulfide bridge connecting individual monomers was observed in SDS-PAGE electrophoresis and analytical ultra-centrifugation studies

(Blank, Wollberg, et al., 2011; Dewilde et al., 2001). Monomeric dimeric, and tetrameric forms were observed in studies of Cygb, but only monomeric form was detected in the SDS-PAGE electrophoresis under reducing conditions, indicating that Cygb oligomers are stabilized through intermolecular disulfide bridges (Beckerson et al., 2015; Tsujino et al., 2014). However, there is no evidence to support that Cygb is in the form of a dimer or tetramer under physiological conditions.

The role of the internal disulfide bridges in vertebrate hexa-coordinate globins remains unclear, however, considering relatively large distance between the Cys residues, the oxidation/reduction of the thiol groups trigger conformational changes in the structure of hexa-coordinate proteins which modulate the protein-ligand interactions. Namely, breakage of the disulfide bridge decreases the affinity of O₂ 2-fold in case of Cygb, two to four fold in case of GbX, and ten fold in case of Ngb (Blank, Wollberg, et al., 2011; Hamdane et al., 2003). Also, the formation of an internal disulfide bridge is critical for the interaction between Cygb and lipids as well as its lipid-peroxidase activity since Cygb binds lipids in the presence of an intramolecular disulfide bridge (Beckerson et al., 2015).

In addition, the disulfide bridge is also involved in maintaining protein stability. The hexacoordinate globins shows an increased thermal stability with Cygb having melting temperature of 95°C and Ngb of 100°C whereas horse heart Mb has melting temperature of 81°C and human Hb of 71°C (Hamdane et al., 2005). Also, engineered human Ngb with one additional disulfide bridge showed enhanced tolerance

to denaturant or acid induced protein unfolding as well as increased melting temperature (H.-X. Liu et al., 2019).

1.8 Distal histidine: gate of the distal pocket

Previous studies on pentacoordinate heme proteins have shown a crucial role of distal histidine residue in regulating affinity and kinetics of diatomic ligand binding to heme iron. A hydrogen bond between the distal histidine nitrogen and O₂ bound to the heme iron stabilizes the gaseous ligand and prevents auto-oxidation of heme iron in both myoglobin and hemoglobin (Olson et al., 1988). Substitution of Gly for the distal histidine leads to a dramatic decrease in oxygen affinity caused by a 100-fold increase in the O₂ dissociation rate constant (Olson et al., 1988). Surprisingly, the distal histidine can function quite differently between penta-coordinate and hexa-coordinate globins. Distal histidine mutations in Mb induce up to 1000-fold increase in its autoxidation rate while mutation of the distal histidine improved Fe²⁺-O₂ complex stability in Ngb around three fold (Tejero et al., 2015). Also, distal histidine replacement in Mb caused a 15-fold decrease in the nitrite reduction rate compared to the wild type whereas the mutation of the distal histidine in Ngb increased the nitrite reduction rate 2000-fold compare to wild type (Tejero et al., 2015). However, Cygb exhibits a similar redox potential (20 mV) to Mb (46 mV) and similar of equilibrium constant for O₂ and CO binding (1 μM⁻¹ and 21.7 μM⁻¹ for Cygb binding of O₂ and CO, respectively, and 1.1 μM⁻¹ and 25.5 μM⁻¹ for Mb binding of O₂ and CO, respectively) pointing towards a similar function of the distal histidine in these proteins (Sawai et al., 2003). In addition,

distal histidine in Cygb is critical for its peroxidase activity as distal histidine mutant exhibit no significant capability to oxidize guaiacol compare to wild type (Beckerson, Svistunenko, et al., 2015).

Distal histidine gating is observed in both hexa-coordinate and penta-coordinate globins as a mechanism of ligand migration regulation. The dissociation of the distal histidine is the rate limiting steps for ligand binding to heme iron in the hexa-coordinate globins because the exogenous ligand has to compete with the distal histidine for iron coordination. The sidechain of the distal histidine that can be either oriented towards the solvent (so called open conformation) or be located in the distal pocket (so called close conformation). Both positions of the distal histidine were reported for Ngb and Cygb (Exertier et al., 2019; Makino et al., 2011). Similar open and close conformation of the distal histidine were also found in Mb and Hb, and the gating effect of the distal histidine can be enhanced or weakened by replacing distal histidine with amino acid residues which has bigger bulky side chain or small shorter side chain, respectively (Birukou et al., 2010; Rohlfs et al., 1990).

Besides regulating the protein-ligand interaction, distal histidine can also play a role in modulating the stability of the globin. The hexa-coordinate Ngb and Cygb showed hyperthermal stability compared to the penta-coordinated Mb and Hb and this hyperthermal can be rendered if the distal histidine is mutated (Hamdane et al., 2005). In addition, the pH-dependent heme release experiment demonstrates the midpoint for the heme from Ngb at pH of 3.2 which is 1.4 unit lower than for Mb, $\text{pH}_{1/2}=4.6$.

However, replacement of distal histidine with glutamine in Ngb leads to an increase of $pH_{1/2}$ to 4.5 (Picotti et al., 2009).

1.9 Extended N- and C-terminals

Cytoglobin has extended N terminal by 18 amino acid residues and C terminal by 16 amino acid residues. The crystal structure revealed that the N terminal, which is highly charged with four positively and seven negatively charged residues, forms a nine amino acid residues long alpha helix whereas the C terminal, which contains five proline residues, adopts a random coil (Makino et al., 2006). While both N- and C-terminals showed no influence on Cygb lipid binding, C- terminal was proposed to affect Cygb's superoxide-scavenging activity and protein stability (Hanai et al., 2017). Since the N-terminal extension in Cygb adopts the alpha helix, a gas sensing function was proposed for this protein, based on similarity with the heme-based aero taxis transducer (HemAT) from *Bacillus subtilis* which exhibits a globin fold with the pre-A helix (Hou et al., 2000).

In addition, another vertebrate globin, (GbX) was also reported to have N- and C- terminal extensions. Two acylation sites were found on the N terminal of GbX and GbX acylation promotes its association to the cell membrane. But the C terminal extension function is unknown (Blank, Wollberg, et al., 2011). So, the physiology role of the extended N- and C-terminals needs to be determined in the novel vertebrate globins.

1.10 Heme disorder and sliding.

Two orientations of the prosthetic group in human Ngb and mouse Ngb have been reported by NMR and X-ray crystallography as well as in molecular dynamics simulation studies (Arcovito et al., 2008; Bocahut et al., 2012; Du et al., 2003; Xu et al., 2009). In Ngb, the heme group can rotate 180° around the α , γ -meso axis, with both propionate group exposed to the solvent which is different from the unique heme orientation in Mb and Cgb (figure 1.7). Such heme orientation disorder is facilitated by the enlarge heme distal cavity in Ngb and may impact the protein-ligand interaction. The putative mechanism of how the heme orientation disorder in Ngb impacts the ligand association rate was proposed by Bocahut et al. Interactions between the vinyl and methyl group on the porphyrin ring and the non-polar amino acid residues (such as, Val 109, Val 68) provide a steric hinder for the ligand migration pathway that links the distal pocket with the solvent and ultimately reduces the rate for ligand association to the heme iron (Bocahut et al., 2012). In addition, based on X-ray crystallography data, so called heme sliding phenomenon in the CO bound murine Ngb was reported (Vallone et al., 2004). While overall structure of Ngb is moderately affected by CO binding, the heme prosthetic group slides deeper into the distal cavity in the CO bound protein (figure 1.8). In addition, the large hydrophobic tunnel connecting the distal pocket and proximal cavity disappears after CO binding of Ngb. It was proposed that the heme

sliding into the deeper distal pocket can destabilize the distal histidine and thus regulate the exogenous ligand binding affinity to Ngb (Vallone et al., 2004). Several amino

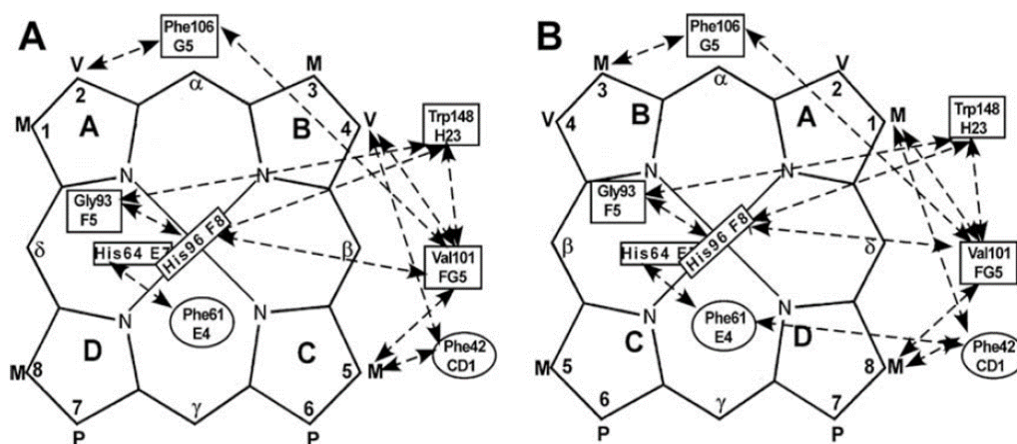


Figure 1.7. The heme orientations in Mb (A) and rotated 180° about the α - γ -meso axis (B). The heme substituents are labeled M (methyl), V (vinyl), and P (propionate) (Xu, Li, et al., 2009).

acid residues were proposed to play a role in heme sliding but only Phe-106 changes its position upon heme sliding to its crevice. NMR and molecular dynamic simulation study have shown that the Phe-106 belongs to the key residues which maintain heme stability inside the distal cavity (Bocahut et al., 2012; Xu, Yin, et al., 2009). Indeed, mutating Phe-106 will trigger the rearrangement of the heme environment and induce further displacement of the heme.

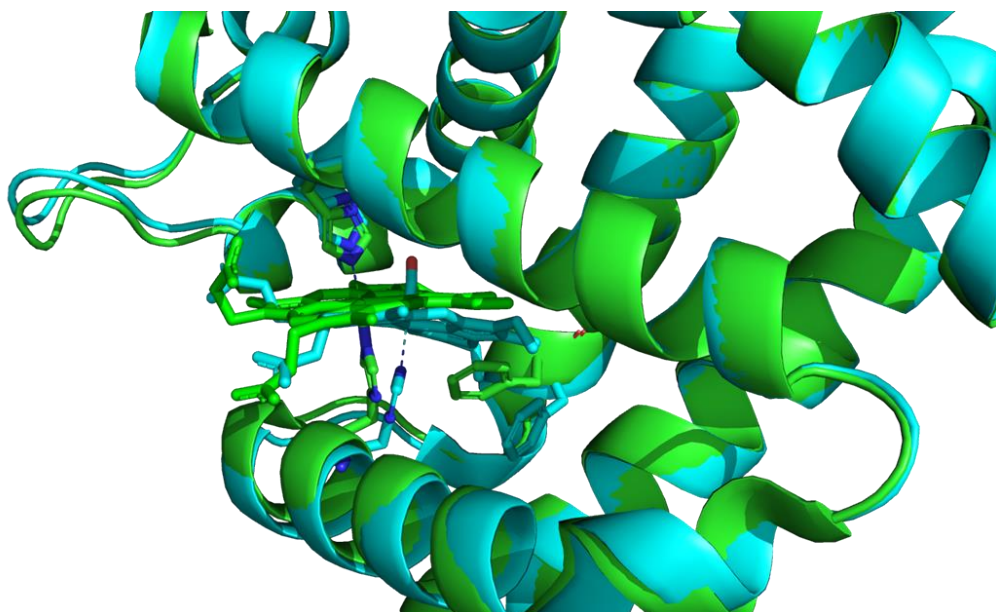


Figure 1.8. Heme sliding upon CO binding. Ferric murine Ngb (in green, PDB: 5EET), CO bound murine Ngb (in cyan, PDB: 1W92). Distal and proximal histidine, heme group as well as Phe-106 are also shown as sticks.

1.11. Globin interactions with exogenous ligands

Globins reversibly bind various exogenous ligands especially diatomic gaseous ligand such as O_2 , CO, NO in its reduced form (Fe^{2+}). Also, globins can interact with other ligands in its met form (Fe^{3+}) such as CN^- and H_2S . Characterization of interactions between globins and exogenous ligands in terms of the equilibrium affinity constant, individual rate constants and associated thermodynamic parameters, enthalpy, entropy and volume changes provide valuable information that helps to reveal potential functions of the globins, such as O_2 transportation and storage, peroxidase activity or NO reductase etc. In addition, understanding of heme proteins interactions with toxic ligands provide insight into the molecular mechanism of toxicity. For example, CO is toxic because it can tightly bind to hemoglobin thereby restrict O_2 supply in the body. Therefore, study of the interaction between globins and exogenous ligands is important

to reveal their physiological functions and understand the molecular mechanisms of their functions.

2 OBJECTIVES

Characterization of structural dynamic in protein is critical for understanding of the structural mechanism that modulate the protein interactions with ligand, binding partners and most importantly to understand their physiological functions. In addition, the studies of protein dynamics in combination with site directed mutagenesis provide an elegant approach to characterize the role of individual amino acid residues in controlling the affinity and kinetics of ligand binding to proteins. In addition, determination of thermodynamic parameters, such as activation and reaction enthalpy, entropy and volume change for ligand association and dissociation, provide insight into energetics of protein ligand interactions. In this work, structural dynamics associated with ligand binding to novel vertebrate globins, namely GbX, were investigated using steady-state and time-resolved spectroscopic methods. Beside to understanding the interactions of vertebrate globins with CO and O₂, a part of this study was devoted to characterizing how can conformation of the protein affect the ligand accessibility to the protein distal pocket by using heme florescent analogs. The universal goal of this study is to provide molecular insight into the mechanism of ligand migration and interactions with vertebrate globins.

In chapter 4, transient absorption spectroscopy as well as photoacoustic calorimetry was employed to characterize CO association and dissociation to GbX, in order to determine the reactivity and heterogeneity of heme iron in hexacoordinate globins. Also, disulfide bridge and distal histidine mutants were employed to study

how these distinct characteristics impact ligand binding, ligand affinity and structural stability of GbX.

In chapter 5, Cygb, Ngb and their mutant were reconstituted by zinc protoporphyrin IX which is a fluorescent analog of iron protoporphyrin IX (native heme). Quenching study were performed by using the reconstituted fluorescent protein. This study provides information on conformational heterogeneity in hexacoordinate globins as well as on the heme pocket accessibility.

In chapter 6, transient absorption spectroscopy as well as photoacoustic calorimetry was employed to characterize O₂ association and dissociation to GbX as well as acid titration was employed to determine how the stability of the protein is impacted by exogenous ligand binding to the heme iron.

3 MATERIAL AND METHODS

3.1 Materials

The Zinc protoporphyrin IX, Fe³⁺tetrakis(4-sulfonatophenyl)phorphine [Fe(III)4SP] was purchased from Frontier Scientific Inc. Myoglobin, dithiothreitol (DTT), Sodium dithionite, Sodium cyanide (NaCN), and 5- δ - aminolevulenic acid (5-ALA) were purchased from Sigma-Aldrich. All other reagents were purchased from Fisher Scientific. All reagents were used as received without further purification.

3.2 Methods

3.2.1 Protein expression and purification.

Cells transformed with plasmids for wild type human Ngb, human Cygb, Zebra fish GbX and mutants were kindly provided by Dr. Pierre Sebban (Paris Sud University, Orsay, France). A six-His tag was adding into the N terminal of the coding sequence of Cygb, Ngb and GbX then cloned into a pET15b expression vector. DNA sequencing was performed to confirm the correction of the insertion of the express DNA sequence in the plasmid. *Escherichia coli* strain BL21 was used for transforming the expression vectors and expression of recombinant proteins

3.2.1.1 Neuroglobin and Cytoglobin isolation and purification.

A pre-culture of 50 mL of Terrific Broth medium was cultured with the Ngb or Cygb cell for 6 h at 37°C 225 rpm with 100 mg L⁻¹ of ampicillin. Next, 15 mL of the pre-culture was transferred into 1 L of Terrific Broth medium with 100 mg L⁻¹ of ampicillin and 170 mg L⁻¹ of 5-aminolevulenic acid. Cells were incubated at 37°C and

225 rpm, until $A_{600\text{ nm}}$ reached 0.8 and the protein expression was induced by addition of IPTG to a final concentration of 0.4 mM. Cells were then incubated overnight at 30°C and 170 rpm. Cell pellet was collected by centrifugation for 15 min at 5000 rpm and 4°C (Thermo Fisher 40R) and homogenized in 50 mM Tris buffer with 1 mM DTT, 1 mM PMSF and 1mM EDTA (pH 8.0). The suspension was sonicated with a sonic dismembrator (Model 100, Fisher Scientific) and centrifuged at 5,000 rpm to remove membrane debris. The supernatant was filtered through a 0.45 μm membrane and loaded into a Ni-NTA column (Qiagen) that was previously equilibrated with 5 mM Tris buffer (pH 8.0). 50 mM Tris buffer with an increasing imidazole concentration of 5-20 mM was used to wash the column to remove non-specifically bound proteins. The column was washed until the 280 nm absorbance of eluate was less than 0.01. Ngb or Cygb was eluted with 5 mM Tris buffer (pH 8.0) containing 40 mM imidazole. Fractions with an $A_{\text{Soret}}/A_{280\text{nm}}$ ratio higher than 2.4 were collected and concentrated using Amicon Millipore concentrators. Purified protein was then dialyzed overnight against 50 mM Tris buffer (pH 7.0). SDS-Page electrophoresis and UV-vis spectroscopy were employed to assess the protein purity and protein was stored at -40 °C.

3.2.1.2 Globin X isolation and purification

A pre-culture of 50 mL of Terrific Broth medium was cultured with the cell for 6 h at 37°C 225 rpm with 100 mg L⁻¹ of ampicillin. Next, 15 mL of the pre-culture was transferred into 1 L of Terrific Broth medium with 100 mg L⁻¹ of ampicillin as well as

170 mg L⁻¹ of 5-aminolevulinic acid. Cells were incubated at 37°C and 225 rpm, until A_{600nm} reached 1.2 then induced by addition of IPTG to a final concentration of 0.4 mM and incubated overnight at 30°C and 170 rpm. Cell pellet was collected by centrifugation for 15 min at 5000 rpm and 4°C (Thermo Fisher 40R) and homogenized in 50 mM Tris buffer with 1 mM DTT, 1 mM PMSF and 1mM EDTA (pH 8.0). The suspension was sonicated with a sonic dismembrator (Model 100, Fisher Scientific) and centrifuged at 5,000 rpm to remove membrane debris. The supernatant was filtered through a 0.45 µm membrane and loaded into a Ni-NTA column (Qiagen) that was previously equilibrated with 5 mM Tris buffer (pH 8.0). Gradient imidazole buffer (50 mM Tris, 5-40 mM imidazole) was used to wash the column to remove non-specific binding protein until the absorbance at 280 nm was less than 0.01. GbX was eluted with 5 mM Tris buffer (pH 8.0) containing 100 mM imidazole. Fractions with an A_{Soret}/A_{280nm} ratio higher than 2.5 were collected and concentrated using Amicon Millipore concentrators. Purified protein was then treated with potassium ferricyanide to obtain the ferric form of GbX and further purified by G25 size-exclusion chromatography to remove potassium ferricyanide, following an overnight dialysis against 50 mM Tris buffer (pH 7.0). SDS-Page electrophoresis and UV-vis spectroscopy were employed to assess the protein purity.

3.2.2 Sodium dodecyl sulfate electrophoresis

Sodium dodecyl sulfate (SDS) electrophoresis was performed according to the procedure described by Gallagher (Gallagher, 2001). Electrophoresis gels were

purchased from NuSep (Tris-Glycine Precast Gels). The composition of 1L 10X running buffer is shown in Table 3.1. Protein samples for electrophoresis were prepared by mixing the protein solution with 20 μ L of loading buffer (Table 3.2). The protein samples were then boiled in a water bath for 8 minutes before loading to into the gel. In general, 10 to 20 μ L (~5 μ g) of protein solubilized in loading buffer were loaded into each well of the electrophoresis gel.

Ingredient	Amount
Tris-base	30.3 g
Glycine	144.4 g
SDS	10 g

Table 3.1. Ingredient of 1L 10X SDS running buffer for electrophoresis.

Initially, voltage of 100 V was applied using a power supply (Model FB300, Fisher Scientific) for 15 mins to let the sample enter the gel and then the voltage was increase to 150 V until the 20 kDa marker reaches 1 cm above the bottom of the gel.

Ingredient	Amount
Tris-HCl	0.3 M
DTT	0.6 M
SDS	10%
Glycerol	30%
Bromophenol blue	<0.06 %

Table 3.2. Ingredient of loading buffer for electrophoresis.

Upon completion of the electrophoresis, the gel was removed from the plastic frame and stained by Coomassie blue staining buffer for at least 3 hours or overnight on a low speed shaker. The gel was de-stained by de-staining buffer for 10 mins, then

Ingredient	Amount
Methanol	50%
Acetic acid	10%
DI Water	40%

Table 3.3. Ingredient of Coomassie blue staining buffer.

the colored de-staining buffer was exchange with the fresh de-staining buffer and de-staining procedure was carry out for additional 2 hours. After de-staining, the gel was

Ingredient	Amount
Coomassie blue R-250	<0.1%
Methanol	20%
Acetic acid	10%
DI Water	69%

Table 3.4. Ingredient of de-staining buffer.

placed into de-ionized water until it fully relaxed then ready for imaging. The composition of the staining and the de-staining buffer is listed in Tables 3.3 and 3.4, respectively.

3.2.3 UV-vis Spectroscopy

Primarily as a quantitative analytical technique, Ultraviolet–visible (UV–vis) spectrophotometry is focused on the absorption of near-UV (180–390 nm) or visible (390–780 nm) radiation by chemical species in the solution (Worsfold & Zagatto, 2005). The electromagnetic spectrum (Table 3.5) of these regions can provide energy

that induce the electronic transitions. Different color of visible light will be absorbed and exhibit at particular wavelengths (Table 3.6).

The Beer's law describes the relationship between absorbance and concentration, and is defined by equation 3.1:

$$A = \epsilon bc \quad (\text{Eq 3.1})$$

Where A is the absorbance of the sample (no unites), ϵ is the molar absorptivity ($l \text{ mol}^{-1} \text{ cm}^{-1}$), b is the path length of the cell with the absorbing medium (cm), and c is the concentration (mol^{-1}). Generally, organic chemicals, such as aromatic compound, absorb energy in the near-UV region as a result of $\sigma \rightarrow \sigma^*$, $n \rightarrow \sigma$, $n \rightarrow \pi^*$, and $\pi \rightarrow \pi^*$ transitions (Worsfold & Zagatto, 2005). For biochemical samples, protein is strongly absorbed in the range of 180-240 nm with is correlated to $n \rightarrow \pi^*$, $\pi \rightarrow \pi^*$ transitions of the peptide bond (Rosenheck & Doty, 1961).

Region	Wavelength range (m)	Wavelength range (commonly used units)	Type of transition
Far-Ultraviolet	10^{-8} – 1.8×10^{-7}	10–180 nm	Middle shell electron
Near-Ultraviolet	1.8×10^{-7} – 3.9×10^{-7}	180–390 nm	Outer shell electron
Visible	3.9×10^{-7} – 7.8×10^{-7}	390–780 nm	Outer shell electron
Near-infrared	7.8×10^{-7} – 2.5×10^{-6}	0.78–2.5 μm	Molecular vibration
Mid- and far-infrared	2.5×10^{-6} – 10^{-3}	2.5–1000 μm	Molecular vibration and rotation

Table 3.5. The electromagnetic spectrum (Worsfold & Zagatto, 2005).

The information of poly-L-glutamic acid absorption spectra under different conditions of ionic strength and pH can be used to estimate the secondary structure of a peptide. It is reported that random coil has an absorption maxima at 192 nm with a molar extinction coefficient around $7.1 \text{ mM}^{-1} \text{ cm}^{-1}$ while β -sheet conformations

absorb maxima at 194 nm (Rosenheck & Doty, 1961). Other than peptide bond, 3 amino acid residues with aromatic sidechains, tryptophan, tyrosine, and phenylalanine, absorb between 260-280 nm with molar extinction coefficient at 280 nm of $5.5 \text{ mM}^{-1} \text{ cm}^{-1}$ (Trp), $1.49 \text{ mM}^{-1} \text{ cm}^{-1}$ (Tyr), and $0.2 \text{ mM}^{-1} \text{ cm}^{-1}$ (Phe)(Mach et al., 1992). In addition, porphyrin exhibit several absorption bands with high extinction coefficients. The Soret or B-band is located between 380-500 nm and has a molar extinction coefficient of $10^5 \text{ M}^{-1} \text{ cm}^{-1}$. In the visible part of the spectrum, between 500-750 nm, porphyrin exhibits several absorption bands, so called Q bands, with molar extinction coefficients of $10^4 \text{ M}^{-1} \text{ cm}^{-1}$ (Uddin, 2012). Thus, the presence of the heme prosthetic group in proteins provides an extraordinary benefit to characterize the change in the heme iron spins, oxidation state or structural changes in the heme surroundings as the heme electronic spectrum is strongly impacted by these changes.

Wavelength (nm)	Color absorbed	Color observed
390-420	Violet	Green-yellow
420-440	Violet-blue	Yellow
440-470	Blue	Orange
470-500	Blue-green	Red
500-520	Green	Purple
520-550	Yellow-green	Violet
550-580	Yellow	Violet-blue
580-620	Orange	Blue
620-680	Red	Blue-green
680-780	Purple	Green

Table 3.6. The visible spectrum (Worsfold & Zagatto, 2005).

3.2.4 Circular Dichroism

Circular dichroism (CD) spectroscopy is a spectroscopic technique that allows for characterization of interactions between molecules and circularly polarized light.

Although CD spectroscopy is used widely in studies of small chiral molecules, it is an important spectroscopic technique to monitor protein secondary structure. In the CD spectroscopy, the absorbance differences between left (A_L) and right (A_R) circularly polarized light of the sample (Equation 3.2).

$$\Delta A = A_L - A_R \quad (\text{Eq. 3.2})$$

The signal is commonly recorded as ellipticity (θ) in degrees and plotted as a function of wavelength. The general relationship between ΔA and θ is described by equation 3.3 (Kelly et al., 2005).

$$\theta = 32.98\Delta A \quad (\text{Eq. 3.3})$$

The CD signal can only be detected for a chiral chromophore. The chromophore is chiral if: (i) it has a chiral chemical structure, (ii) it is covalently connected with a chiral center in a molecule, or (iii) it is located inside an asymmetric environment of a macro-molecule (Kelly et al., 2005).

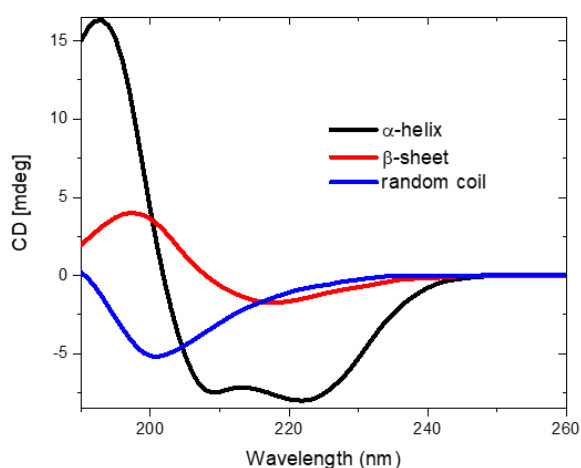


Figure 3.6. Sample electronic CD spectra of protein in α -helix, a β -sheet and a random coil. Simulated by PDBMD2CD.com with data from protein data bank.

In the protein, the optically active chromophores are the peptide bond absorbing below 240 nm, amino acid residues with aromatic side chains that absorb around 260 to 320 nm and a disulfide bridge with broad absorbance centered around 260 nm (Kelly et al., 2005). Determination of the secondary structure of polypeptides and proteins is one of CD's major application in biochemistry, as different secondary structures have distinct CD spectra as shown in Figure 3.6. For example, a typical α -helix exhibits a negative peak at ~222 nm and 208 nm together with a positive peak at 190 nm (Holde et al., 1998). On the other hand, β -sheet is characterized by a negative peak at 215 nm together with a positive peak at ~198 nm (Holde et al., 1998). Random coil shows a negative peak at around 195 nm. There is a decent number of algorithms and software packages which allow to quantify the secondary structure amount based on the far UV CD spectra (Drew et al., 2018). The prediction of the secondary structure of the protein is based on comparison of the CD spectrum of a given protein with the CD data for proteins with known secondary structure. However, the accuracy secondary structure prediction is limited, and the results should be use with cautious.

Importantly, ligand binding, sequence alteration as well as point mutations may induce secondary structure changes can be observed in the CD spectra and thus this technique can be used to characterize ligand interactions with proteins as well as impact individual amino acids on protein structure. In addition, CD spectroscopy is often used to monitor protein folding/unfolding as a function of temperature or pH and to

determine the melting temperature or pH at half-transition that are important parameters for protein stability characterization.

3.2.5 Transient absorption spectroscopy

3.2.5.1 Introduction

Time-resolved techniques allow characterization of kinetic parameters for ligand binding and dissociation from proteins that are necessary to construct kinetic models and reveal the mechanism of the protein-ligand interaction. Stopped-flow is the pioneer of the time-resolved absorption-coupled techniques and was first employed to record kinetic data for hemoglobin-oxygen complex formation (Hartridge & Roughton, 1923).

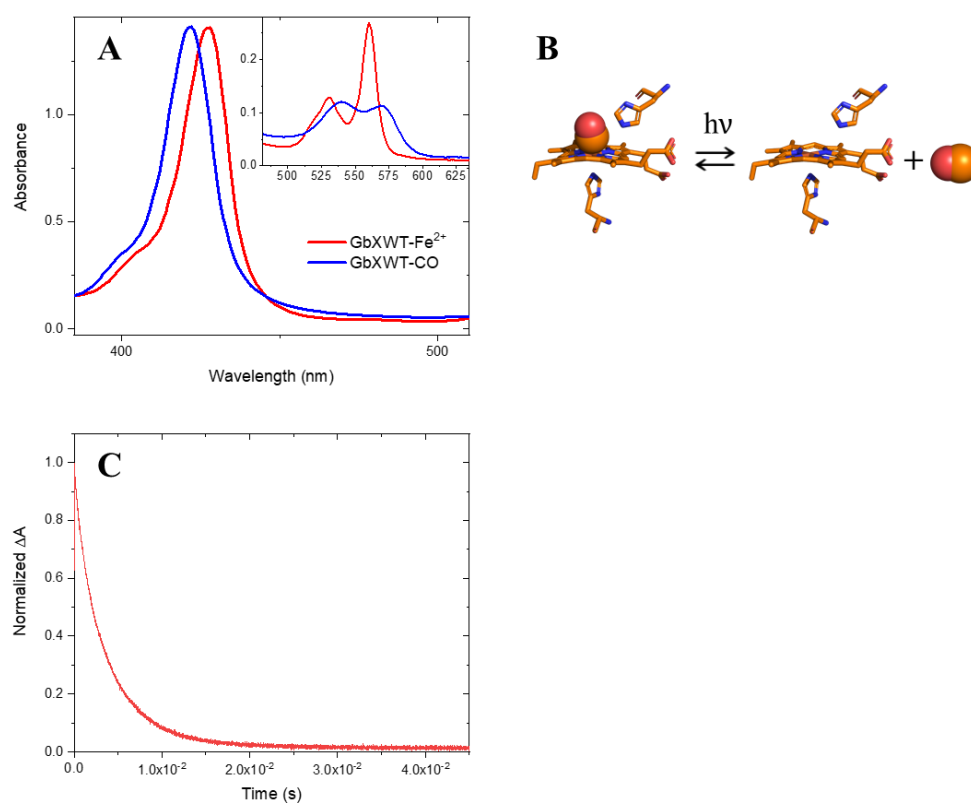


Figure 3.7. In transient absorption spectroscopy, time profiles of absorption changes that are associated with ligand binding/dissociation from proteins are measured. (A) Absorption spectrum of deoxy- and CO-GbX in the UV and visible (inset) region. (B) Simplified reaction

diagram of CO photodissociation and rebinding to swMb. (C) Time resolved absorption traces for CO recombination to GbX on microsecond to millisecond timescale.

In general, a stopped-flow instrument is used for a rapid mixing of the ligand and its receptor and the rate of the ligand-receptor complex formation is probed by monitoring the change in absorption at certain wavelength. However, the application of stop flow is limited by its time resolution of 1 ms that does not allow for monitoring reactions on sub-millisecond timescale.

Transient absorption spectroscopy (TA), also named flash photolysis or pump-probe method, is a method that uses a short pulse from a flash lamp or laser to photo-trigger a chemical reaction and monitor the absorption changes of the entire process. This concept was first reported by Gibson in 1956 in study the CO interaction with myoglobin (Gibson, 1956). Compare to the conventional stopped-flow technique, the transient absorption spectroscopy can detect events that occurs on sub-millisecond time-scales and using novel femtosecond lasers, biological event such as bond cleavage and formation as well as structural relaxation can be monitored on the time-scales from picoseconds to seconds (Weinacht & Pearson, 2018). Transient absorption spectroscopy is widely used to study photochemistry and biologically relevant photochemical process. However, the prerequisite of using TA is the present of a chromophore and photo-initiation of the reaction of interest.

Fortunately, the heme prosthetic group that absorbs across the visible spectrum and photo-liability of the iron ligand bond makes globins specifically attractive as a model system for study ligand binding reactions (Nienhaus, 2010).

3.2.5.2 TA set up

The set-up of the home-built transient absorption spectroscopy instrument in our lab is illustrated in figure 3.8. The sample was in the 0.5×1 cm quartz cuvette that was placed in a temperature-controlled cell holder (Flash 300, Quantum Northwest). The ligand photo-dissociation was triggered using a 532 nm output of Nd:YAG laser (5 ns pulse width, 1Hz repetition Minilite II laser Continuum). The laser beam was directed into the center of the cuvette by use of two laser mirrors.

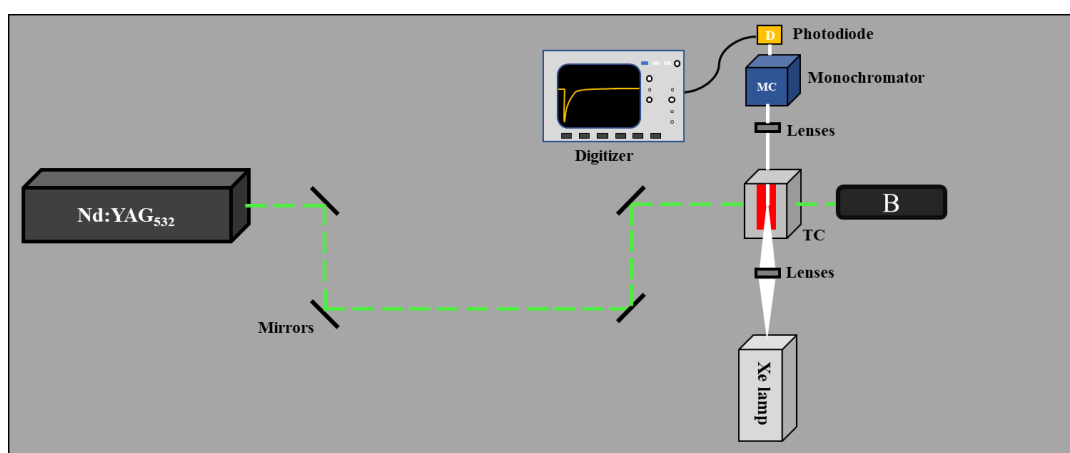


Figure 3.8. Top-view schematic of the transient absorption apparatus. TA components: the sample (red), temperature-controlled cuvette holder (TC), mirrors, pump beam (Nd:YAG532), beam blocker (B), lenses, probe beam (Xe lamp), monochromator (MC), photodiode (D) and Digitizer. Dashed line indicates pulsed light.

The 447 nm continuum wave probe beam (MDL-III-447, Changhun New Industries Optoelectronics Tech Co. Ltd) was focused on the center of the cuvette and emerging light was then focused on the entrance slit of a monochromator (Jobin Yvon) by focusing lenses. The change in absorbance was detected by a single photodiode (Model 818-BB-22, Newport) and the signal was digitized and stored in a 400 MHz digitizer (Wave Surfer 42Xs, LeCroy).

3.2.5.3 TA sample preparation

To prepare CO bound Cygb, Ngb and GbX samples, the protein stock was first diluted by 50 mM Tris-HCl buffer (pH 7.0) and gently mixed by fingertip then spin down by mini centrifuge to remove precipitate. The samples mixture was then transferred into 0.5 cm x 1.0 cm or 0.2 cm x 1.0 cm quartz cuvette by pipette and sealed with a septum cap. Argon was then employed to purge the sample for around 10 min to remove any O₂ dissolved in the solution, 1 µl of freshly prepared ~1mM sodium dithionate was injected into the cuvette by Hamilton syringe. Next, the sample was purged by CO for around 9 min and the formation of the CO bound protein was verified by the UV-vis absorption spectroscopy (single-beam UV-vis spectrometer, Cary 50, Varian). Protein concentrations were calculated using the extinction coefficient at 532 nm of 10.7 mM⁻¹ cm⁻¹ for the met form of the proteins

Ligand association kinetics.

Kinetics associated with CO rebinding to GbX were determined by fitting the absorption traces detected at 447 nm using a multi-exponential decays model (Equation 3.4).

$$\Delta A = \sum_i A_i e^{-\frac{t}{\tau_i}} \quad (\text{Eq. 3.4})$$

Where τ_i is the lifetime and A_i are the amplitude for each step, respectively.

The fitting of the experimental data was performed by multi-exponential decay model in Origin (OriginLab Corp). The quality of the fit was assessed by assessing

residuals for each fit and visual inspection. Also, the error for the rate constants were calculated based on results from three independent experiments.

The maximum entropy method (MEM) was also applied to fitting the kinetic data. The maximum entropy method is a mathematical inversion method, applied in diverse fields such as for example, neutron scattering, radio-astronomy, fluorescence as well as ligand interaction (Livesey & Brochon, 1987; Steinbach, 1996).

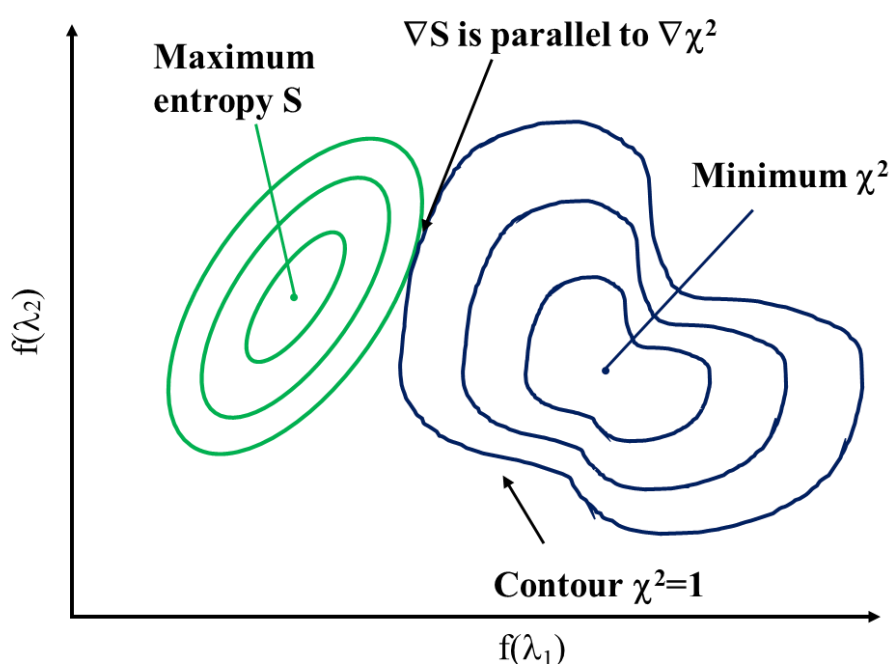


Figure 3.9. Contour plots of the statistic parameter χ^2 and the entropy S for a two dimensional $f(\lambda)$. The maximum entropy solution equivalent to the point where the gradient of χ^2 is parallel to the gradient of S , where χ^2 is close to 1. Modified from Steinbach et al. (Steinbach et al., 1992).

The general principle of maximum entropy method is that a rate of distribution $f(\lambda)$ is displayed by a discrete set of data, $f(\lambda_j)$, and Shannon-Jaynes entropy, S , is employed to measure the uncertainty arise from the defining of the function $f(\lambda_j)$. The entropy S is maximized subject to constraining the statistic parameter χ^2 to 1 (Figure 3.9). Consequently, the maximum entropy method does not bring any associations into

$f(\lambda)$ nor establishes a particular model. Therefore, the experimental data directly present the rate distribution (Peter J. Steinbach et al., 2002; P.J. Steinbach et al., 1992).

The MemExp program designed by Steinbach et al. (Peter J. Steinbach et al., 2002) was applied in this study to analyze the kinetics data collected for CO rebinding to GbX. The MemExp program combine the maximum entropy method (MEM) and either maximum likelihood (ML) or nonlinear least squares (NLS) fitting to analyze a general time-dependent data in terms of discrete and distributed lifetimes (Peter J. Steinbach, 2012; Peter J. Steinbach et al., 2002). One or two distributions of effective log-lifetimes, $g(\log \tau)$ and $h(\log \tau)$, are employed in the program to analyze kinetic data. According to equation 3.5.

$$F_i = D_0 \int_{-\infty}^{+\infty} d \log \tau [g(\log \tau) - h(\log \tau)] e^{-t_i/\tau} + \sum_{k=0}^3 (b_k - c_k) \left(\frac{t_i}{t_{max}} \right)^k \quad (\text{Eq. 3.5})$$

Where D_0 is a normalization constant, the functions $g(\log \tau)$ correspond to the distributions describing decaying kinetics and $h(\log \tau)$ correspond to the distributions describing rising kinetics. And the polynomial function represents the experimental baseline. In order to maintain the baseline comparable in magnitude, the coefficients of them are scaled by the constant parameter t_{max} . The experimental data can be used to estimate the constant D_0 , presuming that all kinetic processes involved in the temporal window of the measurements.

Pseudo-first order reactions.

Rebinding experiments were conducted in conditions of excess ligand concentrations, which generate pseudo-first order kinetics (Klostermeier & Rudolph,

2018). For ligand binding to pentacoordinate protein such as Mb, a reaction describing formation of Protein:CO complex can be written as



The rate law for P (protein) is

$$\frac{d[P]}{dt} = -k_1[P][CO] + k_{-1}[P:CO] \quad (\text{Eq 3.7})$$

The rate laws in terms of formation of P:CO as

$$\frac{d[P:CO]}{dt} = k_1[P][CO] - k_{-1}[P:CO] \quad (\text{Eq 3.8})$$

When the reaction performed under pseudo-first-order conditions, the concentration of CO will be constant over the reaction ($[CO] \approx CO_0$)

$$\frac{d[CO]}{dt} \approx 0 \quad (\text{Eq 3.9})$$

Simplify rate law for P and P:CO to

$$\frac{d[P]}{dt} = -k_1[P]CO_0 + k_{-1}[P:CO] \quad (\text{Eq 3.10})$$

and

$$\frac{d[P:CO]}{dt} = k_1[P]CO_0 - k_{-1}[P:CO] \quad (\text{Eq 3.11})$$

Based on mass conservation, we can express [P] as $P_0 - [P:CO]$:

$$\frac{d[P:CO]}{dt} = k_1(P_0 - [P:CO])CO_0 - k_{-1}[P:CO] = k_1P_0CO_0 + (-k_1CO_0 - k_{-1})[P:CO] \quad (\text{Eq 3.12})$$

and can separate the variables

$$\frac{d[P:CO]}{k_1P_0CO_0 - (-k_1CO_0 + k_{-1})[P:CO]} = dt \quad (\text{Eq 3.13})$$

The integral on the left can be evaluated by substitution of u for the denominator,

with

$$\frac{du}{d[P:CO]} = -(k_1CO_0 + k_{-1}) \text{ or } d[P:CO] = \frac{du}{-(k_1CO_0+k_{-1})} \quad (\text{Eq 3.14})$$

giving

$$\frac{1}{-(k_1CO_0+k_{-1})} \cdot \int \frac{1}{u} du = 1 \int_0^t dt \quad (\text{Eq 3.15})$$

and

$$\frac{1}{-(k_1CO_0+k_{-1})} \cdot \ln u = t \quad (\text{Eq 3.16})$$

Substituting back u and evaluating the integral from 0 to [P:CO](t) then yields

$$\frac{\ln(k_1P_0CO_0 - (-k_1CO_0 - k_{-1})[P:CO]) - \ln(k_1P_0CO_0)}{-(-k_1CO_0 - k_{-1})} = t \quad (\text{Eq 3.17})$$

which can be solved for [P:CO](t):

$$[P:CO](t) = P_0 \frac{k_1CO_0}{k_1CO_0+k_{-1}} (1 - e^{-(k_1CO_0+k_{-1})t}) \quad (\text{Eq 3.18})$$

The exponential term in eq 3.18 has the form of a simple growth reaction with e observed rate constant

$$k_{obs} = k_1CO_0 + k_{-1} \quad (\text{Eq 3.19})$$

Here, the k_1 and k_{-1} is the k_{on} and k_{off} of CO binding to protein, respectively. We can obtain the k_1 and k_{-1} by plot k_{obs} (observed rate constant for binding at different concentrations CO_0) as a function of CO_0 , since the dependence of k_{obs} and concentration CO_0 is linear, the slop is k_1 and y-axis intercept is k_{-1} .

Steady-state thermodynamics

Time-resolved experiments performed as a function of temperature can be analyzed using, Arrhenius (Eq) and Eyring (Eq) equations to obtain thermodynamic parameters for ligand binding to heme proteins. Activation energy (E_a) and pre-exponential factor (A) can be determined by using Arrhenius equation (Eq. 3.20)

$$\ln k = \ln A - \frac{E_a}{RT} \quad (\text{Eq. 3.20})$$

where A is pre-exponential factor, k is rate constant, R is gas constant, T is absolute temperature in Kelvin. On the other side, activation enthalpy ($\Delta^\ddagger H$) and entropy ($\Delta^\ddagger S$) can be determined by Eyring equation:

$$\ln \frac{k}{T} = -\frac{\Delta^\ddagger H}{R} \cdot \frac{1}{T} + \ln \frac{k_B}{h} + \frac{\Delta^\ddagger S}{R} \quad (\text{Eq. 3.21})$$

where k_B is Boltzmann constant, h is Planck's constant, k is rate constant, R is gas constant, and T is absolute temperature. It should be pay attention that E_a and $\Delta^\ddagger H$ are related quantities and $E_a = \Delta^\ddagger H + RT$ for reaction in the solution (figure 3.10)(Atkins & Paula, 2010).

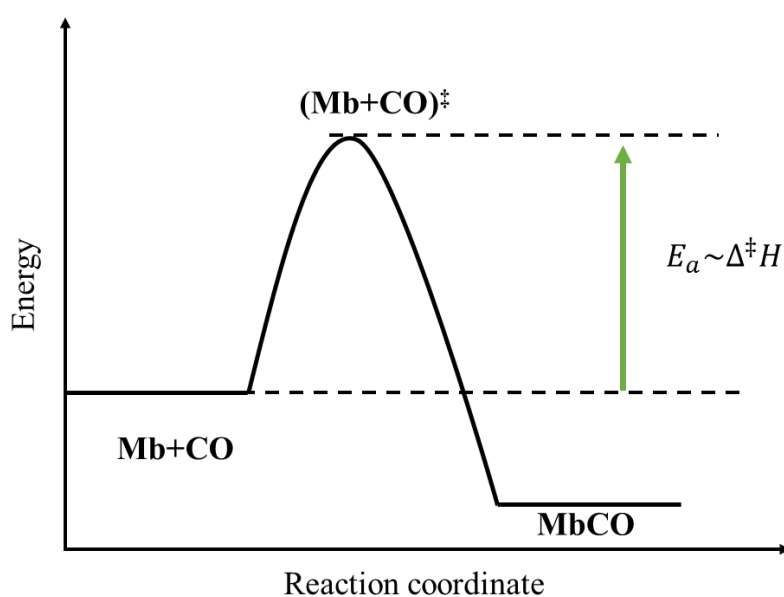


Figure 3.10. An energy diagram for CO binding to Mb.

3.2.6 Photoacoustic calorimetry (PAC)

3.2.6.1 Introduction

The changes in the electronic spectrum of chromophores can be explored by time-resolved optical methods with high sensitivity in the time range from picosecond to

millisecond and these data provide information about local structure dynamics. The ability to probe directly the thermodynamic events occurring on these time scales in the proteins, in term of molar volumes and enthalpy changes is still limited (Larsen & Mikšovská, 2007; Vetromile et al., 2011).

Photoacoustic calorimetry (PAC) which is one of the photothermal methods, is a useful techniques that capable to obtain the time scale of structural changes as well as to quantify structural changes in term of reaction volume and enthalpy changes occurring on physiologically relevant time scales in proteins (Gensch & Viappiani, 2003; Larsen & Mikšovská, 2007). Without a need for a chromophore or fluorophore, PAC is capable to observe the entire reaction enthalpy and volume change correlated with global structural changes in proteins in both magnitude and time (~ 50 ns to $10 \mu\text{s}$) (Mikšovská et al., 2008). PAC is widely used in study conformational changes associated with ligand photo-release from heme proteins, such as CO-Mb or CO-Hb.

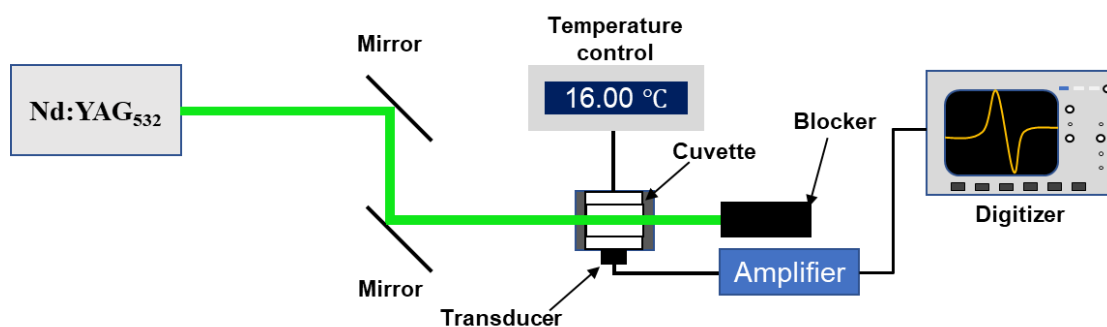


Figure 3.11. Schematic diagram of a home-build PAC instrument setup (top view).

The general physical principle behind the photoacoustic calorimetry is that upon photo-excitation of a molecule there is a accompanied dissipation of excess energy through vibrational relaxation to the ground state and concomitant thermal heating of

the surrounding solvent (Gensch & Viappiani, 2003; Larsen & Mikšová, 2007). In this thesis, PAC was employed to characterize energetic cost of structural changes upon ligand dissociation from CO-bound and O₂-bound GbX variants.

3.2.6.2 PAC set up

The home-built PAC instrument was described before (Mikšová et al., 2008). A schematic representation of the PAC instrumental setup is shown in Figure 3.11. The CO bound GbX samples were placed into a 0.5 × 1.0 cm quartz optical cuvette sealed by a septum cap. The cuvette was placed into a temperature-controlled cuvette holder (Flash 300, Quantum Northwest). The photo-dissociation of CO from GbX was triggered by a 5 ns laser pulse (532 nm, 1 Hz repetition rate, Minilite II, Continuum) and the acoustic waves were detected by a piezoelectric detector attached by a thin layer of honey to the side of the cuvette. A schematic diagram of the wave propagation in the cuvette in PAC experiment is shown in Figure 3.12.

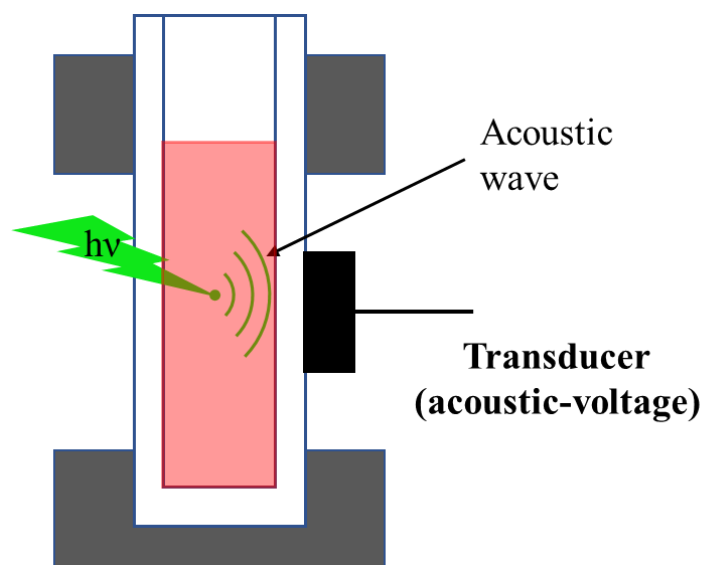


Figure 3.12. Schematic diagram of wave propagation from the sample to the detector in PAC measurements.

The signal was amplified by a pre-amplifier (C6438-01, Hamamatsu) and recorded using a 400 MHz digitizer (Wave Surfer 42Xs, LeCroy). Sample and reference (Fe(III)tetrakis(4-sulfonatophenyl)porphine, Fe(III)4SP, Frontier Scientifica Inc) traces were measured in the temperature range between 16 and 30°C under identical conditions. In order to improve the signal-to-noise ratio, 25-50 traces were averaged for each photoacoustic trace. Photoacoustic traces were then analyzed using Origin as described below.

3.2.6.3 Quantum yield determination

The quantum yield (Φ) for the biomolecular CO and O₂ dissociation was determined as described previously (Belogortseva et al., 2007). All transient absorption measurements were carried out using 20 μ M protein samples in 50 mM TrisHCl buffer, pH 7.0. Samples were transferred into a 5 mm path quartz cuvette and placed into a temperature-controlled holder (Quantum Northwest). Ligand photo-dissociation was triggered using a 532 nm output from a Nd:YAG laser (Minilite II, Continuum). The probe beam (MDL-III-447, Changhun New Industries Optoelectronics Tech Co. Ltd) was propagated through the center of the cuvette and then focused on the input of a monochromator (Yvon-Jovin) by lenses. The intensity of the probe beam was detected by an amplified photodiode (Model 818-BB-22, Newport) and subsequently digitized (Wave Surfer 42Xs, 400 MHz). The quantum yield was determined by comparing the change in the sample absorbance at 447 nm with that of the reference. CO bound Mb was used as a reference to determine quantum yields as it has a high quantum yield of

0.98 and the quantum yield is temperature independent (Schuresko & Webb, 1978).

Based on the absorption change of sample (ΔA_{sam}) and reference (ΔA_{ref}), the quantum yield was determined according to Eq 3.22:

$$\Phi = \frac{\Delta A_{sam} \Delta \epsilon_{ref} \Phi_{ref}}{\Delta A_{ref} \Delta \epsilon_{sam}} \quad (\text{Eq 3.22})$$

Where ΔA_{sam} and ΔA_{ref} are the change of the absorbance of sample and reference at 447 nm, respectively, and $\Delta \epsilon_{sam}$ and $\Delta \epsilon_{ref}$ are the difference of the extinction coefficient between the CO or O₂ bound and reduced form of the sample and the reference, respectively.

3.2.6.4 PAC data analysis

The data analysis for PAC has been previously reviewed (Gensch & Viappiani, 2003; Larsen & Mikšovská, 2007). The amplitude of the sample acoustic signals is the difference between the first maximum and minimum of the sample acoustic wave as show in figure 3.13, this is also applied for reference. The following equation describe the relation between the amplitude of the sample acoustic wave and heat released to the solvent, Q, and nonthermal volume change ($\Delta V_{nonthermal}$):

$$S = KE_a \left(Q \frac{\beta}{C_p \rho} + \Delta V_{nonthermal} \right) \quad (\text{Eq 3.23})$$

The $Q[\beta/(C_p \rho)]$ term corresponds to the thermal volume change ($\Delta V_{thermal}$). The photo-triggered volume changes such as conformation rearrangement, cleavage of the Fe-O₂ bond are described as $\Delta V_{nonthermal}$. β is the thermal expansion coefficient and it is temperature dependent for water. The term E_a is the number Einsteins absorbed and K is the instrument response parameter. A signal for calorimetric reference was measured

under conditions identical to that for sample in order to eliminate the instrument response parameter and calibrate the instrument. Fe(III)4SP was used as a reference in PAC studies as it does not undergo any photochemistry and the molecule releases absorbed energy into the surrounding solvent with a yield of unity (Abbruzzetti et al., 1999).

The amplitude of acoustic signal for reference R can be expressed as:

$$R = KE_a E_{hv} \left(\frac{\beta}{C_p \rho} \right) \quad (\text{Eq 3.24})$$

Where E_{hv} is the energy of the photon at the excitation wavelength.

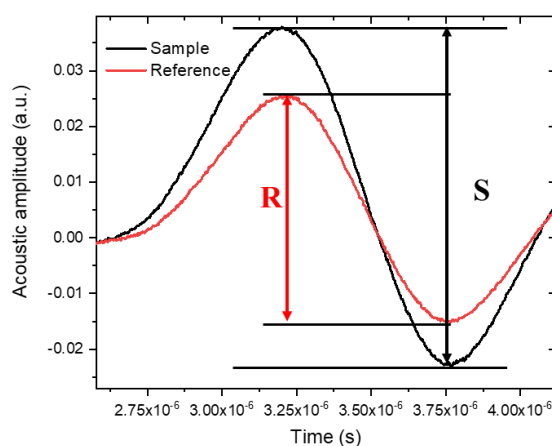


Figure 3.13. Illustrative PAC acoustic traces for sample and reference compound.

The acoustic traces were collected as a function of temperature to separate the nonthermal and thermal volume changes.

According to equation 3.25, by plot the ratio of the sample and reference acoustic waves amplitude as a function of the temperature dependent term $[\beta/(C_p \rho)]$, the non-thermal volume change can be obtained from the slope and the amount of heat released to the solution can be extract from the intercept of the linear plot.

$$\Phi E_{hv} = \left(\frac{S}{R}\right) E_{hv} = Q + \left(\frac{C_p \rho}{\beta}\right) \Delta V_{nonthermal} \quad (\text{Eq 3.25})$$

For processes with the quantum yield (Φ) less than 1, the reaction enthalpy (ΔH) and volume change (ΔV) can be determined according to equation 3.26 and 3.27, respectively.

$$\Delta H = \frac{E_{hv} - Q}{\Phi} \quad (\text{Eq 3.26})$$

$$\Delta V = \frac{\Delta V_{nonthermal}}{\Phi} \quad (\text{Eq 3.27})$$

Because the piezoelectric transducer is capable to detect not only the amplitude of the acoustic wave but also the temporal profile of the acoustic wave, reactions occurring within the time resolution (~ 50 ns to 10 μ s) of the PAC instrumentation can be characterized in term of their time constant and activation enthalpy and entropy change. The presence of a kinetic event occurring between 50 ns and 10 μ s is evident from the shift of the sample acoustic wave to lower frequencies with respect to the reference wave (figure 3.14).

The function describing the sample acoustic wave $E(t)$ is the convolution of a time-dependent heat source ($H(t)$) with the instrument response function $T(t)$ according to Eq 3.28.

$$E(t) = H(t) \otimes T(t) \quad (\text{Eq 3.28})$$

For a two-step process, the time dependence of the concentration for A and B can be expressed using equation 3.30 and 3.31.



$$[A] = A_0 e^{-\frac{t}{\tau_1}} \quad (\text{Eq 3.30})$$

$$[B] = \frac{A_0 k_1}{k_2 - k_1} \left(e^{-\frac{t}{\tau_1}} - e^{-\frac{t}{\tau_2}} \right) \quad (\text{Eq 3.31})$$

The time-dependent heat source can be expressed by equation 3.31 (Schaberle et al., 2010).

$$H(t) = \phi_1 e^{-\frac{t}{\tau_1}} + \frac{\phi_2 k_1}{k_2 - k_1} \left(e^{-\frac{t}{\tau_1}} - e^{-\frac{t}{\tau_2}} \right) \quad (\text{Eq 3.32})$$

Deconvolution the sample acoustic trace provides ϕ_1 and ϕ_2 parameters that correspond to the ratio of the amplitude for the sample and reference acoustic wave for the first and second step of the reaction, respectively, as well relaxation time τ_1 and τ_2 . The software SoundAnalysis (Quantum Northwest) was used to analyze the PAC data. The τ_1 was fixed as 1 ns, assuming the first kinetic process occurs within the laser pulse and the remaining three parameters (τ_2 , ϕ_1 and ϕ_2) were varied. The time-dependent heat source function, $H(t)$, is calculated by estimating the ϕ_1 , ϕ_2 and τ_2 parameters, and then convoluted with $T(t)$ function that corresponds to the acoustic wave for the calibration compound. The calculated acoustic wave for the sample, $E_{\text{cal}}(t)$, is then compared to the measured acoustic wave for the sample and fitting parameters ϕ_1 , ϕ_2 and τ_2 until a satisfactory fit is obtained. The quality of the fit is evaluated by visual inspection of the residuals. For processes that occur with a quantum yield, Φ , that is temperature dependent in the temperature range used in PAC measurements, the thermodynamic parameters for the fast phase ($\tau < 50$ ns) are determined by plotting $[E_{\text{hv}}(\phi-1)/\Phi]$ versus $(C_p\rho/\beta)$ according to Eq. 3.41 and the volume and enthalpy changes for the subsequent steps are obtained by plotting $(E_{\text{hv}}\phi/\Phi)$ versus $(C_p\rho/\beta)$ according to Eq 3.34. (Peters et al., 1992).

$$\frac{E_{hv}(\phi-1)}{\Phi} = -\Delta H + \left(\frac{C_p \rho}{\beta}\right) \Delta V \quad (\text{Eq 3.33})$$

$$\frac{\phi E_{hv}}{\Phi} = -\Delta H + \left(\frac{C_p \rho}{\beta}\right) \Delta \quad (\text{Eq 3.34})$$

Where ΔH and ΔV correspond to the reaction enthalpy and volume change, respectively.

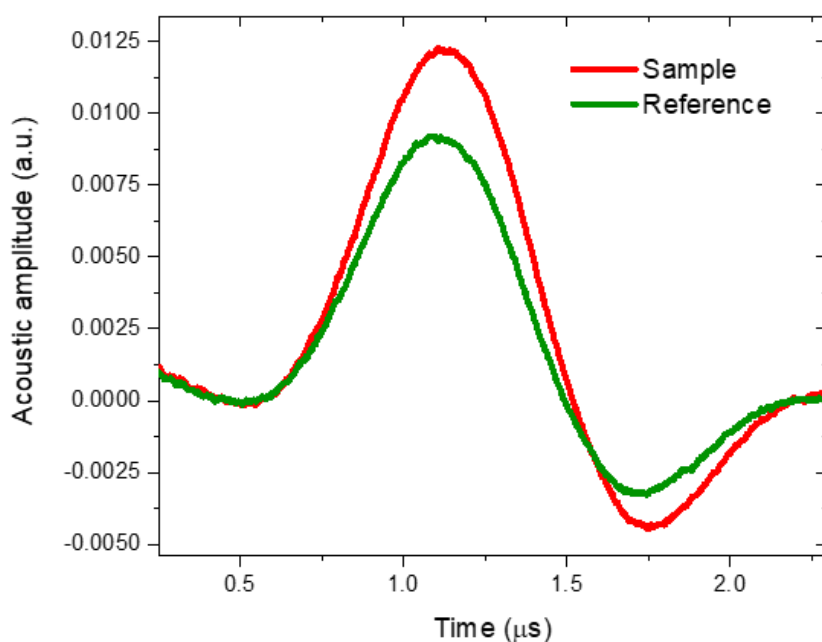


Figure 3.14. Illustrative PAC acoustic traces for the sample acoustic trace is shifted in phase compare to the reference trace.

3.2.7 Stability studies

The acid denaturation of met form or O₂ bound GbX variants was probed by observing the decrease in absorbance of the Soret band proteins upon acidification of protein samples. Aliquots (3-55 μL) of 2 M or 4 M HCl were added to 2 mL of 10 μM or 8 μM protein in 5 mM citrate/borate/phosphate buffer (pH 8.0), containing 0.1 M NaCl. After 10 min of equilibration at room temperature, UV-vis spectra and pH of the solution were recorded. The UV-vis spectra were then corrected for a dilution and the

fraction of unfolded protein was determined using absorbance values at 415 nm according to equation 3.35.

$$f_{unfold} = \frac{A_0 - A}{A_0 - A_T} \quad (\text{Eq 3.35})$$

where A_0 is the protein absorbance at neutral pH, A is the absorbance at 415 nm at any pH and A_T is the absorbance at 415 nm at lowest pH value measured. The values of the fraction of unfolded protein, $f_{unfolded}$, were plotted as a function of pH and analyzed using equation 3.36:

$$f_{unfold} = \frac{\alpha_N + m_N \times pH + (\alpha_D + m_D \times pH) \times 10^{\Delta V_{H^+} \times (pH_{mid} - pH)}}{1 + 10^{\Delta V_{H^+} \times (pH_{mid} - pH)}} \quad (\text{Eq 3.36})$$

Where pH_{mid} is the midpoints of the unfolding transitions and ΔV_{H^+} is used to describe the protons bound or released during the transition (Karp et al., 2007).

3.2.8 Cyanide affinity test

The affinity constants for cyanide binding to WT GbX and mutants were determined by monitoring the changes in the protein absorption spectrum upon addition of sodium cyanide. The titrations were performed using 8 μM protein in 50 mM Tris buffer pH 7.0 at room temperature. The titrating solution was 750 mM NaCN solubilized in the same buffer. The NaCN concentration in protein samples was varied between 0.5 mM and 150 mM. The spectrum was obtained after 2 min stirring by micro-stir bar after each NaCN addition to achieve equilibrium. The UV-vis spectra were corrected for dilution and scattering using FluorTools (a|e, FluorTools.com).

3.3 Methods: Chapter 2

3.3.1 Preparation of ZnPPIX reconstituted hexacoordinate globin

Heme was extracted based on previously published 2-butanone methods (Teale, 1959). Wild type Cygb, Ngb and mutants are denatured by addition of concentrated HCl until pH decreased to 2.0 to release the native heme group from the protein. The sample mixture was then transfer into a 25 mL volumetric flask by glass pipette and the identical volume of ice-cold 2-butanone was added (Acros Organics, 99+% spectroscopic grade). The mixture was vigorously shaken and placed on ice for ~2 min until the aqueous phase and organic phase were separated. The colorless aqueous phase containing the unfolded apo-protein was extracted and dialyzed overnight against 50 mM TrisHCl pH 2.5 to remove residual 2-butanone.

Next day, zinc protoporphyrin IX (ZnPPIX, Frontier Scientific) solution was prepared by solubilizing ZnPPIX powder in 1 M freshly prepared NaOH. ZnPPIX solution was mixed with the apo-protein sample in 1:1 molar ratio and the solution pH was then adjusted to be above 10. The ZnPPIX protein mixture was then incubated on ice for ~2 hours and GuHCl was added to achieve a final concentration of 6 M. The sample mixture was then dialyzed against 50 mM Tris-HCl, pH 7.0 to allow the ZnPPIX-reconstituted protein gradually to refold into native conformation. After dialysis, the ZnPPIX-reconstituted protein were filtered, and their absorption spectra were recorded to verify the ZnPPIX incorporation into the heme pocket and aliquot then store at 4°C.

3.3.2 Fluorescence spectroscopy

The definition of fluorescence is a molecular transition from the lowest vibrational level of the energy level S_1 to any vibrational level of the ground state, S_0 , with a concomitant photon emission (figure 3.15) (Lakowicz, 2007). Molecules that are fluorescent are called fluorophores and are distinguished by their emission spectra maxima (λ_{\max}), lifetime of the $S_1 \rightarrow S_0$ transition (τ_f) and fluorescence quantum yield (Φ_F).

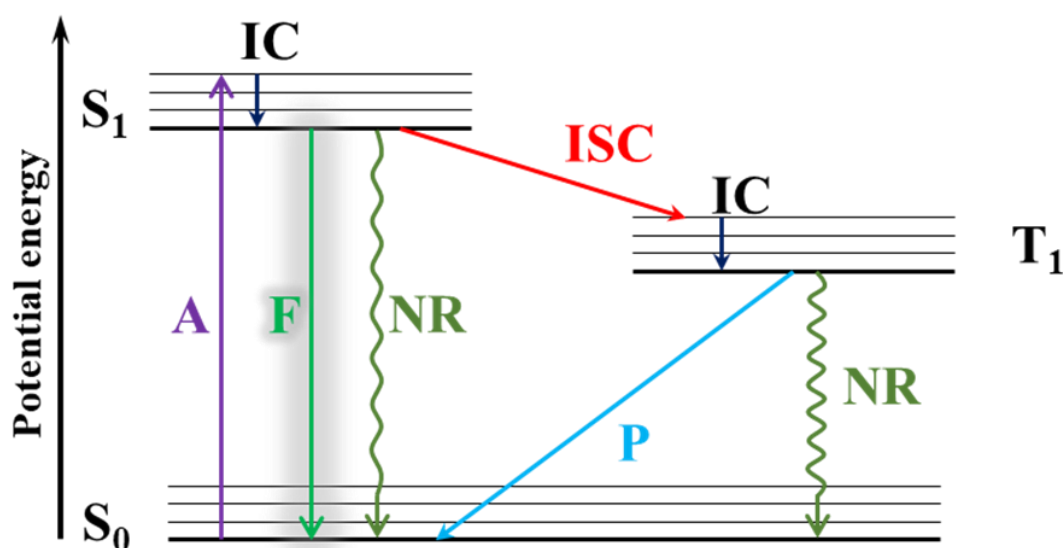


Figure 3.15. Simplified Jablonski diagram represent electronic transitions between different electronic states. A as absorption, IC as internal conversion, ISC as intersystem crossing, F as fluorescence, NR as nonradiative decay, P as phosphorescence, S as singlet state, T as triplet state.

The fluorescence studies of proteins focus on characterization of either intrinsic or extrinsic fluorescence probes. Tryptophan, tyrosine, and phenylalanine residues are usual intrinsic probes in proteins while the extrinsic probes are organic fluorophores that are non-covalently or covalently bound to the protein, for example, porphyrins,

8-anilino-1-naphthalenesulphonic acid (1,8-ANS), fluorescein (Ross & Jameson, 2008). Fluorescence spectroscopy is extensively used in studies of protein conformation and structural dynamics due to its high sensitivity to conformational changes and structural fluctuations of the fluorophore surrounding (Lakowicz, 2007). In short, the distinct properties of fluorescence such as emission spectrum, lifetime, and quantum yield, can be altered by any excited-state event including conformational changes, drug binding, presence of a quencher etc (Valeur, 2001).

3.3.2.1 Steady-state fluorescence spectroscopy

Steady-state fluorescence emission spectra were recorded using Cary Eclipse Fluorescence Spectrophotometer. The excitation wavelength used for fluorescence studies of intrinsic Trp residues in Ngb, Cygb and mutants was at 295 nm and the spectra were recorded using a 10 nm monochromator slits whereas zinc protoporphyrin IX (ZnPPIX) reconstituted proteins were excited at 421 nm and 10 nm monochromator slits were used. The protein samples were prepared by diluting the protein from stock solution in 50 mM Tris buffer, pH 7.0, to a final concentration of 4 μ M and the protein samples were then transferred into a 0.2 x 1.0 cm quartz cuvette by micropipette. Methyl viologen (MV^{2+}) quenching study were performed by titrating 4 μ M ZnPPIX reconstituted protein with increasing concentration MV^{2+} . The emission spectra from 540 nm to 740 nm were recorded as well as UV-vis spectra for inner filter correction.

3.3.2.2 Steady-state frequency-domain fluorescence lifetime

The definition of fluorescence lifetime is the time a fluorophore spends in the excited state prior to the $S_1 \rightarrow S_0$ transition (Lakowicz, 2007). Frequency-domain (FD) or phase-modulation measurements can determine the decay of the fluorophore from excited to the ground state (Holde et al., 1998). In FD measurements, the fluorophore is excited by a sinusoidally modulated light. The time-delay of the fluorescence emission is governed by the modulation frequency of excitation ($\omega = 2\pi \cdot \text{frequency}$), which result in a phase shift (ϕ_ω) to lower frequencies (figure 3.16).

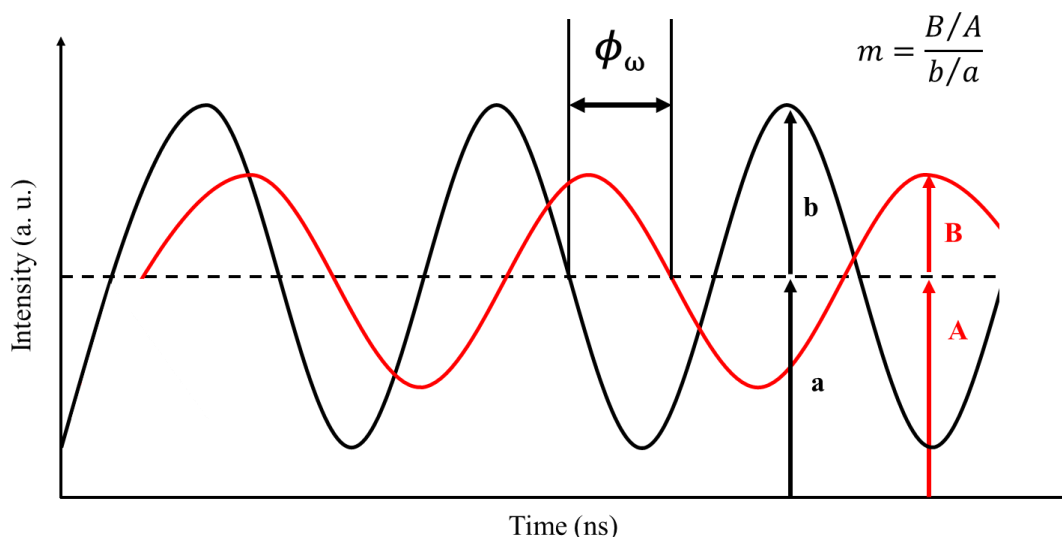


Figure 3.16. The modulation of emission (red) is decreased by modulation of excitation light intensity (black) and result in phase shift. The dash line indicated average intensity for both waves. The modulation ratio (m) is determined by the amplitude of the average intensity (a, A) and the offset from the average intensity (b, B) of emission and excitation.

For a single-exponential decay, phase lifetime (τ_{ϕ_ω}) and modulation (τ_{m_ω}) lifetime can be determined if modulation frequency (ω) is known according Eq3.37 and 3.38:

$$\tau_{\phi_\omega} = \omega^{-1} \tan \phi \quad (\text{Eq 3.37})$$

$$\tau_{m\omega} = \frac{1}{\omega} \left[\frac{1}{m^2} - 1 \right]^{1/2} \quad (\text{Eq 3.38})$$

where m is the modulation ratio and ϕ is the phase shift. The depopulation of the excited state of fluorophore is frequently a heterogeneous procedure, which need to use multi-exponential model rather than single exponential decay. Total intensity observed $I(t)$ is defined as sum of first-order processes

$$I(t) = \sum \alpha_i e^{-t/\tau_i} \quad (\text{Eq 3.39})$$

where τ_i and α_i stand for fluorescence lifetimes and pre-exponential factors associated with each fluorescence decay procedure. Particularly, if the same fluorophore is found in different environments, the pre-exponential factors (α_i) values are proportional to the fractional population of fluorophore in each environment (Lakowicz, 2007). The fraction of fluorescence intensity of each component that contributes to the multi-exponential decay is related to the pre-exponential factors according to equation 3.40(Lakowicz et al., 1984).

$$f_i = \frac{\alpha_i \tau_i}{\sum_j \alpha_j \tau_j} \quad (\text{Eq 3.40})$$

Transforms N_ω and D_ω can be obtained from multi-exponential decays of phase and modulation lifetimes, which are defined as

$$N_\omega = \frac{\sum_i \frac{\alpha_i \omega \tau_i^2}{(1+\omega^2 \tau_i^2)}}{\sum_i \alpha_i \tau_i} \quad (\text{Eq 3.41})$$

$$D_\omega = \frac{\sum_i \frac{\alpha_i \tau_i}{(1+\omega^2 \tau_i^2)}}{\sum_i \alpha_i \tau_i} \quad (\text{Eq 3.42})$$

Then, equation 3.43 and 3.44 can be used to calculate the modulation ratio and phase angle.

$$m_{\omega,calc} = (N_{\omega}^2 + D_{\omega}^2)^{1/2} \quad (\text{Eq 3.43})$$

$$\tan \phi_{\omega,calc} = \frac{N_{\omega}}{D_{\omega}} \quad (\text{Eq 3.44})$$

3.3.2.3 Time-resolved fluorescence lifetime measurement

Determination of excited-state fluorescence lifetime was performed on Chronos Spectrofluorometer (ISS) using 280 nm laser diode with 300 nm bandpass excitation filter (Andover Corp.) and a 500 nm or 550 nm long pass emission filter (Andover Corp.). ZnPPIX-proteins (in 50mM TrisHCl, pH 7.0) and reference (POPOP in ethanol, $\tau_{ref} = 1.35$) were placed in 0.5 x 1.0 cm quartz cuvette. The phase shift and modulation ratios were recorded on 15 modulation frequencies between 20-200 MHz and analyzed using Vinci Software (ISS).

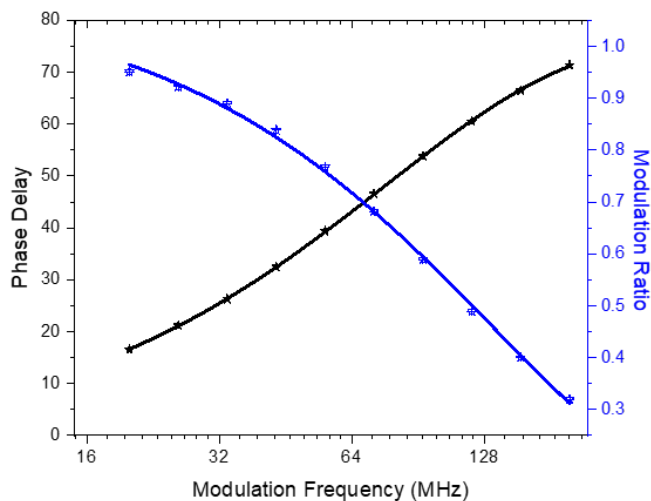


Figure 3.17. Phase delay (ϕ_{ω}) and modulation ratio (m) versus modulation frequency (ω) for POPOP reference compound.

3.3.3 Phosphorescence

Fluorophore molecules in the lowest vibrational level of the excited state S_1 can undergo an intersystem crossing to the excited triplet state (T_1). This nonradiative

transition is caused by spin conversion which leads to the electron of excited state (T_1) and ground (S_0) with the same spin ($\uparrow\uparrow$) (Lakowicz, 2007). The conversion from the triplet state to the ground state occurs on millisecond to second timescale and due to fact that the $T_1 \rightarrow S_0$ transition is spin-forbidden and requires change in multiplicity (Lakowicz, 2007). Since T_1 has lower energy than S_1 , phosphorescence spectra are red shifted compared to fluorescence (Lakowicz, 2007). In addition, because the quantum yield for phosphorescence are usually low ($\Phi_P \sim 10^{-6}$), determination of the phosphorescence properties requires very concentrated samples and the measurements are carry out at low temperatures (Lakowicz, 2007). Also, as O_2 is a very efficient quencher for phosphoresce, sample need to be thoroughly deoxygenated.

3.3.3.1 Phosphorescence measurement

Transient absorption spectroscopy was used to monitor phosphorescence decay of ZnPPIX-incorporated globins. ZnPPIX-reconstituted samples (20 μ M) were prepared in a 0.5 x 1.0 cm quartz cuvette, sealed with a septum cap and parafilm. The sample was wrapped by foil to avoid light exposure and deoxygenated with argon for one hour while gently stirring using a micro stir bar. The cuvette containing sample was then placed into a cell holder and excited with a Nd:YAG laser (Minilite, Continuum) with a 532 nm output (pump beam). The absorbance of the triplet state was monitored using a 447 nm diode-pumped solid-state laser (MDL-III-447, Changchun New Industries Optoelectronics Tech Co. Ltd.).

4 IMPACT OF THE DISULFID BRIDGE AND DISTAL HISTIDINE ON LIGAND MIGRATION IN GLOBIN X.

4.1 Introduction

Globin is a sub-super family of heme proteins that carry out a variety of functions in different organisms such as oxygen storage and transport, catalysis, cellular signaling, and electron transfer (T Burmester & Hankeln, 2014; Larsen & Mikšovská, 2007). Hemoglobin (Hb) and myoglobin (Mb) are the two most well-studied globins, which were considered the only two globins in vertebrates. However, in the past two decades, sequences of new members of globin family were discovered in the Expressed Sequence Tags (EST) database including sequence for neuroglobin (Ngb), cytoglobin (Cygb), globin E and globin X (T Burmester & Hankeln, 2014). Globin X (GbX) consists of ~200 amino acids and thus is larger than a typical globin (~150 amino acids), and it is mainly found in fish and amphibians but seemingly lost in birds and mammals (Dröge & Makalowski, 2011). Like Cygb, GbX has extended N-terminal and C-terminal, and it has been shown that myristylation and palmitoylation of residues located on the N-terminal extension of GbX, which may be responsible for its membrane binding capacity (Blank, Wollberg, et al., 2011). The expression patterns of globin X in different species are distinct, as it is broadly expressed in various non-neuronal tissues in goldfish and whereas in *Xenopus* this protein is expressed mainly in the brain and eye (Fuchs et al., 2006; Roesner et al., 2004). However, the primary function of globin X remains elusive.

Unlike hemoglobin or myoglobin which are penta-coordinate, GbX belongs to hexa-coordinate globins, which means that the distal histidine also coordinates to heme iron in the met and deoxy form of the protein. Previous study has shown that the distal histidine in both Ngb and Cygb is involved in regulating the affinity for gaseous ligands (Astudillo et al., 2012; Hamdane et al., 2003). Distal histidine can swing in or out of the heme binding pocket, populating either close or open conformation of the distal pocket. Such distal histidine conformational flexibility was associated with increased the heterogeneity of the distal pocket in Ngb and Cygb. Interestingly, hexa-coordinate globins shown a higher thermal stability compared to penta-coordinate globins (Hamdane et al., 2005).

Similar to both Cygb and Ngb, GbX is also reported to be able to form disulfide bridge between two of its cysteine residues (65 and 141)(Blank, Wollberg, et al., 2011). Study has shown the disulfide bridge modulates the affinity of Ngb and Cygb to oxygen as well as the carbon monoxide binding kinetics through a conformational change in the E helix where the distal histidine located (Astudillo et al., 2013; Hamdane et al., 2003). Reeder's group has shown that the intramolecular disulfide bridge in Cygb is crucial for lipid binding, and Morishima's group has shown that the internal disulfide bridge in Ngb is vital for protein-protein interactions between Ngb and Gα11 (Beckerson, Wilson, et al., 2015; Wakasugi et al., 2003). Since the disulfide bridge can be cleaved and reformed through cellular activities, this implies that the

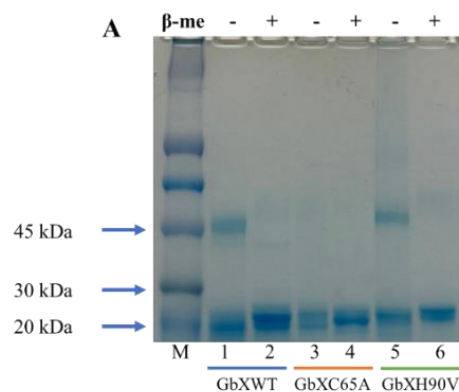
reduction/oxidation of disulfide bridge in both proteins may have significant impact on protein function.

So far, only a limited number of studies were performed on GbX and the crystal structure of GbX is also unknown. Burmester's group has shown that both Mb and GbX transfected cell has higher viability under hypoxia while GbX promotes cell survival under conditions of oxidative stress (Koch & Burmester, 2016). Gladwin's group has shown that GbX is expressed in zebrafish red blood cells, and it has a potential role as nitrite reductase in the blood (Corti et al., 2016). Unfortunately, the molecular mechanism of how GbX can carry its potential physiological functions is not clear. Since the majority of GbX's putative functions involve interactions with small diatomic ligands, in this study, we characterize CO binding to GbX as a probe to monitor how distinct structural properties of GbX, internal disulfide bridge, and distal histidine, affect GbX affinity and kinetics for diatomic ligands.

4.2 Result

4.2.1 Oligomerization state of purified GbX

Purification of recombinant GbX variants was confirmed by SDS-PAGE show in



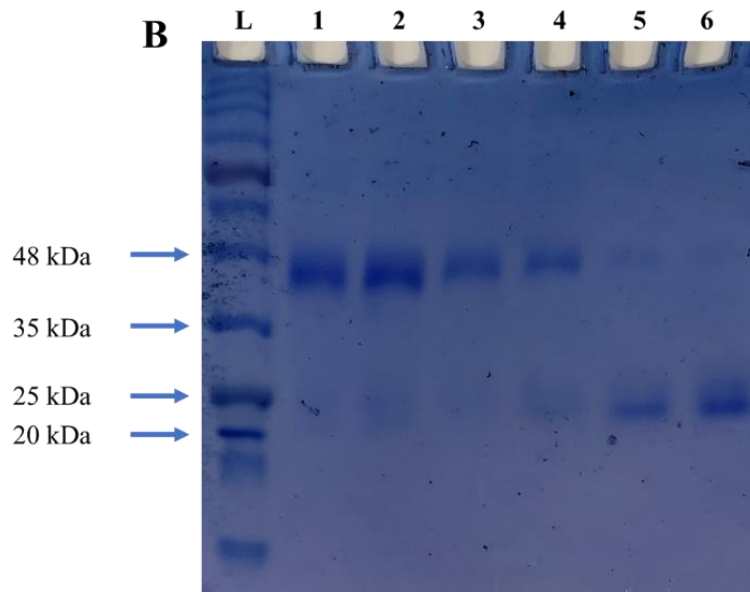


Figure 4.1. SDS-PAGE gel for purified GbX variants in the presence/absence of β -me. B, SDS-PAGE gel for GbXWT fractions after separation of monomer and dimer using size exclusion chromatography.

figure 4.1 A. A band with molecular mass around 25 kDa was observed in samples for all constructs and corresponds to the theoretical molecular mass of the GbX variants. For GbXWT and GbXH90V samples prepared in the absence of β -me, an additional band of lower intensity with a molecular mass of approximately 50 kDa was detected in samples without β -me. The absence of 50 kDa band in the GbXC65A mutant suggests that this band represents a covalent homodimer, with Cys65 participating in the disulfide bridge. Although the expression level of the dimer is less than the expression level of monomer, around 30%, the protein samples were further purified using a size exclusion chromatography to separate oligomeric species (figure 4.1B). The results presented in this manuscript were obtained for GbX monomer, unless otherwise specified.

4.2.2 Steady-state UV-vis spectra and far-UV CD spectra

The UV-vis spectra of GbX variants are similar to the spectra of other hexa-

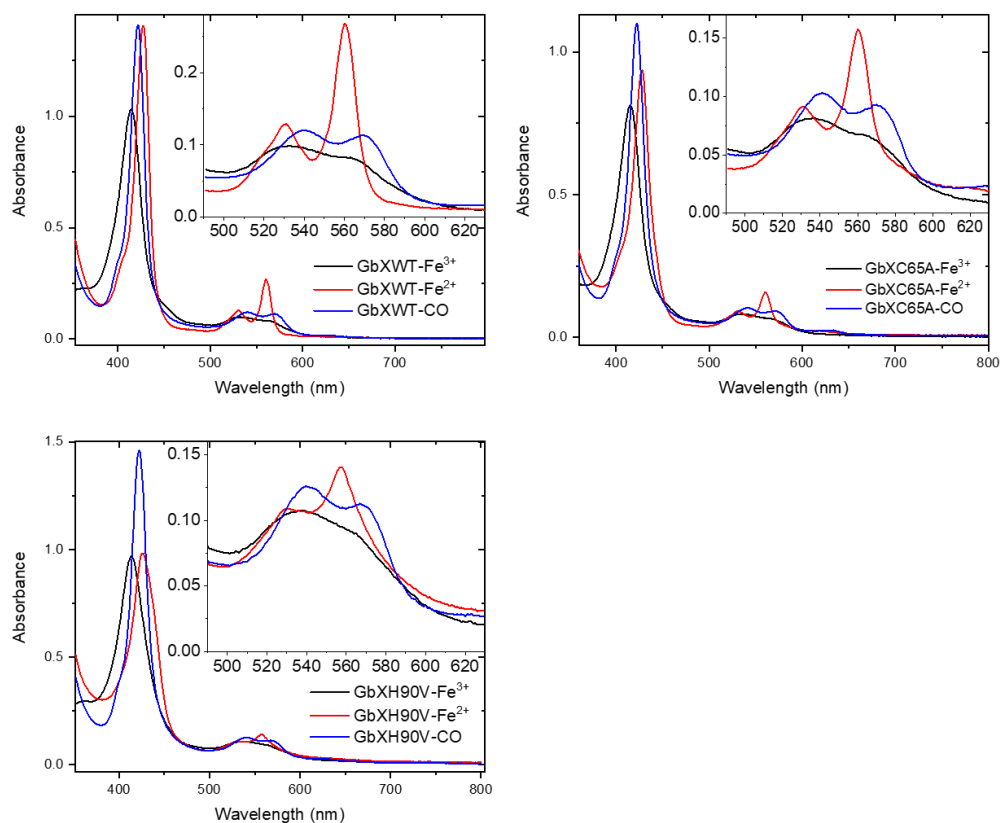


Figure 4.2. Absorbance spectra of the oxidized (met), reduced (ferrous deoxy), and CO bound forms of GbX variants.

coordinated globins such as Cygb and Ngb. The met-form of GbXWT shows a Soret peak at 414 nm and two additional Q-bands at 532 nm and 563 nm (Figure 4.2; Table 4.1). The deoxy-form of GbXWT exhibits a Soret peak at 428 nm and Q-bands at 531 nm and 560 nm that are characteristic for heme proteins with an intrinsic bis histidine coordination of the heme iron (Wang et al., 2003). Upon CO addition, the Soret band shifts to 422 nm and Q-bands appears at 539 nm and 569 nm, in agreement with the formation of low-spin hexa-coordinated CO bound heme iron. Absorption spectrum of

met form of GbXC65A has the Soret band at 415 nm but the β band position is 4 nm red-shifted compared to the spectrum of met form of GbXWT, suggesting that

	Soret band (nm)	β -band (nm)	α -band (nm)
GbXWT-Fe³⁺	414	532	563
GbXWT-Fe²⁺	428	531	560
GbXWT-CO	422	539	569
GbXC65A-Fe³⁺	415	536	564
GbXC65A-Fe²⁺	428	531	560
GbXC65A-CO	422	541	570
GbXH90V-Fe³⁺	414	536	565
GbXH90V-Fe²⁺	426	530	557
GbXH90V-CO	422	540	567

Table 4.1 UV-vis absorption spectra wavelength of Soret and α/β band of each GbX variants. the heme electronic structure is altered by the removal of the intra-protein disulfide bond. The absorption spectra of the deoxy- and CO bound GbXC65A constructs are nearly identical to those observed for GbXWT.

The absorption spectra measured for GbXH90A mutant do not clearly show a presence of a five-coordinate heme iron in the met- or deoxy form of the protein, although a shoulder of the Soret band and low absorbance of the α and β bands observed in the deoxyGbX spectrum are consistent with a fraction of the protein being in the five-coordinate form. A similar absorption spectrum was reported previously for NgbH64Ala mutant and attributed to the presence of a water molecule (Tejero et al., 2015).

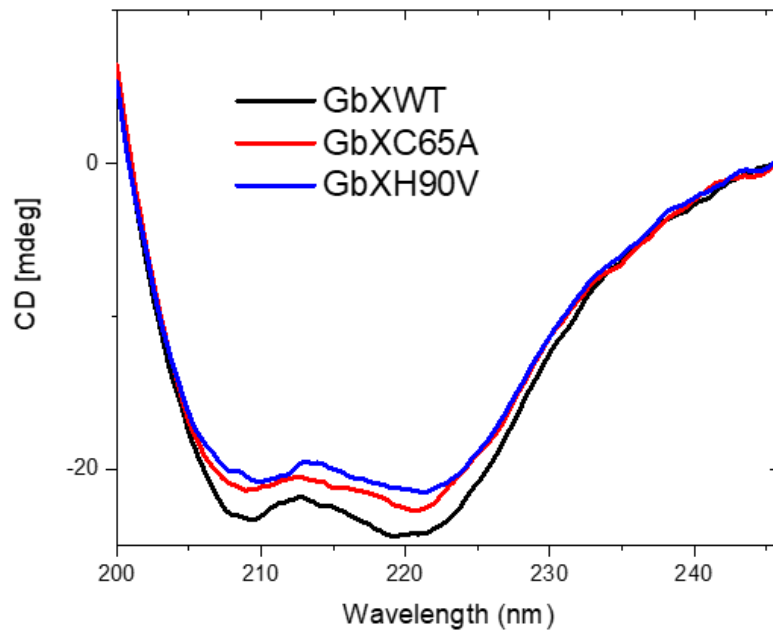


Figure 4.3. CD spectra in the far-UV region of GbX variants. All samples are aligned at Abs₂₈₀ nm.

Far-UV CD spectra of all GbX variants show two prominent minima at 208 nm and 222 nm which are similar to the CD spectra recorded previously to hexa-coordinated globins and characteristic for α -helical proteins (figure 4.3).

4.2.3 Stability of GbX towards pH unfolding

The stability of GbX constructs was probed by monitoring absorbance of the Soret band as a function of pH. The overlay of the absorption spectra of met GbXWT measured in the pH range from 8.0 to 1.6 are shown in Figure 4.4.

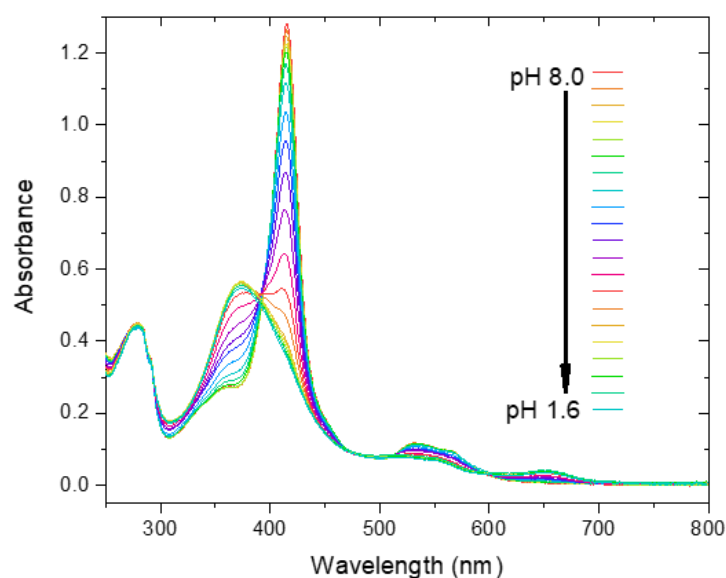


Figure 4.4. Acid-induced unfolding of GbXWT UV-vis absorption spectra. Measurements were performed in 5 mM phosphate-citrate buffer and 100 mM NaCl, under equilibrium conditions.

Figure 4.4 shows an isobestic point at 393 nm, pointing towards a two-state release of the heme group. The absorption spectrum of GbXWT measured at pH 1.6 shows a broad Soret band with a maximum at 372 nm which is consistent with a destabilize polypeptide chain and a concomitant release of the prosthetic group from the protein matrix. Analogous changes in the absorption spectra were determined for pH unfolding of GbXC65A and GbXH90A constructs (data not shown). The fraction of unfolded protein calculated based on the absorbance changes at 415 nm was plotted as a function of pH for all construct studied (Figure 4.5; Table 4.2) and the experimental data were analyzed using Eq.3.36.

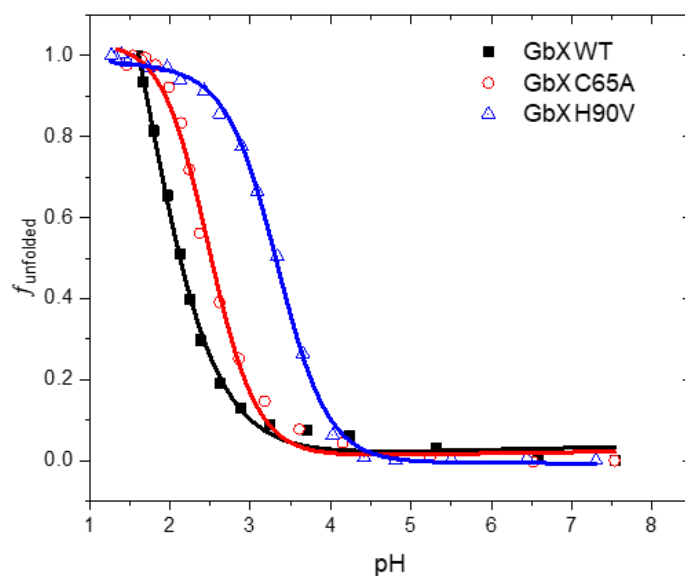


Figure 4.5. Acid-induced GbX variants unfolding. The solid line corresponds to the experimental data using Eq. 3.36. Measurements were performed in 5 mM phosphate-citrate buffer and 100 mM NaCl, under equilibrium conditions.

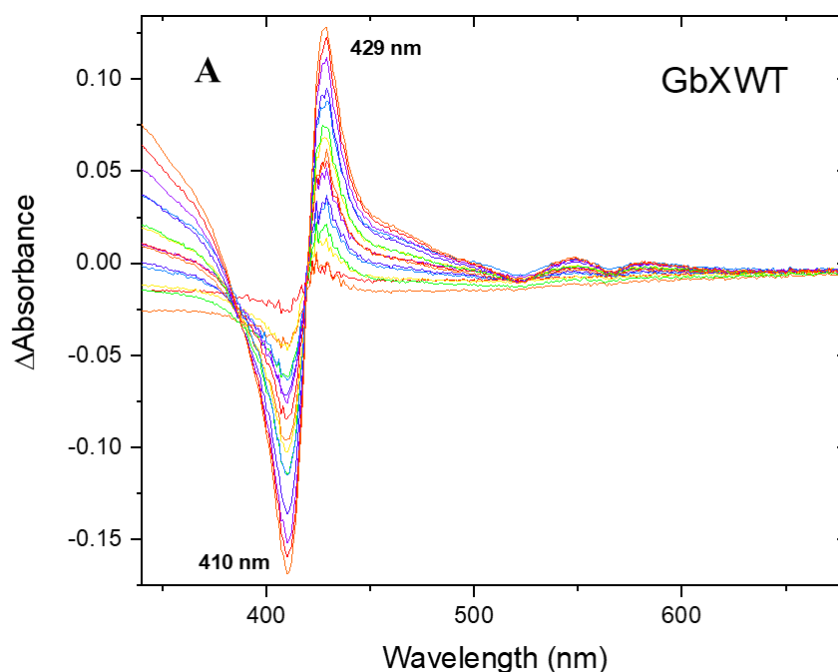
The pH induced unfolding of GbXWT is characterized by a pH at half-transition (pH_{mid}) of 1.9, which is about 2.7 units lower than that previously reported for horse heart Mb (pH_{mid} 4.6) and 1.3 units lower than that determined for Ngb (pH_{mid} 3.2), indicating that the unfolding of the protein structure and release of heme in GbX occurs at more acidic pH range. The absence of the internal disulfide bond or the coordination bond between the distal histidine and heme iron decreases the protein stability, as the release of the heme group from GbXC65A and GbXH90A is characterized by pH_{mid} of 2.48 ± 0.01 and 3.4 ± 0.1 , respectively. The n values were found to be close to unity suggesting that the destabilization of the protein is associated with a protonation of a single amino acid residue.

	pH_{mid}	Δv_{H^+}
GbXWT	1.9 ± 0.1	-1.3 ± 0.1
GbXC65A	2.48 ± 0.01	-1.4 ± 0.1
GbXH90V	3.4 ± 0.1	-1.2 ± 0.2
*hCygb	3.3	N/A
*hNgb	3.3	N/A
*hMb	4.6	N/A

Table 4.2. Parameters of the pH-induced GbX variants unfolding (* (Picotti et al., 2009)).

4.2.4 CN⁻ binding to GbX

Cyanide is frequently used as a probe to characterize the distal pocket in met form of heme proteins as it binds to the heme axial site in the met form of the heme proteins. Cyanide binding to ferric GbX leads to a red shift in the Soret band to 419 in case of GbXWT, and to 420 nm for the GbXC65A mutant as shown in Fig.6A. The equilibrium dissociation constants for CN⁻ binding to met form of GbX constructs are determined by monitoring the changes in the absorption spectra upon addition of small aliquots of CN⁻ stock solution.



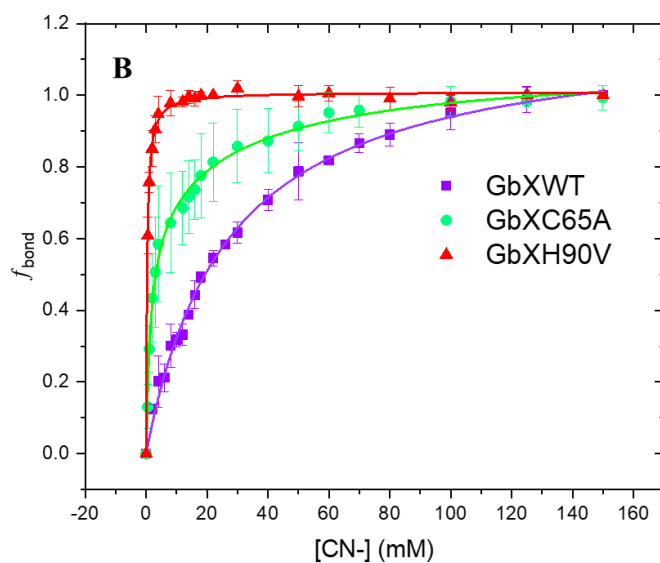


Figure 4.6. A, absorption difference spectra at various cyanide concentrations, relative to the ferric GbX form (without cyanide), the spectra were measured at room temperature in 50 mM TrisHCl at pH 7. B, cyanide binding to GbX variants, fraction bond was calculated by absorption at 410 nm as a function of cyanide concentration, only cysteine mutant shows possible two binding sites.

The fraction of protein in the CN^- bound form was calculated based on the absorbance at 410 nm at various CN^- concentrations (Figure 4.6 A) and the plots of the fraction of proteins in the CN^- bound form as a function of cyanide concentrations are shown in figure 4.6 B. The titration curves for GbXWT and GbXH90V were analyzed using a single binding model whereas of the titration curve for GbXC65A construct was fitted using a two independent binding site model, as the single binding site model have not provided a satisfactory fit. The CN^- binds to GbXWT and GbXH90V mutant with an equilibrium dissociation constant, $K_d = 27 \pm 1$ mM and 0.3 ± 0.1 mM respectively. Interestingly, GbXWT has 10,000-fold lower affinity for CN^- than previously reported affinity of CN^- association to Cygb. Unlike GbXWT and GbXH90V mutant, titration of GbXC65A mutant shown two cyanide binding sites, a high affinity site ($K_d = 1.5 \pm 0.4$ mM) and a low affinity site ($K_d = 38 \pm 4$ mM).

	K_d1 (mM)	K_d2 (mM)
GbXWT	27±1	N/A
GbXC65A	1.5±0.4	38±4
GbXH90V	0.3±0.1	N/A
†hCygbWT	0.0028	0.32
‡hMbWT	1.7	N/A

Table 4.3. Parameters of the CN⁻ binding to GbX variants (†(Tsujino et al., 2014), ‡(Dou et al., 1996)).

4.2.5 GbX CO binding kinetic

To further analyze interactions of GbX variants with diatomic ligand, CO binding kinetics were determined using transient absorption spectroscopy. The transient absorption traces for CO binding to GbX constructs studied are shown in Figure 4.7 A. The traces were analyzed using both multiple-exponential decay model and MEM (maximum entropy method) and the kinetic parameters are summarized in Table 4.4. Four distinct kinetics were resolved for CO association to GbXWT: $k_1 = 4 \pm 0.3 \mu\text{M}^{-1} \text{s}^{-1}$, $k_2 = 0.87 \pm 0.09 \mu\text{M}^{-1} \text{s}^{-1}$, $k_3 = 0.49 \pm 0.06 \mu\text{M}^{-1} \text{s}^{-1}$ and $k_4 = 0.08 \pm 0.02 \mu\text{M}^{-1} \text{s}^{-1}$, although the amplitude associated with the slowest rate constant is small, ~ 5%. Similar rate constants were obtained using MEM analysis. The analysis of the CO rebinding kinetics to GbXC65A mutant reveals three kinetics with the rate constants similar to k_2 , k_3 and k_4 found for CO rebinding to GbXWT. The slowest process characterized by k_3 has a small amplitude, ~ 4%. The substitution of distal His 90 by Ala results in significantly faster CO rebinding with the first two rate constants being faster than those

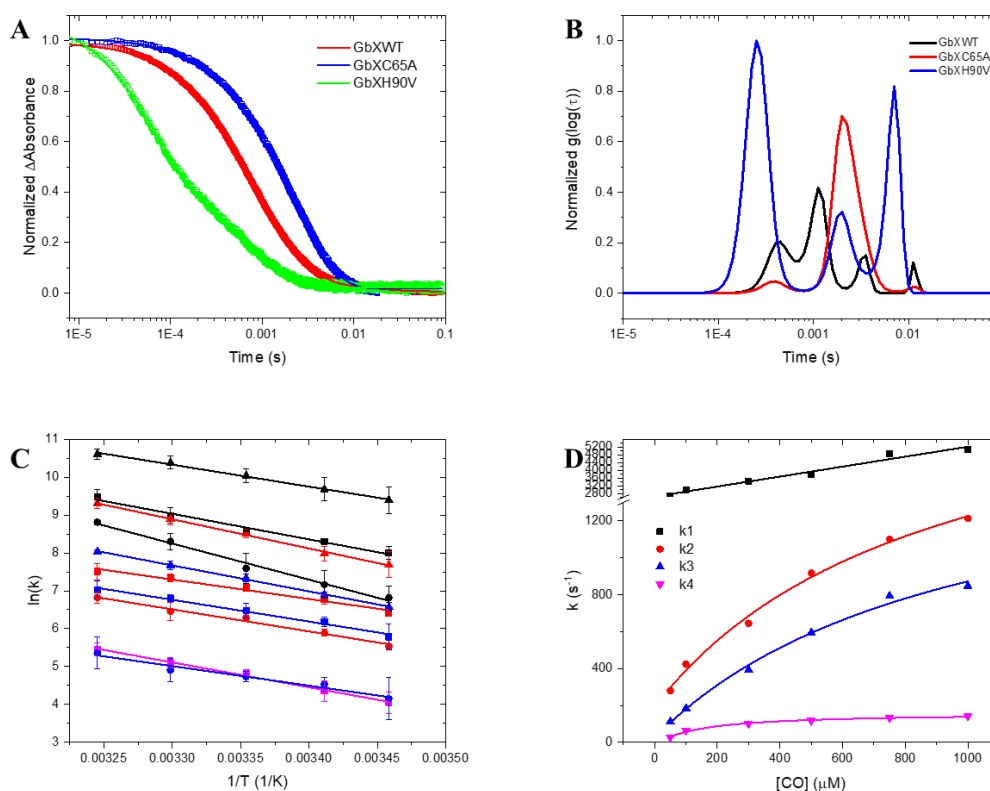


Figure 4.7. A, transient absorption traces for CO rebinding to GbX variants. B, Lifetime distribution associated with the CO rebinding to GbX variant determined by MEM approach. C, Arrhenius plot of temperature dependent CO rebinding to GbX variants, color represent different rate constant (black k1, red k2, blue k3, and purple k4) and symbol represent different GbX variants (square WT, round C65A, and triangle H90V). D, Eyring plot of temperature dependent CO rebinding to GbX variants.

observed in the GbXWT and GbXC65A mutant whereas the third rate constant, $k_3 = 1 \pm 0.06 \mu\text{M}^{-1} \text{s}^{-1}$ is very similar to the value of k_2 for ligand binding to GbXWT.

Comparing the averaged rate constant (k_{ave}) of GbX variants, the average rate constant for CO rebinding to GbXWT is $1.4 \mu\text{M}^{-1} \text{s}^{-1}$ which is around three fold larger than the average rate constant for CO rebinding to GbXC65A, $0.5 \mu\text{M}^{-1} \text{s}^{-1}$, but almost eight fold smaller than the average rate constant for CO binding to GbXH90V, $10.4 \mu\text{M}^{-1} \text{s}^{-1}$. These results indicate the internal disulfide bridge and distal histidine play a role in modulating the ligand binding to GbX. Interestingly, the k_{ave} of GbXWT is close to the

k_{ave} of hhMb but significantly smaller than the rate constant for CO binding to rice Hb as well as hCygb. From the temperature dependence of the individual rate constants,

	A ₁ (%)	k ₁ ($\mu\text{M}^{-1}\text{s}^{-1}$)	A ₂ (%)	k ₂ ($\mu\text{M}^{-1}\text{s}^{-1}$)	A ₃ (%)	k ₃ ($\mu\text{M}^{-1}\text{s}^{-1}$)	A ₄ (%)	k ₄ ($\mu\text{M}^{-1}\text{s}^{-1}$)	k _{ave} ($\mu\text{M}^{-1}\text{s}^{-1}$)
GbXWT (decay)	21±2	4.0±0.3	57±3	0.87±0.09	17±1	0.49±0.06	5±2	0.08±0.02	1.4
GbXWT (MEM)	35±2	2.3±0.07	47±2	0.83±0.05	12±0.3	0.24±0.06	6±0.5	0.06±0.03	1.2
GbXC65A (decay)	15±4	1.4±0.5	81±3	0.36±0.03	4±3	0.09±0.02	N/A	N/A	0.5
GbXC65A (MEM)	5±2	2.9±0.4	94±2	0.39±0.07	2±0.5	0.06±0.03	N/A	N/A	0.5
GbXH90V (decay)	56±1	16.9±5.0	22±4	3.0±0.6	22±4	1±0.06	N/A	N/A	10.4
GbXH90V (MEM)	46±18	29.1±10.5	30±13	6.0±5.5	24±9	1.1±0.2	N/A	N/A	15.4
*hhMb	N/A	N/A	N/A	N/A	N/A	N/A	N/A	N/A	0.5
†rHb	N/A	N/A	N/A	N/A	N/A	N/A	N/A	N/A	5.0
‡hCygb	1.4	325	98.6	7.5	N/A	N/A	N/A	N/A	11.9

Table 4.4. Rate constants for CO binding to GbX variants obtained by fitting the experimental data by exponential decay model and MEM analysis at 20°C. (*)(Belogortseva et al., 2007),†(Butcher et al., 2017), ‡(Astudillo et al., 2013))

the activation energy, log pre-exponential factor, reaction enthalpy, and reaction entropy was extrapolated (figure 4.7 C and table 4.5). The activation energy for CO binding to GbX variants is similar within the experimental error for all variants studied suggesting the similar activation barrier for CO binding to heme iron, ~ 10 kcal mol⁻¹. This activation barrier is higher than the barrier for CO binding to horse heart Mb (8.5 kcal mol⁻¹) and human Ngb (4.5 kcal mol⁻¹). Analogously, activation enthalpy for CO binding to GbX, $\Delta H^\ddagger = 10$ kcal mol⁻¹ is slightly increased compare to that observed for CO binding to horse heart Mb (~ 7.1 kcal mol⁻¹) and rice Hb (~ 8 kcal mol⁻¹). Notably, the overall activation entropy for CO binding to GbXWT is higher than that determined for

hhMb and rHb, suggesting distinct structural reorganization upon CO binding to GbX compare to other globins.

		E_a (kcal mol ⁻¹)	Log(A)	ΔH^\ddagger (kcal mol ⁻¹)	ΔS^\ddagger (cal mol ⁻¹ K ⁻¹)
GbXWT	k1	13.5±3.3	13.7±2.5	11.0±1.9	-4.3±6
	k2	10.3±2.4	10.6±1.8	12.2±5.4	-3.4±18
	k3	11.2±4.4	11.1±3.2	12.8±4.3	-2.5±14
	k4	12.8±4.6	11.5±3.3	14.2±4.6	-1.2±15
GbXC65A	k1	18.6±3.3	17.0±2.3	18.0±3.3	16.8±10
	k2	11.7±1.9	11.4±1.6	11.1±1.9	-8.9±6
	k3	10.0±6.4	9.4±4.7	10.3±6.4	-14.2±21
GbXH90V	k1	11.2±2.1	12.6±1.4	10.6±2.1	-2.9±6.4
	k2	15.0±1.9	14.6±1.4	14.4±1.9	6.7±5.8
	k3	13.6±1.5	13.1±1.1	14.3±0.9	2.6±4.7
*rHb1WT	k	8.5±0.4	N/A	8.0±0.4	-28±1.3
†hhMb	k	N/A	N/A	7.1±0.8	-22.4±2.8

Table 4.5. Activation energy, log pre-exponential factor, activation enthalpy, and activation entropy of temperature dependent CO rebinding to GbX variants. (*(Butcher et al., 2017), †(Mikšovská et al., 2003))

The rates for CO association to GbX were also monitored as a function of CO concentration and the plots of the apparent rate constants as a function of CO concentration are shown in Figure 4.8. For CO binding to GbXH90V mutant, all three rate constants exhibit a linear dependence on the ligand concentration in agreement with one step CO binding. The experimental data were analyzed using equation 3.45

$$k_{app} = k_{on}[CO] + k_{off} \quad (\text{Eq 3.45})$$

where k_{app} is the observed rate constant for the formation of the CO-GbX complex, k_{on} and k_{off} are the elementary rate constants. The individual rate constants are summarized in Table 4.6 and were used to calculate the equilibrium dissociation constants, K_D , for each individual step.

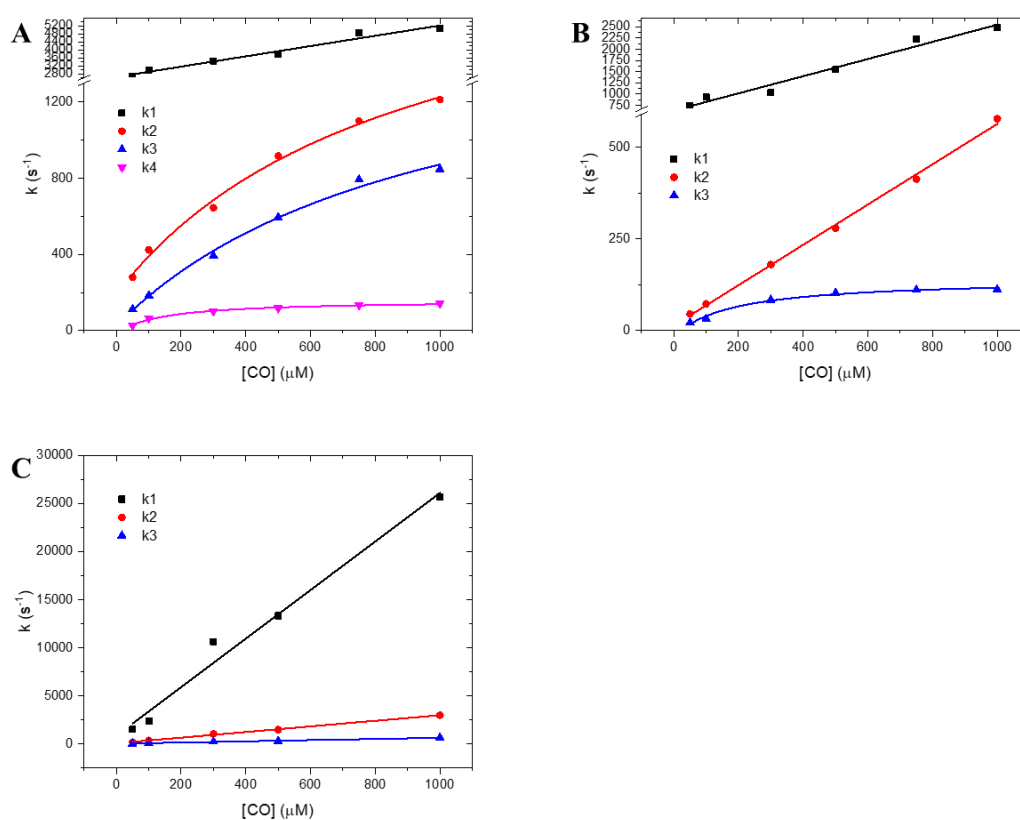


Figure 4.8. Logarithmic plots of the rate constants for CO rebinding to GbXWT (A), GbXC65A (B), and GbXH90V (C) as a function of CO concentration, experiment was performed by 20 μM protein in 50mM TrisHCl, pH 7, at 25°C.

The plot of the apparent rate constants for the ligand binding to GbXWT and GbXC65A mutant are more complex than for GbXH90V mutant. In case of CO binding to GbXC65A mutant, the rate constants k_1 and k_2 exhibit a linear dependence on the

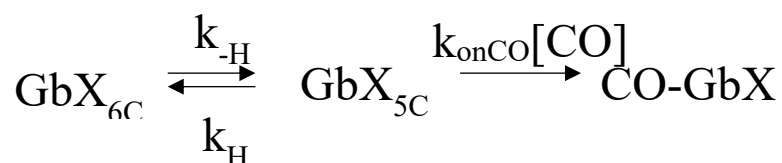
CO concentration, in agreement with the CO directly binding to a five-coordinate heme iron in a single step reaction, in a similar way as observed for GbXH90V mutant.

	k_{on}^{CO} ($\mu\text{M}^{-1} \text{s}^{-1}$)	k_{off}^{CO} (s^{-1})	K_{dCO} (μM)	
GbXWT k1	2.6 ± 0.2	2639 ± 128	1024.8 ± 128	
GbXC65A k1	1.9 ± 0.2	636 ± 91	344 ± 84	
GbXC65A k2	0.55 ± 0.01	14 ± 8	26 ± 15	
GbXH90V k1	25 ± 2	859 ± 992	38 ± 43	
GbXH90V k2	2.9 ± 0.1	80 ± 51	29 ± 19	
GbXH90V k3	0.62 ± 0.03	27 ± 17	45 ± 30	
#Mb	0.53	0.019	0.03	
	k_{on}^{CO} ($\mu\text{M}^{-1} \text{s}^{-1}$)	k_{on}^{His} (s^{-1})	k_{off}^{His} (s^{-1})	K_{aHis}
GbXWT k2	1122	382989	1585	241
GbXWT k3	79	63033	1577	79
GbXWT k4	105	20799	168	104
GbXC65A k3	21	5630	151	37
*rHb1	6.8	75	40	1.9
*SynHb	90	4200	14	300
*hNgb	40	>2000	2.3	~1000
*hCygb	5.6	430	0.5	860

Table 4.6. Rate and equilibrium constants for CO binding to GbX variants. (#(Rohlfs et al., 1990), *(Smaghe et al., 2006))

From the linear fit of the experimental data, the values of k_{on} and k_{off} for each individual binding step were extrapolated (Table 4.6). Interestingly, the equilibrium dissociation constant for CO association to GbXC65A mutant, that was determined based on the k_{on} and k_{off} values for the second kinetic step, $K_D = 26 \pm 15 \mu\text{M}$, is comparable to that observed for CO binding to distal histidine mutant. On the other

hand, the equilibrium dissociation constant determined from the individual rate constants for the first step is about ten times larger than that determined from the individual rate constants for the second step or the equilibrium dissociation constant for CO binding to GbXC65A mutant. In case of WT, the plot of the k_{obs} as a function of the CO concentration is linear only for k_1 . As described previously, the k_{on} and k_{off} values were extrapolated from the linear fit of the experimental data and used to determine the equilibrium dissociation constant, $K_D = 1024 \pm 128 \mu\text{M}$. The saturation plots of k_{obs} as a function of CO concentration observed for GbXWT and GbXC65A mutant indicate, that the CO binding occurs as a two step process and can be described according to Scheme 1:



$k_{-\text{H}}$ and k_{H} are the individual rate constant for the distal histidine dissociation and binding, respectively, and k_{onCO} is the rate for CO binding. Using steady-state approximation approach, the observed rate constant depends on the ligand concentration according to equation 3.46:

$$k_{obs,CO} = \frac{k_{-\text{H}}k_{\text{on}}^{\text{CO}}[\text{CO}]}{k_{\text{H}}+k_{-\text{H}}+k_{\text{on}}^{\text{CO}}[\text{CO}]} \quad (3.46)$$

The results of the analysis of the rate constant using Eq 3.46 are provided in Table 4.6.

The affinity constant of distal histidine (K_{aHis}) to GbXWT is around 140 which is almost four-fold higher than the affinity constant for the distal histidine in GbXC65A,

suggesting that the disruption of the internal disulfide bridge further decreases the affinity of distal histidine to heme iron. Surprisingly, the k_{on}^{CO} and K_{aHis} determined for GbXWT are very close to these values measured for pant hexa-coordinate globin, SynHb. These data suggest that GbX interacts with CO in a similar way as observed previously in some plants hemoglobins.

4.2.6 CO dissociation from GbX

The quantum yield for bimolecular CO dissociation from CO-GbX was determined as described in material and methods. The observed quantum yields are similar to quantum yields determined previously for CO dissociation from CO-Ngb and CO-Cygb and for all constructs studied the bimolecular quantum yield is temperature dependent (Figure 4.9). The quantum yield of CO from GbX variants are temperature dependent and ranges from 0.55 to 0.65 between 16°C to 35°C in case of GbX WT.

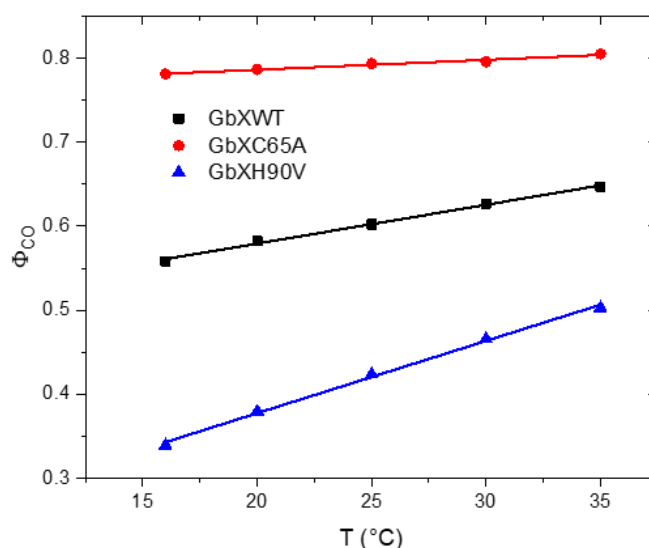


Figure 4.9. CO quantum yield for bimolecular dissociation from GbX variants as a function of temperature.

In contrast, the quantum yield for bimolecular CO dissociation from GbXC65 is higher and ranges from 0.78 to 0.80. These results suggest that the presence of the internal disulfide bond decreases the internal barrier for CO geminate re-binding. The quantum yield for the CO bimolecular dissociation from CO GbXH90V is smaller and ranges from 0.33 to 0.50 in the temperature range studied. These results suggest that the absence of the distal histidine residue significantly facilitate the CO geminate re-binding.

Photo-acoustic calorimetry experiments were conducted to investigate the reaction enthalpy and volume changes upon the dissociation of CO from GbX variants. Figure 4.10 show the overlay of normalized acoustic traces of CO bound GbX variants and the reference. There is significant phase shift between the sample acoustic wave and

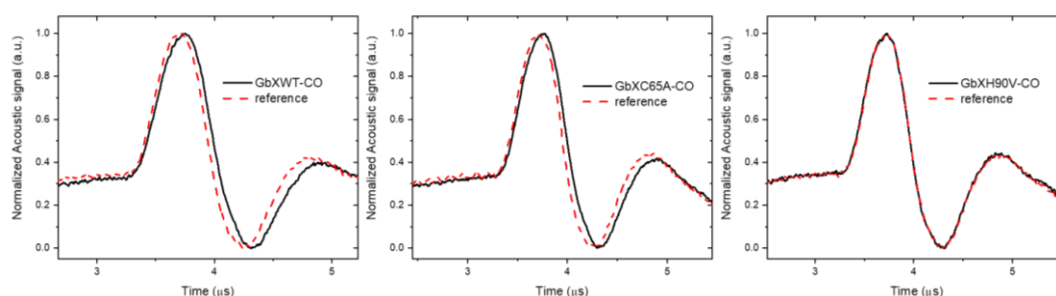


Figure 4.10. Overlay of normalized acoustic traces of CO bound GbX variants with reference. reference acoustic wave in both GbXWT and GbXC65A, suggesting that the dissociation of CO from the heme pocket is a multi-step process. No phase shift was observed for GbXH90V, indicating fast CO escape from the distal cavity ($\tau < 50$ ns) following the breakage of the Fe-CO bond. Deconvolution of the acoustic traces reveals two distinct phases for CO escape from GbXWT and GbXC65A: 1) a prompt phase (τ_1

< 50 ns) which represents the photo-cleavage of the CO-Fe bond and ligand relocation within the distal cavity and possibly its migration into distant hydrophobic cavities, and 2) a kinetic step with a lifetime $\tau_2 = 137$ ns at 20 °C that can be associate with CO escape into the surrounding solvent. The activation thermodynamic parameter (ΔH^\ddagger and ΔV^\ddagger) for CO release from GbX variants were obtained using Eyring plot (Figure 4.11) for τ_2 parameters. Table 4.7 summarizes the observed values for the reaction and activation parameters associated with the photo-dissociation of Fe-CO bond and subsequent ligand escape from the protein matrix in GbX variants as well as previously reported data for Cygb and Mb. The activation enthalpy for CO escape from the protein matrix in GbXWT and Cys65 mutant are very similar to Mb and CygbWT pointing towards a similar activation barrier for CO escape from globins. However, the activation entropy of CO escape from GbXWT and Cys65 mutant is higher than Mb and CygbWT imply

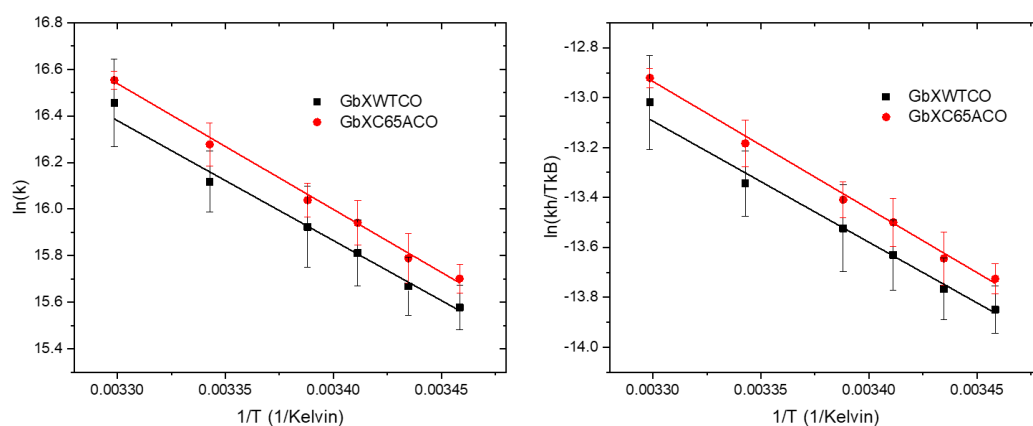


Figure 4.11. Arrhenius (left) and Eyring (right) plot of slow phase for CO photo-dissociation from GbXWT and C65A mutant.

the dissociation of CO from the distal pocket in GbX is more entropically favored. In addition, the 137 ns time constant determined for CO escape from GbXWT is similar to time constant observed for ligand escape from CygbWT ($\tau \sim 150$ ns) and ligand escape

from Mb ($\tau \sim 150$ ns at pH 3.5). The fast CO escape observed for GbX and Cygb can be associated with the increased dynamic of the distal histidine side-chain dynamics is reported to be controlled by Phe46, a residue that is conserved in the Mb and Cygb sequence.

	Temperature (°C)	ΔH_1 (kcal mol ⁻¹)	ΔV_1 (mL mol ⁻¹)	ΔH_2 (kcal mol ⁻¹)	ΔV_2 (mL mol ⁻¹)	τ (ns)	$\Delta H^\#$ (kcal mol ⁻¹)	$\Delta S^\#$ (cal mol ⁻¹ K ⁻¹)
GbXWT-CO	16-30	28±9	5±2	1.4±9	10±1.5	137	10.1±1.4	7.2±4.8
GbXC65A-CO	16-30	13±4	3.4±1.8	2.4±2.8	6.6±0.7	120	10.0±0.6	7.2±2.1
*CygbWT-CO	16-35	1.1±3.6	1.7±0.7	7.5±2.5	8.6±0.5	150	9.2±0.4	4.1±1.3
*Mb-CO	16-35	7.4±2.0	-1.7±0.5	6.9±2.9	12.1±0.7	700	10.2±0.7	4.0±2.2

Table 4.7. Reaction (ΔH and ΔV) and activation ($\Delta H^\#$ and $\Delta V^\#$) parameters associated with the photo-dissociation of Fe-CO bond and subsequent ligand escape from the protein matrix in GbX variants. (*(Astudillo et al., 2013))

Since this phenylalanine is also conserved in GbX, it is possible it could also play a role in modulating the distal histidine orientations. The thermodynamic parameters for CO escape from GbX variants were determined by plotting $E_{hv}(\phi - 1) / \Phi$ as a function of the temperature dependent parameter (C_{pp}/β), according to Eqs. 3.33 and 3.34 (Figure 4.11) and were listed in Tables 4.7 and 4.8.

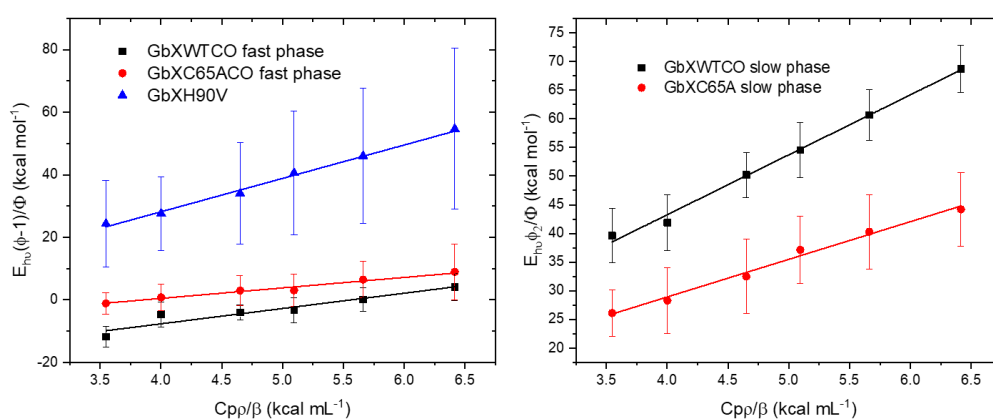


Figure 4.12. Plot of $\phi_1 E_{hv}$ versus C_{pp}/β for the prompt phase (left) and the slow phase (right) for CO photo-dissociation from GbX variants.

The photo-cleavage of the Fe-CO bond and subsequent ligand release from GbXWT are associated with an enthalpy change of $\Delta H_1 = 28 \pm 9 \text{ kcal mol}^{-1}$ and a negligible volume change $\Delta V_1 = 5 \pm 2 \text{ mL mol}^{-1}$. The accompanying enthalpy change is reflecting the enthalpy of the cleavage of Fe-CO bond ($\Delta H_{\text{Fe-CO}} = 17 \text{ kcal mol}^{-1}$). The following ligand escape from the protein matrix is slightly endothermic ($\Delta H_2 = 1.4 \pm 9 \text{ kcal mol}^{-1}$) and leads to a small volume increase ($\Delta V_2 = 10 \pm 1.5 \text{ mL mol}^{-1}$). The overall enthalpy changes and volume change observed for CO release from GbX variants as well as other previously studied globins are listed in Table 4.8. In order to have a better understanding of structural changes associated with the CO photo-dissociation, the measured reaction volume and enthalpy changes were used to estimate structural enthalpy change (ΔH_{str}) and structure volume change (ΔV_{str}) using Equation 3.47 and 3.48.

$$\Delta H_{\text{total}} = \Delta H_{\text{Fe-CO}} + \Delta H_{\text{str}} \quad (\text{Eq 3.47})$$

$$\Delta V_{\text{total}} = \Delta V_{\text{CO}}^\circ + V_{5c}^\circ \text{GbX} - V_{6c}^\circ \text{GbXCO} \quad (\text{Eq 3.48})$$

Where V_{CO}° is the partial molar volume of CO (37.3 mL mol^{-1}), $V_{\text{str}} = V_{5c}^\circ \text{GbX} - V_{6c}^\circ \text{GbXCO}$ which describes the difference between the partial molar volume of the penta-coordinate GbX and CO-bound GbX (Moore et al., 1982). Considering the fluctuation of the values, the structure enthalpy changes of GbXWT ($\Delta H_{\text{str}} = 12 \pm 13 \text{ kcal mol}^{-1}$) is comparable in GbXC65A ($\Delta H_{\text{str}} = -2 \pm 5 \text{ kcal mol}^{-1}$) and GbXH90V ($\Delta H_{\text{str}} = -2 \pm 5 \text{ kcal mol}^{-1}$), imply the enthalpy change upon the dissociation of CO is mainly the result of iron CO bond breakage. On the other hand, the structure volume

	Temperature (°C)	ΔH_{total} (kcal mol ⁻¹)	ΔH_{str} (kcal mol ⁻¹)	ΔV_{total} (mL mol ⁻¹)	ΔV_{str} (mL mol ⁻¹)	ΔV_{str+H_2O} (mL mol ⁻¹)
GbXWT-CO	16-30	29±13	12±13	15±2.5	-22.3±2.5	-2.3±2.5
GbXC65A-CO	16-30	15±5	-2±5	10±2	-27.3±2	-9.3±2
GbXH90V-CO	16-30	15±5	-2±5	11±5	-26.3±2	-8.3±2
*CygbWT-CO	16-35	9±4	-8±4	10.3±1.2	-27±1.2	-9±1.2
*NgbWT-CO	16-35	20±4	3±4	13.4±0.9	-23.9±0.9	-5.9±0.9
*Mb-CO	16-35	14±3	-3±3	10.4±0.7	-26.9±0.7	-8.9±0.7
†Hb-CO	16-35	18±2.9	1±2.9	23.4±0.5	-13.9±0.9	4.1±0.9

Table 4.8. Total volume and enthalpy changes associated with the CO dissociation from GbX variants as well as Cygb, Ngb, Mb, and Hb. (* (Astudillo et al., 2013), † (Peters et al., 1992))

change in GbXWT ($\Delta V_{str} = -22.3 \pm 2.5$ mL mol⁻¹) is slightly less than both GbXC65A ($\Delta V_{str} = -27.3 \pm 2$ mL mol⁻¹) and GbXH90V ($\Delta V_{str} = -26.3 \pm 2$ mL mol⁻¹). It was reported that water molecules could enter the distal pocket of Mb when exogenous ligand is not present. It is possible that after the dissociation of CO from the GbX, a water molecule could enter the distal pocket. Taking into account the water molecule, the ΔV_{str+H_2O} of GbXWT, GbXC65A and GbXH90V is -2.3 ± 2.5 mL mol⁻¹, -9.3 ± 2 mL mol⁻¹, and -8.3 ± 2 mL mol⁻¹, respectively. Therefore, the overall structure of GbXWT remain unchanged upon the dissociation of CO while there is small contraction of the protein conformation in both GbXC65A and GbXH90V. Interestingly, while shown a similar structure enthalpy change to other globins, the negligible structure volume change observed for CO release from GbXWT is distinct from other globins studied using PAC indicating distinct structural changes upon CO dissociation. This is also consistent with distinct activation entropy changes observed for CO binding to GbX variants.

4.3 Discussion

The results presented here demonstrate several distinct properties of GbX. Interestingly, this protein demonstrates a high stability towards pH as the pH_{mid} value for the pH induced unfolding of GbXWT is significantly lower than that observed previously for pentacoordinate hhMb as well as hexacoordinate Ngb suggesting an increased stability of this protein. Interestingly, the increased stability cannot be fully attributed to coordination bond between the distal histidine and heme iron as GbXH90V construct exhibits increased pH stability with respect to Mb. This suggest more stronger interaction between the proximal histidine and heme iron in GbX.

Affinity constants for CN^- binding to GbX variants are significantly lower than that observed for other hexa-coordinate globins, pointing towards lower reactivity of iron atom in GbX towards this ligand. Interestingly, two affinity constants determined for CN^- association to GbXC65A mutant are consistent with this construct adopting two conformations in the met form. The low cyanide affinity conformation in the cysteine mutant is similar to WT while the high cyanide affinity conformation binds CN^- with the similar affinity as the GbXH90V mutant, suggesting that in the high affinity conformation, the distal histidine is weakly associated to the heme iron. Previous studies shown that the disulfide bridge in Cygb modulates its ligand affinity and the disruption of the disulfide bridge leads to the rearrangement of the E helix where distal histidine is located and ultimately change the position of distal histidine. Also, crystallographic study of Cygb structure revealed the existence of two different

conformations of the protein with two distinct orientations of the distal histidine. Analogously, the disruption of the disulfide bridge in GbX may lead to two different protein conformations with distinct position of distal histidine that leads to two different affinities for CN^- binding.

In addition, the CO binding to GbX is heterogenous, with 4 different rate constants resolved by transient absorption spectroscopy. In general, the removal of the disulfide bond decreases the rate constant for CO rebinding three times with respect to GbXWT, whereas the replacement of distal histidine increases the CO rebinding rate eight times. More importantly, the kinetics are significantly slower compare to the CO rebinding kinetics to Cygb. The fast rate constants for CO binding to Cygb were associated with a highly reactive heme iron in this protein. The slow rebinding observed for GbX is consistent with the heme iron reactivity being similar to Mb or rice Hb. Besides, the CO concentration dependent experiment show a high dissociation constant of CO and a small affinity constant for distal histidine binding to GbX heme iron, further supporting the hypothesis that the heme iron inside GbX is less reactive compare to other vertebrate globins.

The quantum yield for bimolecular CO rebinding to GbX variants reveal that the disruption of internal disulfide bridge promotes the CO to escape from the protein by increasing the energy barrier for the geminate CO rebinding whereas the removal of distal histidine facilitates the CO geminate rebinding. Photo-acoustic calorimetry data shows that the CO escape from GbXWT and GbXC65A is a two-step process with a

time constant around 130 ns which is similar to time constant measured for CO escape from Cygb and Mb at pH 3.5. The activation barrier for CO dissociation in GbX is similar to Cygb and hhMb but with a higher activation entropy. In addition, the structure enthalpy change for CO escape from GbX is similar to other globins while the structural volume change is less than that measured in other globins studied by PAC. These results imply a distinct structural change accompanying CO dissociation from the GbX protein matrix.

5 CHARACTERIZATION OF THE CONFORMATION, REGULATION, ORIENTATION, AND HEME ACCESIBILITY IN HEXACOORDINATE GLOBINS BY USING FLUORESCENT HEME ANALOG.

5.1 Introduction

The development of a method to extract the heme prosthetic group from globin proteins is of paramount importance since it allows to investigate the interaction between the heme group and the surrounding amino acid residues in the heme cavity, as well as how these interactions affect or regulate the function of the heme protein, using NMR spectroscopy and fluorescence techniques (Fanelli et al., 1958; Teale, 1959). The native holoMb and the reconstituted FePPIX-Mb (heme group extracted from the native protein and reconstituted with the synthesized iron protoporphyrin IX) present no differences in terms of spectra properties, confirming the reversibility of the recombination reaction (HARRISON & BLOUT, 1965). Other than iron protoporphyrin IX, other porphyrin-based molecules can be used to replace the heme prosthetic group inside the heme protein. By using heme analogs, the role of the peripheral side chains of the heme group can be examined to determine their impact on structure-function relation between the heme and globin scaffold. For instance, heme-7-propionate affects binding between the proximal histidine and heme iron in horse heart myoglobin, while removing heme-6-propionate can disrupt hydrogen bonding

network in the distal pocket which impacts the autoxidation of the heme (Hayashi et al., 2002).

Furthermore, fluorescent heme analogs such as free based porphyrin or zinc protoporphyrin IX (ZnPPIX) are also used to study structural function relationship of the proteins by applying fluorescence techniques. Due to the iron coordination to the porphyrin ring, the iron heme is non-fluorescent. In addition, due to a significant spectral overlap between the emission spectrum of tryptophan and absorption spectrum of heme in the native state, the iron in the porphyrin ring efficiently quenches the intrinsic tryptophan fluorescence (Weber & Teale, 1959). Thus, replacement of the native heme with its fluorescent analogs allows fluorescence- and phosphorescence-based characterizations of structural and dynamic properties of heme proteins. ZnPPIX reconstituted hemoglobin were used to investigate the allosteric effects, while ZnPPIX reconstituted Mb were used to study its interactions with cytochrome b5 (Liang et al., 2002; Naito et al., 1998).

Quenching ZnPPIX reconstituted globins with small molecules provides a way to measure how small molecules diffuse through the protein matrix without the process being influenced by the actual binding step (Barboy & Feitelson, 1987). By introducing a chemical modification or mutation of the protein, specific amino acid residues or structural features can be examined and their impact on the ligand diffusion or migration pattern in the proteins can be determined (Aono et al., 1995). In addition, ZnPPIX has a longer triplet state lifetime than other metallo-porphyrins and O₂ is well

known as a highly efficient quencher of excited triplet states (Aono et al., 1995). Therefore, triplet state quenching studies of ZnPPIX reconstituted globins allow to study the mechanism of O₂ diffusion and migration into the heme bind site. This is particularly important since O₂ is an important physiological molecule (Barboy & Feitelson, 1987).

It was previously shown by our group that hexa-coordinate globins can be successfully reconstituted by ZnPPIX and the incorporated fluorescent analogue exhibits fluorescent properties that are distinct from those observed previously for penta-coordinate proteins, Mb and Hb (Tangar et al., 2019). Here we report reconstitution of several variants of Ngb and Cygb, with several ZnPPIX to investigate how conformational changes in terms of removal the distal histidine coordination and the absence of the internal disulfide bond affect the heme orientation and ligand diffusion into the heme cavity.

5.2 Results

5.2.1 Steady-state UV-vis absorption spectroscopy

Steady-state UV-vis absorption spectra of reconstituted ZnPPIXCygb, ZnPPIX-Ngb as well as their mutants are shown in Figure 5.1. Incorporation of ZnPPIX into wild type Cygb results in a Soret band maximum at 428 nm, β band at 553 nm and a split α band situated at 587 nm and 595 nm. All Cygb mutants showed a comparable absorption spectrum with a similar location of λ_{\max} of the Soret band and β band. Interestingly, the absorption spectrum for ZnPPIX-CygbC38S and ZnPPIX-

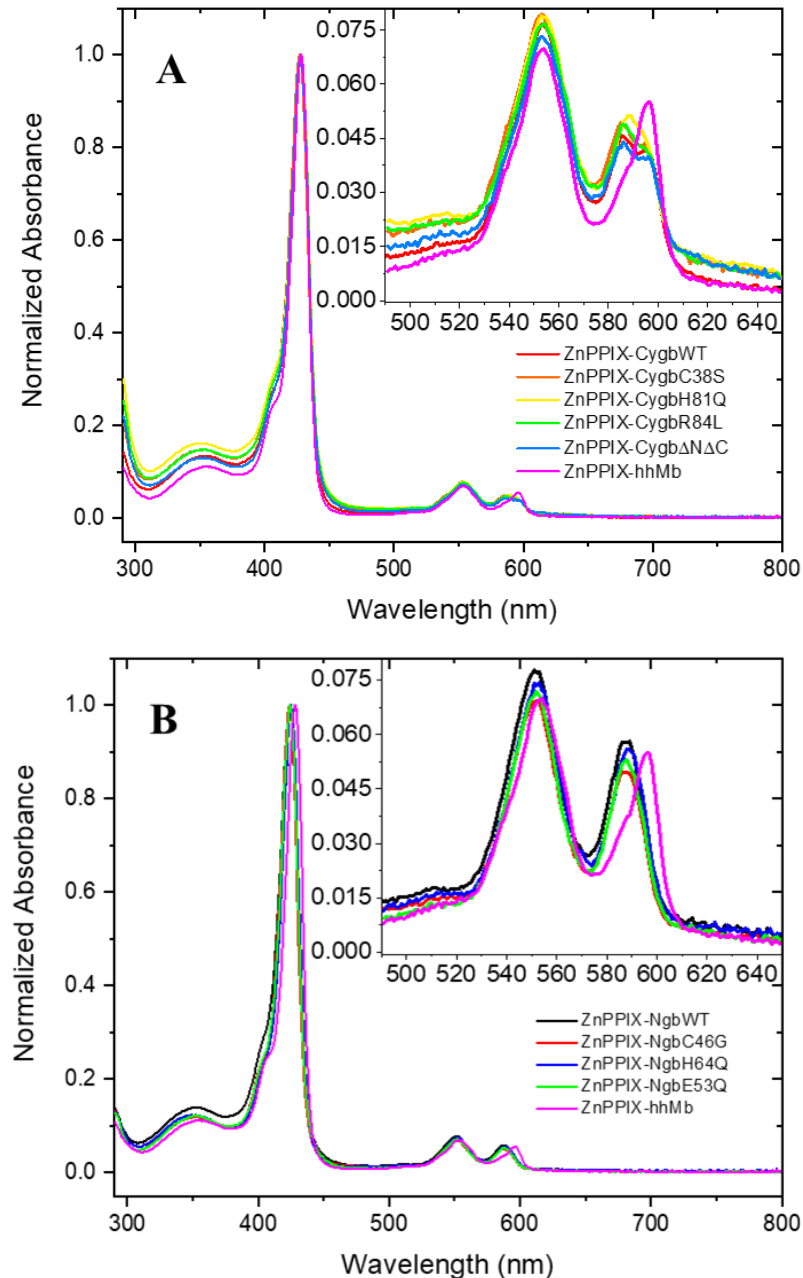


Figure 5.1. Normalized steady-state absorption spectra of ZnPPIX-hhMb and ZnPPIX-Cygb variants (A) and ZnPPIX-Ngb variants (B) in 50 mM TrisHCl pH 7.0.

Cygb Δ N Δ C showed similar α band split as observed in the absorption spectrum of the CygbWT. In the absorption spectrum of ZnPPIX-CygbR84L, the peak located at 595 nm has a lower intensity than the peak at 586 nm. Notably, the absorption spectrum for the ZnPPIX-CygbH81Q mutant exhibited a single α -band that is broader than an α -band observed in ZnPPIX-Mb. On the other hand, the absorption spectrum of reconstituted

	Soret	β	α
ZnPPIX-hhMb	428 nm	554 nm	595 nm
ZnPPIX-CygbWT	428 nm	553 nm	585/594 nm
ZnPPIX-CygbC38S	427 nm	553 nm	585/595 nm
ZnPPIX-CygbH81Q	428 nm	553 nm	588 nm
ZnPPIX-CygbR84L	428 nm	554 nm	586* nm
ZnPPIX-Cygb Δ N Δ C	428 nm	553 nm	586/596 nm
ZnPPIX-NgbWT	425 nm	552 nm	588 nm
ZnPPIX-NgbC46G	424 nm	552 nm	587 nm
ZnPPIX-NgbH64Q	425 nm	553 nm	588 nm
ZnPPIX-NgbE53Q	424 nm	552 nm	588 nm

Table 5.1. Summary of UV-vis absorption maxima for ZnPPIX reconstituted hhMb, Cygb and Ngb variants. Specifically, CygbR84L shown a shoulder rather than a peak at \sim 595 nm.

NgbWT showed a Soret band at 425 nm, with β and α bands centered at 552 and 588 nm, respectively. All Ngb mutants showed identical position of the Soret band as well as β and α bands to the wild type protein. Reconstituted ZnPPIX-hhMb was also prepared and characterized as a control and its absorption spectrum was characterized by a Soret band at 428 nm, with β and α bands centered at 554 and 595 nm which are comparable to the previously published data (ALBANI & ALPERT, 1987).

5.2.2 Steady-state fluorescence emission spectra

Fluorescent emission spectra revealed that, upon excitation at 421 nm, steady-state emission of ZnPPIX reconstituted wild type Cygb exhibits a narrow peak at 598 nm and a broad band of weaker intensity at 649 nm (figure 5.2). Emission spectra for Cygb mutants showed a comparable λ_{\max} for both peaks, but the peaks of shorter wavelength in ZnPPIX-CygbH81Q and ZnPPIX-Cygb Δ N Δ C are \sim 1 nm blue shifted compare to wild type Cygb. On the other hand, the emission spectrum of ZnPPIX-NgbWT is blue-shifted, with the one peak situated at 593 nm and the longer wavelength peak located

at 647 nm. Emission spectra for Ngb mutants show a similar λ_{max} for both emission peaks with exception of the emission spectrum for ZnPPIX-NgbC46G mutant that has the λ_{max} of the longer emission band 2 nm blue shifted compared to the ZnPPIX-NgbWT.

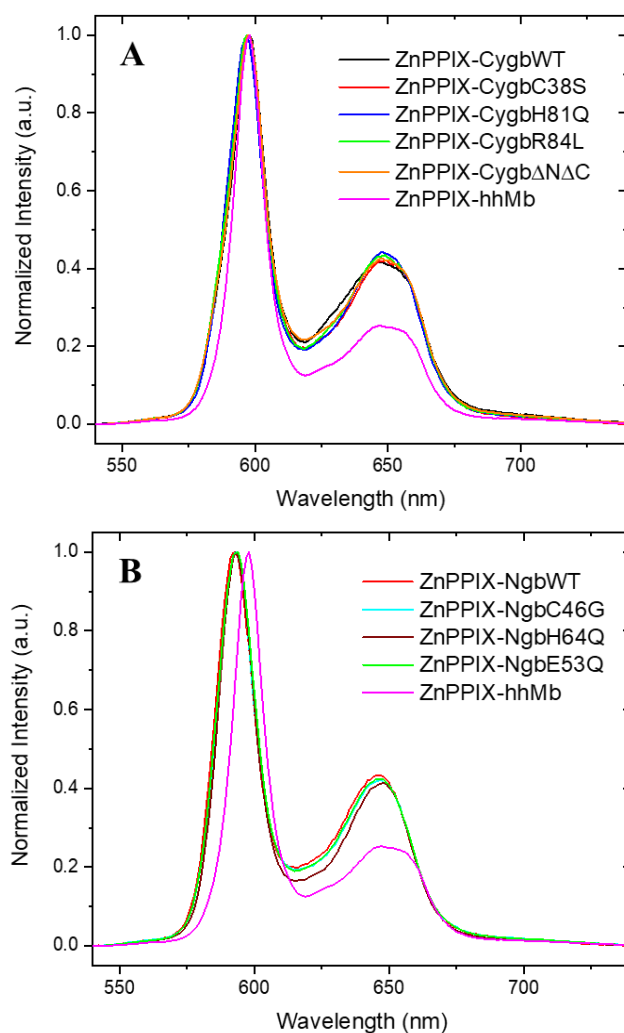


Figure 5.1. Normalized steady-state fluorescence emission of ZnPPIX-Cygb variants (A) and ZnPPIX-Ngb variants (B), using $\lambda_{\text{exc}} = 421$ nm.

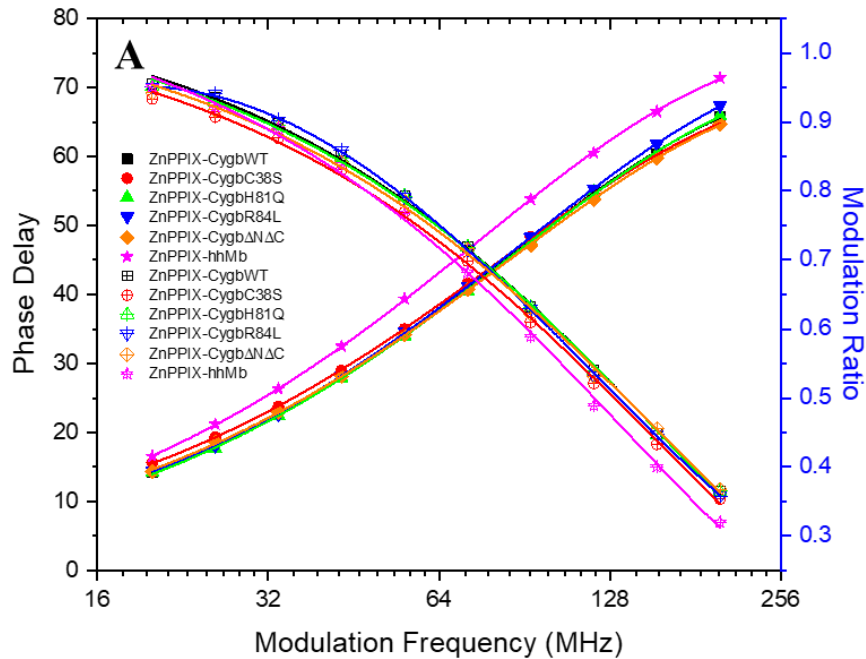
Notably, ZnPPIX-NgbH64Q 648 nm emission band is narrower compared to the ZnPPIX-NgbWT, pointing towards a less heterogenous surrounding of the fluorophore environment compared to all the mutants.

	λ_{\max_1}	λ_{\max_2}
ZnPPIX-hhMb	598 nm	650 nm
ZnPPIX-CygbWT	598 nm	649 nm
ZnPPIX-CygbC38S	598 nm	649 nm
ZnPPIX-CygbH81Q	597 nm	648 nm
ZnPPIX-CygbR84L	597 nm	649 nm
ZnPPIX-Cygb Δ N Δ C	598 nm	648 nm
ZnPPIX-NgbWT	593 nm	647 nm
ZnPPIX-NgbC46G	593 nm	645 nm
ZnPPIX-NgbH64Q	593 nm	648 nm
ZnPPIX-NgbE53Q	594 nm	646 nm

Table 5.2. Summary of fluorescence emission maxima for ZnPPIX reconstituted hhMb, Cygb and Ngb variants.

5.2.3 Fluorescence and phosphorescence lifetime

The single state lifetime of ZnPPIX reconstituted proteins was determined in the frequency mode and the plots of phase shift/modulation ratio as a function of



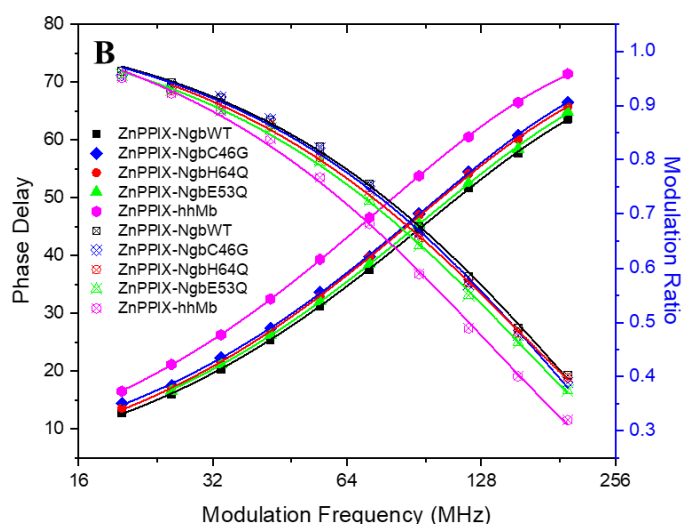


Figure 5.3. Time-resolved fluorescence in the frequency domain data determined for ZnPPIX-Cygb variants (A) and ZnPPIX-Ngb variants (B).

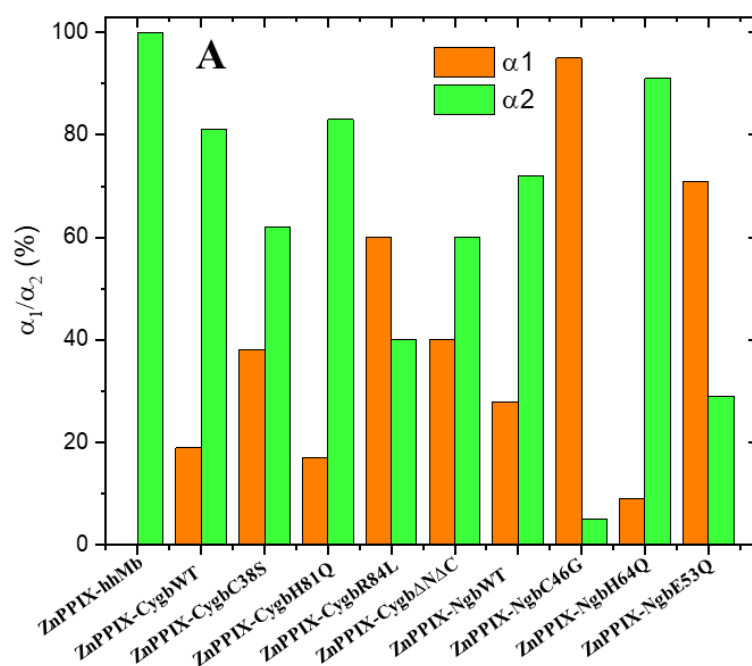
modulation frequency is shown in Figure 5.3. The data for ZnPPIX reconstituted Mb were analyzed using a single exponential decay model, whereas the results for the ZnPPIX reconstituted Ngb and Cygb constructs were analyzed using a sum of two exponential decays and the recovered decay parameters are listed in Table 5.3.

	ZnPPIX-hhMb	ZnPPIX-CygbWT	ZnPPIX-CygbC38S	ZnPPIX-CygbH81Q	ZnPPIX-CygbR84L	ZnPPIX-Cygb Δ N Δ C	ZnPPIX-NgbWT	ZnPPIX-NgbC46G	ZnPPIX-NgbH64Q	ZnPPIX-NgbE53Q
τ_1 (ns)	N/A	0.787	1.02	0.785	1.61	1.55	0.959	1.76	0.738	1.45
α_1	N/A	0.19	0.38	0.17	0.6	0.71	0.28	0.95	0.09	0.71
τ_2 (ns)	2.36	2.12	2.43	2.07	2.46	2.86	1.94	4.22	1.92	2.49
α_2	1	0.81	0.62	0.83	0.4	0.29	0.72	0.05	0.91	0.29
τ_p (ms)	15.5	14.8	11.2	13.7	13.1	n.d.	11.1	17.3	15.5	n.d.

Table 5.3. Summary of fluorescence and phosphorescence parameters of ZnPPIX-reconstituted hexacoordinate globins.

The bimodal decay observed for ZnPPIX-Cygb WT and ZnPPIX-NgbWT exhibits two distinct fluorescence lifetimes with $\tau_1 \sim 0.8$ ns and $\tau_2 \sim 2.1$ ns, and the pre-exponential factor associated with the faster decay α_1 , being ~ 0.35 and the pre-exponential factor associated with the longer lifetime, α_2 , being ~ 0.65 . ZnPPIX-CygbHis81Q mutant exhibits analogous lifetimes and associated pre-exponential

factors as ZnPPIX-Cygb WT, whereas Cygb other mutants showed an increase in both lifetimes as well as increase of the α_1 pre-exponential factor. ZnPPIX-NgbWT also exhibits a bimodal fluorescence decay with the lifetimes: $\tau_1 \sim 1$ ns and $\tau_2 \sim 2$ ns, and the pre-exponential factors $\alpha_1 = 0.28$ and $\alpha_2 = 0.72$. Compared to ZnPPIX-NgbWT, ZnPPIXNgbH64G exhibits a shorter $\tau_1 = 0.74$ ns and a smaller α_1 value of 0.1. In case of ZnPPIX-NgbC46G and ZnPPIX-NgbE53Q mutants, τ_1 increases to 1.76 ns and 1.45 ns, respectively, and the pre-exponential factor α_1 is 0.95 and 0.75, respectively. Interestingly, both residues, Cys 46 and Glu 53 are located in the CD loop of the protein, indicating that changes in this flexible loop impact the heme binding pocket. The second lifetime observed for ZnPPIXC46G is two times slower than that observed for the ZnPPIX-NgbWT, however the pre-exponential factor associated with this lifetime is small, 5%.



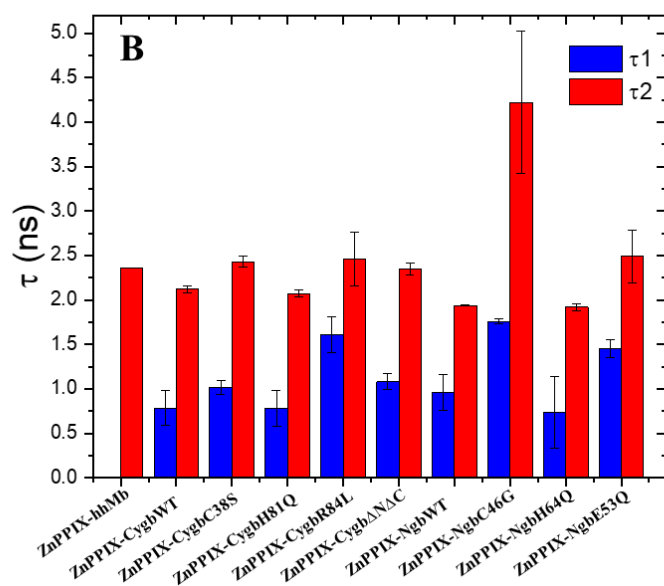


Figure 5.4. Time-resolved fluorescence in the frequency domain data determined for ZnPPIX-Cygb variants (A) and ZnPPIX-Ngb variants (B).

In addition to the characterization of the singlet lifetime of ZnPPIX, we have measured ZnPPIX triplet state lifetime by monitoring the time profile of the absorbance change of the triplet state at 447 nm. The transient absorption traces are shown in Figure 5.5 and the data were analyzed using a single exponential decay model.

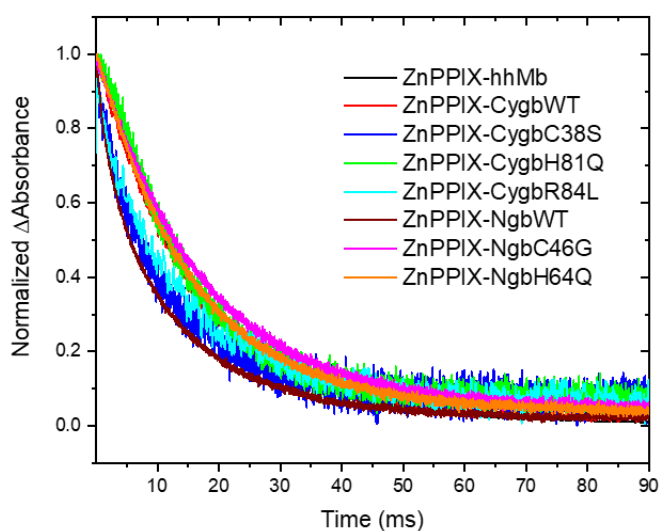


Figure 5.5. Phosphorescence decay determined for reconstituted globins. Phosphorescence decay was monitored at 447 nm.

Phosphorescence lifetime, τ_p , observed for ZnPPIX-Cygb variants varies from 11.2 ms to 14.8 ms and similar variations were observed for the triplet state lifetime of ZnPPIX-Ngb variants (from 11.1 ms to 17.3 ms). The detected lifetimes are similar to the triplet state decay of ZnPPIX-hhMb, $\tau_p = 15.5$ ms. As the ZnPPIX lifetime is strongly impacted by the presence of oxygen in the deoxygenated proteins samples, it is possible that the observed deviations in the phosphorescence lifetime reflect the presence of the residual oxygen.

5.2.4 Quenching study

Methyl viologen (MV^{2+}) has been employed previously as an efficient quencher of the singlet state emission of ZnPPIX. To characterize interactions between MV^{2+} and ZnPPIX reconstituted proteins, we have monitored absorption spectra of ZnPPIX reconstituted proteins in the presence of increasing concentration of MV^{2+} .

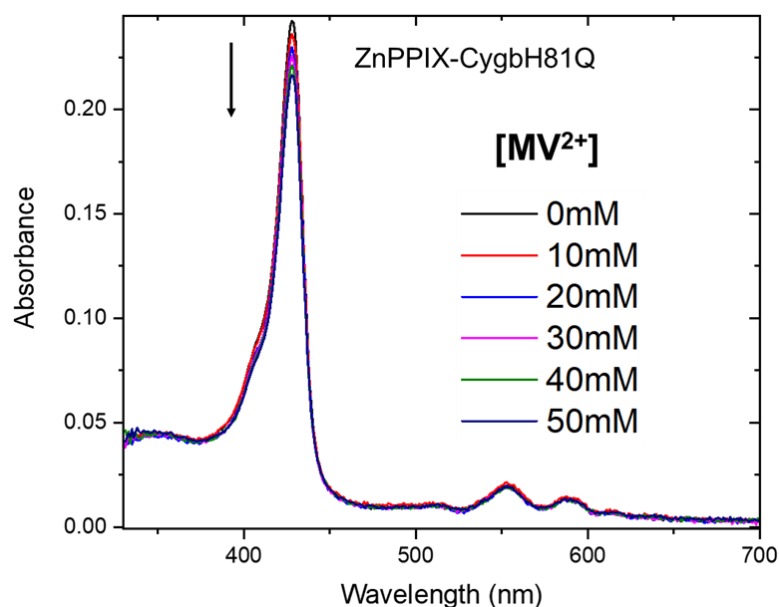


Figure 5.6. Example of UV-vis absorption spectra of ZnPPIX reconstituted protein with increasing concentration of methyl viologen. A decrease of Soret band absorbance is observed.

In the presence of the quencher, the absorbance of the Soret band decreases, indicating MV^{2+} binding to the protein, possible in the vicinity of the heme binding pocket. The impact of MV^{2+} association to ZnPPIX-CygbH81Q mutant on ZnPPIX absorption spectrum is demonstrated in Figure 5.6 and similar results were obtained for other constructs, data not shown.

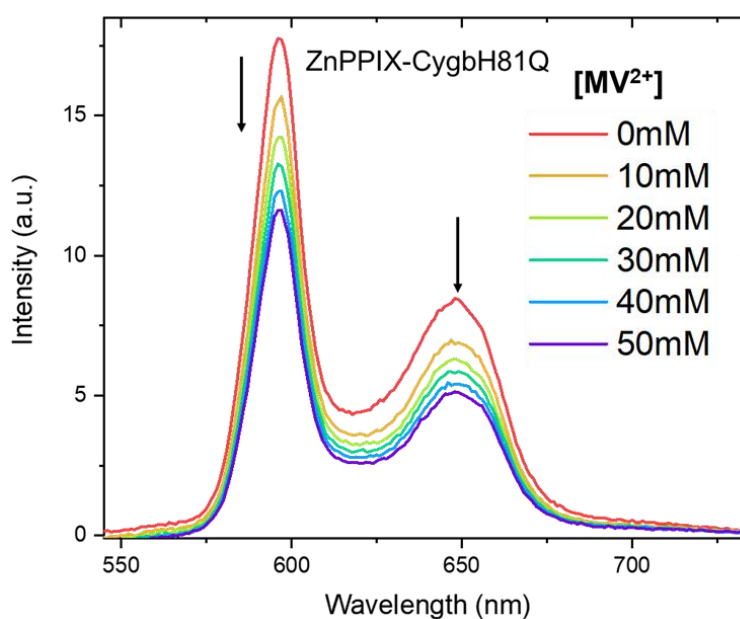


Figure 5.7. Example of fluorescence emission spectra of ZnPPIX reconstituted protein in the presence of increasing concentration of methyl viologen.

The quenching of the ZnPPIX reconstituted globins was probed by monitoring the fluorescent emission spectra at increasing concentration of the quencher (Figure 5.7). The Stern-Volmer plot was constructed by plotting the ratio of the emission intensity at zero quencher and increased quencher concentration as a function of quencher concentration and the plots are shown in Figure 5.8. The Stern-Volmer constant, K_{sv} , was determined by fitting the experimental data using a linear Stern-Volmer equation and the results are summarized in Table 5.4. The value of K_{sv} was determined to be 16.7

± 0.9 , 17.2 ± 5.3 , and $9.62 \pm 1.1 \text{ M}^{-1}$ for ZnPPIX reconstituted CygbWT, CygbC38S, CygbH81Q, respectively. Also, ZnPPIX reconstituted NgbWT has relatively larger K_{sv} value of $34.1 \pm 2.1 \text{ M}^{-1}$ while the ZnPPIX-NgbC46G and ZnPPIX-NgbH64Q showed a smaller K_{sv} values of 26.5 ± 0.76 and $25.4 \pm 11.0 \text{ M}^{-1}$, respectively.

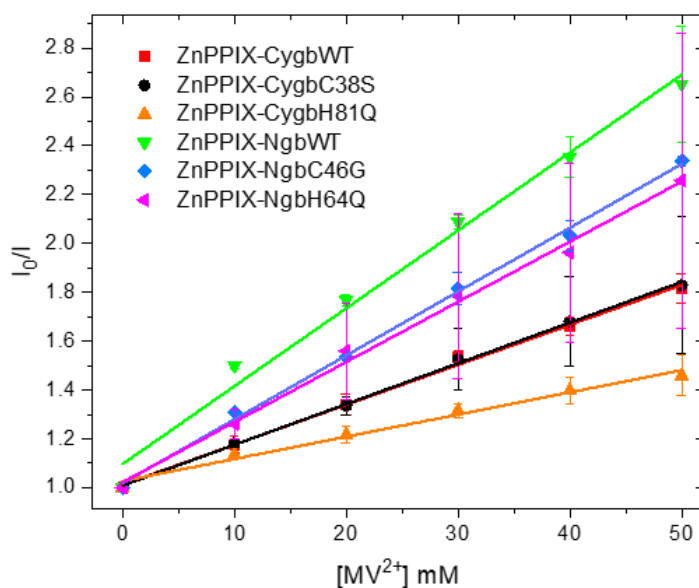


Figure 5.8. The Stern-Volmer plot for the quenching of the steady-state fluorescence of ZnPPIX reconstituted globins by methyl viologen.

In addition to monitoring quenching of the ZnPPIX singlet state, we have taken advantage of the fact that O₂ is an excellent quencher of ZnPPIX triplet state. The

Proteins	$K_{sv}(\text{M}^{-1})$
ZnPPIX-CygbWT	16.7 ± 0.9
ZnPPIX-CygbC38S	17.2 ± 5.3
ZnPPIX-CygbH81Q	9.62 ± 1.1
ZnPPIX-NgbWT	34.1 ± 2.1
ZnPPIX-Ngc46G	26.5 ± 0.76
ZnPPIX-NgbH64Q	25.4 ± 11.0

Table 5.4. Summary of Stern-Volmer constant of ZnPPIX-reconstituted hexacoordinate globins. quenching of the triplet state of ZnPPIX reconstituted globins was characterized by measuring the phosphorescence lifetime. The quantum yield of phosphorescence

emission was very low, and the triplet state emission was usually detected at low temperatures (around 100 K), making the detection of the triplet state lifetime challenging. Here, we took advantage of the fact that ZnPPIX triplet state absorbs at 447 nm and thus the triplet state lifetime can be detected by measuring the time profile of the triplet state absorbance.

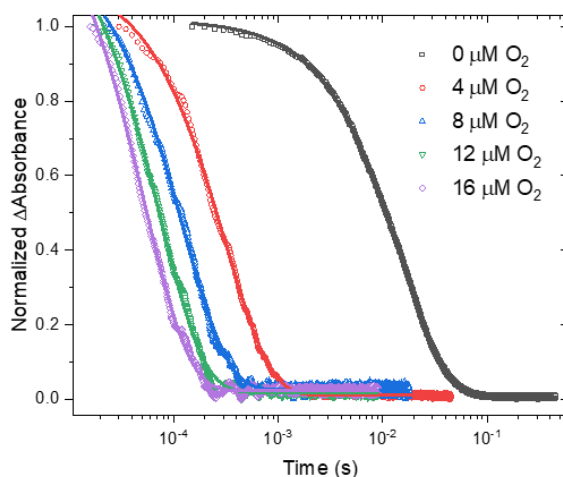


Figure 5.9. Triplet state lifetime traces of ZnPPIX-hhMb obtained by transient absorbance at varying concentration of oxygen. All traces are fitted by single exponential decay.

The triplet state quenching was monitored by measuring the triplet state lifetime as a function of the increasing concentration of oxygen. The transient absorption traces

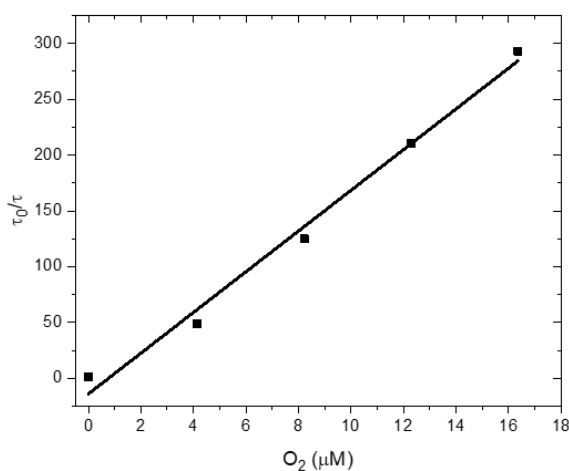


Figure 5.10. The Stern-Volmer plot for the quenching of the triplet-state phosphorescence of ZnPPIX reconstituted hhM by oxygen.

for ZnPPIX-hhMb are shown in Figure 5.9 and the corresponding Stern Volmer plot is presented in Figure 5.10. The quenching rate constant were determined from the plot of the ratio of the triplet state lifetime in the absence of quencher and in the presence of quencher. The recovered rate constants are: $k_q = 3.23 \times 10^8 \pm 0.32 \text{ M}^{-1} \text{ s}^{-1}$ for ZnPPIX-hhMb which is similar to the previous

	$k_q (\text{M}^{-1} \text{ s}^{-1})$
ZnPPIX-hhMb	$3.23 \times 10^8 \pm 0.32$
ZnPPIX-CygbWT	$3.03 \times 10^8 \pm 0.8$
ZnPPIX-NgbWT	$4.08 \times 10^8 \pm 1.39$

Table 5.5. Summary of quenching rate constant of ZnPPIX-reconstituted globins.

reported value [Barboy and Feitelson]. Also, the k_q for ZnPPIX-CygbWT is $3.03 \times 10^8 \pm 0.8 \text{ M}^{-1} \text{ s}^{-1}$ and ZnPPIX-NgbWT is $4.08 \times 10^8 \pm 1.39 \text{ M}^{-1} \text{ s}^{-1}$ that is comparable to the value obtained for ZnPPIX reconstituted hhMb.

5.3 Discussion

The reconstitution of globins with ZnPPIX combined with site-directed mutagenesis provides a powerful method to study how the prosthetic group interacts with the protein scaffold as well as with the exogenous ligands due to the high sensitivity of the fluorescent analog, ZnPPIX, to changes in its surrounding as well as to the presence of various quenchers. Steady-state absorption and fluorescence emission of the ZnPPIX-reconstituted proteins provide insight into the structural heterogeneity of the heme binding cavity. An α -band split was observed for most Cygb reconstituted

proteins while the split is compromised in CygbR84L mutant and nearly disappeared in CygbH81L mutant, suggesting that the electronic structure of ZnPPIX is sensitive to small changes in the heme binding pocket. Namely, the conformational heterogeneity of the distal histidine sidechain as well as two distinct orientations of Arg84 sidechain observed in the structure of ligand bound Cygb may contribute to the observed split of α -band in the absorption spectrum of Cygb. Compare to emission spectra of ZnPPIX-hhMb and ZnPPIX-Cygb variants, all ZnPPIX reconstituted Ngb variants shown a blue-shifted Soret bands by 3 nm. Such hypsochromic shift in the absorption spectra may be attributed to an increase in the polarity of the fluorophore surrounding, thus the heme cavity in Ngb appears to be more polar compare to that of Mb and Cygb [(Leonard, Yonetani, and Callis)]. This is consistent with the distinct emission spectra measured for Ngb variants and Cygb variant as the longer wavelength emission peak in Ngb is blue shifter compare to Cygb and Mb. Considering a larger volume of the heme binding cavity in Ngb compare to Cygb, the Ngb distal cavity may be occupied by water molecule(s), resulting in the blue shift of the Soret band and the longer wavelength peak of the emission spectrum. Interestingly, Ngb C46G mutant and Ngb E52Q mutant leads to a 1-2 nm blue shift in the longer wavelength emission peak compare to NgbWT, suggesting that the heme pocket in Ngb is sensitive to the structural changes in the CD loop that are triggered by to the reduction of the disulfide bridge or substitution of negatively charged Glu residue by Gln.

Additional information about the heme pocket dynamics can be obtained by monitoring the fluorescence lifetime of ZnPPIX. Based on the biphasic fluorescent lifetimes and associated pre-exponential values, it is reasonable to assume there are two different orientations of the heme inside the distal cavity in both Cygb and Ngb. Indeed, heme disorder was observed in previous NMR and X-ray crystallography studies on human and murine Ngb as the heme group was found to rotate around the α - γ -meso axis [Xu, Yin, and Du; Du et al.; Pesce et al.]. The data reported here suggest that the orientation of the porphyrin group in the reconstituted Ngb variants is sensitive to the conformational changes in the CD loop of the protein, as the lifetime data for NgbC46Gmutnt and NgbH64Q mutant exhibit increase in τ_1 and τ_2 values with respect to the values observed for NgbWT. Interestingly, the pre-exponential factor associated with τ_2 in NgbH64Q mutant is less than 10%, suggesting that the distal histidine sidechain contributes to the observed bimodal lifetime in ZnPPIXNgb. This is further confirmed by lifetime data for NgbC46G mutant. Although two lifetimes were resolved in this construct, the pre-exponential factor associated with τ_2 is small, $\sim 5\%$, suggesting that removal of the intra-protein disulfide bridge promotes a single orientation of the heme group, possible through decreasing the conformational heterogeneity of the distal histidine. The lifetime data recorded for Cygb constructs indicate that the lifetime of ZnPPIX reconstituted in Cygb variants is less sensitive to the changes in the flurophore surrounding. Surprisingly, the lifetime parameters measured for CygbH81Q mutant are almost identical to lifetime data for CygbWT. The removal of the disulfide bridge leads

to a small increase in both τ_1 and τ_2 as well as the increase in the pre-exponential factor for τ_1 and similar increase in τ_1 was observed for CygbR84L mutant and truncated mutant. Interestingly, previous study reported that arginine 84 adopt two distinct orientations in the ligand free Cygb: a major conformation (~60%) with the side-chain positioned towards the solvent and a minor conformation (~40%) with the side-chain positioned towards the heme pocket, and this heterogeneity might be promoted by the reduction of the disulfide bridge (Astudillo et al., 2013). Also, the lifetime data for the ZnPPIX reconstituted truncated Cygb indicates that the extended terminals in Cygb can also impact the heme orientation in the heme binding cavity, however, the mechanism is not clear. The phosphorescence lifetimes are comparable in all ZnPPIX reconstituted globins suggesting that the triplet state lifetime is not sensitive to small changes in the fluorophore environment. It is also possible that the changes in the phosphorescent decay are small and thus may be difficult to resolved as the phosphorescence lifetime is strongly impacted by a possible presence of residual oxygen.

Quenching study can provide information on the accessibility and migration of the ligand to the heme pocket. The quenching of the steady-state fluorescence of ZnPPIX reconstituted globins by methyl viologen illustrate distinct distal pocket accessibility in Cygb and Ngb. The K_{sv} value reveals that Cygb variants are generally less accessible for quencher than Ngb variants. The replacement of distal histidine in Cygb further decreased the accessibility of the distal pocket while the removal of the internal disulfide bond does not impact the quencher access to ZnPPIX in Cygb. Compare to

Cygb, the distal cavity in Ngb is more open to the exogenous ligands, but the accessibility is diminished by the removal of the disulfide bridge and by substitution of distal histidine residue. Oxygen quenching of the triplet-state phosphorescence of ZnPPIX reconstituted globin provide the quenching rate constant for ZnPPIX reconstituted hhMb, CygbWT and NgbWT. Although there are small variations, the quenching rate constant determined for all three proteins are comparable and indicate that the diffusion of the oxygen molecule represent the rate limiting step for O₂ migration into the heme binding pocket.

5.4 Summary

In conclusion, by incorporating heme fluorescent analogs into the hexacoordinated globins, we were able to reveal distinct structural changes in hexa-coordinate globins Cygb and Ngb. The observed bimodal fluorescence lifetime as well as the splitting of the α -band in the absorption spectrum of Cygb variants indicate heterogeneity of the ZnPPIX orientation in the protein pocket and/or heterogeneity in the fluorophore surrounding. Indeed, the results obtained for constructs with replaced distal histidine residue in both proteins suggest that the orientation of the distal histidine may contribute to the conformational heterogeneity observed in hexa-coordinate globins. In addition, the distal histidine conformation may be modulated by the disulfide bond in Ngb and by Arg81 sidechain in Cygb protein. The environment of the ZnPPIX in Ngb and Cygb is distinct as evident from different absorption and emission spectra recorded for

ZnPPIX Ngb and ZnPPIX Cygb variants. This is further confirmed by an increased accessibility of ZnPPIX to MV^{2+} quencher in Ngb structure.

6 THE O₂ BINDING KINETIC AND IMPACT ON HEME CAVITY

STABILITY IN GLOBIN X.

6.1 Introduction

Globin X (GbX) is a new member of the globin superfamily that first discovered in fish and amphibians (Roesner et al., 2004). Similar to other novel members of the vertebrate globins such as neuroglobin (Ngb) and cytoglobin (Cygb), GbX exhibits a hexa-coordination that has a distal histidine bind the heme iron at six position (Blank, Wollberg, et al., 2011). The distal histidine in GbX can be displaced by the small diatomic ligands such as CO, NO, or O₂. As a hexa-coordinate globin, the distal histidine in the heme pocket will compete with the exogenous ligands which ultimately modulate the ligand affinity to the protein, for example, replacement of the distal histidine in Ngb result in a 5 to 10 fold increase in CO rebinding rate compare to WT and the replacement of the distal histidine in mouse Ngb increases the affinity of the protein for O₂ 10 fold. GbX display a high affinity to O₂ (P₅₀ ~1.3 torr) which is close to that observed for Mb (P₅₀ ~1 torr), Cygb (P₅₀ ~1 torr) and Ngb (P₅₀ ~1.9 torr), suggesting its potential role as a respiratory protein (Blank, Wollberg, et al., 2011).

In addition, GbX possess cysteine residues that are capable of forming intramolecular disulfide bridge which may influence the overall oxygen affinity. Indeed, Burmester's group has shown that in the presence of the reducing agent, DTT, GbX exhibits a fourfold decrease in the affinity for O₂ (Blank, Wollberg, et al., 2011).

Similar impact of the disruption of disulfide bridge on O₂ affinity was also observed in Ngb (~ nine-fold) but small impact of the disulfide bond on O₂ was observed in Cygb, ~two fold (Hamdane et al., 2003). Such large change in the O₂ affinity observed in Ngb was attributed to the movement of the E-helix triggered by the disruption of the disulfide bridge. The presence of intramolecular disulfide bridge is also important for other function properties of globins. For example, Cygb cannot bind lipids in the absence of the disulfide bond (Beckerson, Wilson, et al., 2015). However, the disruption of the disulfide bridge in Ngb does not impact the rate constant for CO escape from the protein matrix (Astudillo et al., 2010). Less is known about the impact of the intramolecular disulfide bridge on the structural properties of GbX as the crystal structure of GbX has not been resolved. The two cysteines in the GbX that are responsible for the disulfide bridge formation are the Cys65 and Cys141, The Cys residues are located apart compare to Ngb structure that has Cys residue that form a disulfide bridge located in the CD loop, Cys 46 and Cys 55. Therefore, the disruption of the internal disulfide bridge in the GbX may trigger larger structural changes and thus have more pronounced impact on functional properties of GbX. Here, we employed the time-resolved absorption spectroscopy and photoacoustic calorimetry together with site-directed mutagenesis to investigate the kinetic and energetics for O₂ binding to GbX and how the internal disulfide bridge can regulate the O₂ binding kinetics and thermodynamics. Since the biological and physiological function of the GbX is still not clear, our study can provide information on how GbX interacts with the biological

important molecule, O₂, in terms of the affinity, rate constants and activation and reaction thermodynamic parameters.

6.2 Result

6.2.1 Steady-state UV-vis spectra

The O₂ bound GbXWT and C65A mutant absorption spectra were recorded and are shown in figure 6.1 and summarized in table 6.1.

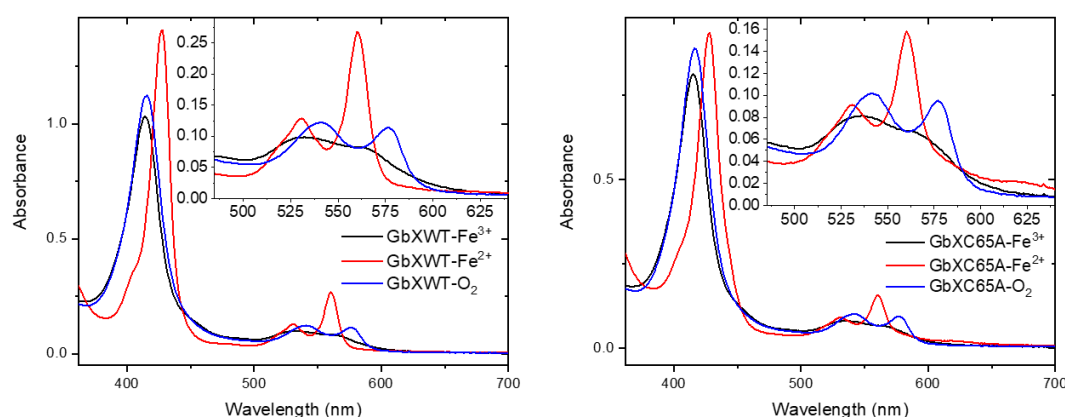


Figure 6.1. Absorption spectra of the oxidized (met), reduced (ferrous deoxy), and O₂ bound forms of GbX WT and C65A mutant. Measured in 50 mM TrisHCl pH 7.0.

The O₂ bound GbXWT shows a Soret at 416 nm and two additional Q-bands at 541 nm and 574 nm. The Soret band is shifted 6 nm and the β -bands shifted \sim 1 nm and

	Soret band (nm)	β -band (nm)	α -band (nm)
GbXWT-Fe ³⁺	414	532	563
GbXWT-Fe ²⁺	428	531	560
GbXWT-O ₂	416	541	576
GbXC65A-Fe ³⁺	415	536	564
GbXC65A-Fe ²⁺	428	531	560
GbXC65A-O ₂	416	541	577

Table 6.1. Absorption spectra wavelength of Soret and Q-band of GbX WT and C64A mutant summarized in the table.

α -band shifted 5 nm compare to CO bound GbXWT. Absorption spectrum of O₂ bound GbXC65A has the Soret band at 416 nm and Q-bands at 541 nm and 577 nm and it is

comparable to the absorption spectrum for GbXWT, suggesting that the heme electronic structure is similar in the oxygen bound protein with and without intra-protein disulfide bridge.

6.2.2 Stability of O₂ bound GbX towards pH unfolding

The stability of O₂ bound GbX variants was probed by recording absorbance of the Soret band as a function of pH. The overlay of the absorption spectra of O₂ bound GbXWT measured in the pH range from 8.0 to 0.4 is shown in figure 6.2, The absorption spectra show an isosbestic point at 393 nm, pointing towards a two-state heme release from the oxygen bound protein.

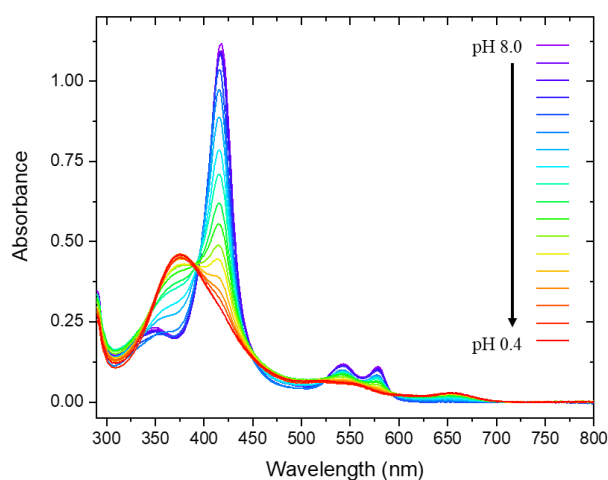


Figure 6.2. UV-vis absorption spectra of GBXWT in the oxygen bound form as function of pH. Measurements were performed in 5 mM phosphate-citrate buffer and 100 mM NaCl, under equilibrium conditions.

The absorption spectrum of GbXWT measured at pH 0.4 shows a broad Soret band with a maximum at 375 nm which is consistent with an destabilize polypeptide chain and a concomitant release of the prosthetic group from the protein matrix. Analogous changes in the absorption spectra were observed for pH unfolding of GbXC65A (data

not shown). The fraction of unfolded protein calculated based on the absorbance changes at 416 nm was plotted as a function of pH for both WT and C65A mutant (Figure 6.3). The experimental data were fitted using Eq. 3.41 and the fitting parameters are summarized in Table 6.2. The pH induced unfolding of O₂ bound GbXWT is

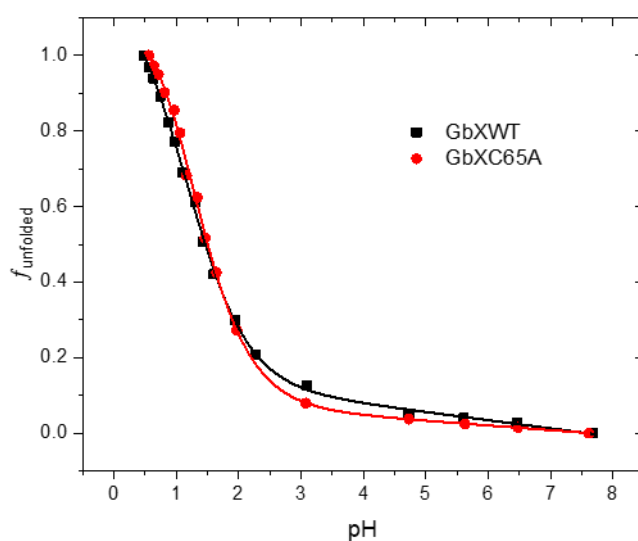


Figure 6.3. Fraction unfolding of oxygen bound GbX WT and C65A mutant plot as a function of pH.

characterized by a pH at half-transition (pH_{mid}) of 1.19, which is about 3.4 units lower than that previously reported for met horse heart Mb (pH_{mid} 4.6) and 2 units lower than that determined for met Ngb (pH_{mid} 3.2). Also, the pH induced unfolding of O₂ bound GbXWT is 0.7 unit lower than that obtained for the met GbXWT (pH_{mid} 1.9). In contrast, pH induced unfolding of O₂ bound GbXC65A shown a pH at half-transition (pH_{mid}) of 1.07 which is similar to the value determined for O₂ bound GbXWT.

	pH _{mid}	Δv_{H^+}
GbXWT	1.19	-0.90
GbXC65A	1.07	-0.97

Table 6.2. Parameters of the acid-induced oxygen bound GbX variants unfolding.

Interestingly, the pH_{mid} for pH induced unfolding of O₂ bound GbXC65A is 1.4 units lower than that for the met form of GbXC65A (pH_{mid} 2.48), suggesting a minor impact of the disulfide bridge on the stability of the protein in the oxygen bound form.

6.2.3 GbX O₂ binding kinetic

To further analyze interactions of GbX variants with O₂, O₂ binding kinetics were investigated using transient absorption spectroscopy. The transient absorption traces for O₂ binding to GbX constructs studied are shown in Figure 6.4A. Both traces were fitted

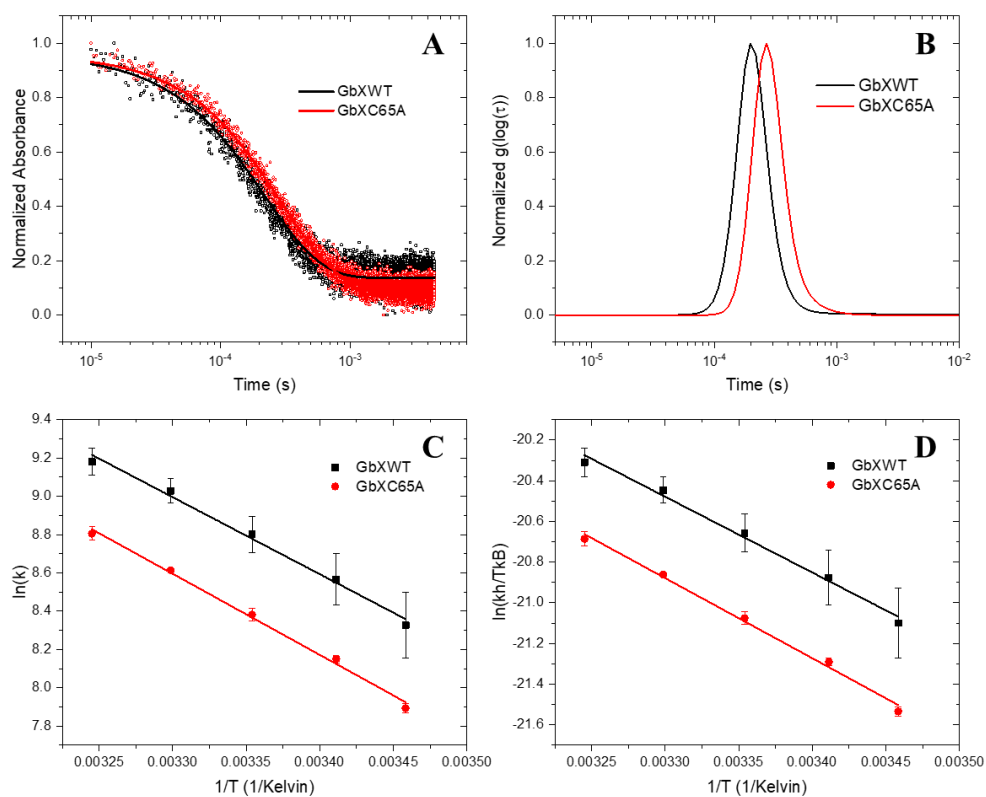


Figure 6.4. A, transient absorption traces for O₂ rebinding to GbX variants. B, Lifetime

distribution associated with the O₂ rebinding to GbX variant determined by MEM approach. C, Arrhenius plot of temperature dependent O₂ rebinding to GbX variants. D, Eyring plot of temperature dependent O₂ rebinding to GbX variants.

using a single exponential decay model and MEM (maximum entropy method) and the kinetic parameters are summarized in Table 6.3. A single kinetic was obtained for O₂ association to GbXWT with $k = 21.2 \pm 2.8 \mu\text{M}^{-1} \text{s}^{-1}$. Similar rate constant was obtained using MEM analysis ($k = 22.0 \pm 2.4 \mu\text{M}^{-1} \text{s}^{-1}$). The analysis of O₂ rebinding kinetic to GbXC65A mutant also reveals only 1 rate constant which is $13.9 \pm 0.3 \mu\text{M}^{-1} \text{s}^{-1}$ which is slower than the rate constant measured for O₂ binding to GbXWT. In addition to the individual rate constants, the activation energy, log pre-exponential factor, reaction enthalpy, and reaction entropy were determined by temperature dependent O₂ rebinding experiment (figure 6.4 C, D; Table 6.4).

	k ($\mu\text{M}^{-1} \text{s}^{-1}$)
GbXWT (decay)	21.2 ± 2.8
GbXWT (MEM)	22.0 ± 2.4
GbXC65A (decay)	13.9 ± 0.3
GbXC65A (MEM)	14.6 ± 0.3

Table 6.3. Rate constants for O₂ binding to GbX variants obtained using both exponential decay model and MEM analysis at 20°C.

The activation energy for O₂ binding to GbX is $7.9 \pm 1.5 \text{ kcal mol}^{-1}$ which is similar to horse heart Mb ($7.5 \text{ kcal mol}^{-1}$) and human Ngb (8 kcal mol^{-1}) as well as the hemoglobin from *Drosophila* ($10.5 \text{ kcal mol}^{-1}$) and *Arabidopsis* (8 kcal mol^{-1}), indicating a similar energy barrier for O₂ binding to heme iron in globins (Julien Uzan et al, 2004).

	E_a (kcal mol ⁻¹)	Log(A)	ΔH^\ddagger (kcal mol ⁻¹)	ΔS^\ddagger (cal mol ⁻¹ K ⁻¹)
GbXWT	7.9±1.5	9.6±1.1	7.3±1.5	-16.1±4.6
GbXC65A	8.4±0.1	9.8±0.1	7.8±0.1	-15.3±0.3

Table 6.4. Activation energy, log pre-exponential factor, activation enthalpy, and activation entropy of temperature dependent O₂ rebinding to GbX variants.

Also, activation enthalpy and entropy were obtained from the Eyring plot for O₂ binding to GbX. The linear fit provide ΔH^\ddagger to be 7.3 ± 1.5 kcal mol⁻¹ and ΔS^\ddagger equal to -16.1 ± 4.6 cal mol⁻¹ K⁻¹. In comparison, disulfide bridge mutant GbXC65A shown an activation energy (8.4 ± 0.1 kcal mol⁻¹), activation enthalpy ($\Delta H^\ddagger = 7.8 \pm 0.1$ kcal mol⁻¹) as well as activation entropy (-15.3 ± 0.3 cal mol⁻¹ K⁻¹) for O₂ binding which are comparable to GbXWT.

6.2.4 Photoacoustic calorimetry result of O₂ dissociation

The bimolecular quantum yielded for O₂ photo-release from GbXWT and C65A mutant is obtained by transient absorption spectroscopy and plot as a function of temperature shown in figure 6.5. The quantum yielded of GbXWTO₂ is ranging from 3.1% to 4.6% from 16 °C to 35 °C. On other hand, the bimolecular quantum yield for O₂ dissociation for GbXC65A is also temperature dependent and roughly two times higher than that observed for GbXWT.

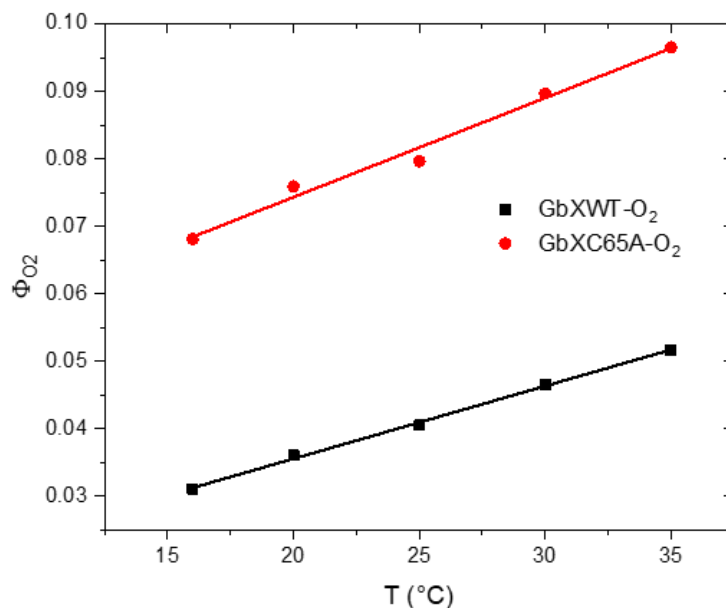


Figure 6.5 Quantum yield of O₂ from GbXWT and C65A plot as a function of temperature.

An overlay of the normalized photoacoustic traces for photo-dissociation of O₂ from GbXWT and GbXC65A together with the reference compound, 4SP, are shown in Figures 6.6. The photoacoustic traces are clearly shown that there is no phase shift between the sample and reference which indicated that the O₂ escaped from the protein matrix within 50 ns.

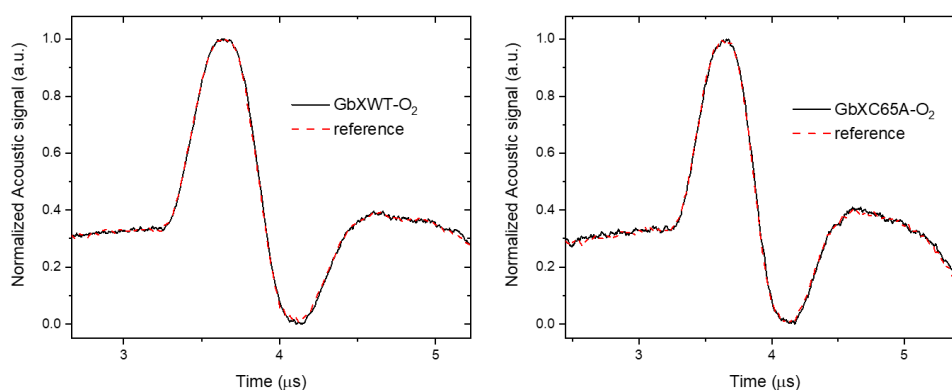


Figure 6.6 Photoacoustic traces for oxygen dissociation from GbXWT (left) and GbXC65A (right) together with the trace for the reference compound 4SP. Conditions: 20 μ M protein in 50 mM Tris buffer (pH 7.0). The absorbance of the reference compound is aligned with the absorbance of the sample at 532 nm.

Plots of the PAC amplitude ratios as a function of the thermal coefficient $[(C_{pp})/\beta]$ over the temperature range of 16 - 30 °C are displayed in Figure 6.7. The reaction enthalpy and volume changes were obtained from the intercept and slope of the linear plot, respectively, as described in the Materials and Methods section, and are listed in Table 6.5. From the reaction volume change, the structural volume change, ΔV_{str} , that describes the difference between the partial molar volume of the penta-coordinate GbX and O₂-bound GbX can be determined according to the equation 3.49.

$$\Delta V_{total} = \Delta V_{O_2}^\emptyset + V_{5c}^\emptyset GbX - V_{6c}^\emptyset GbXO_2 \quad (\text{Eq 3.49})$$

Where $V_{O_2}^\emptyset$ is the partial molar volume of O₂ (33.2 mL mol⁻¹), $V_{str} = V_{5c}^\emptyset GbX - V_{6c}^\emptyset GbXO_2$ (Moore et al., 1982).

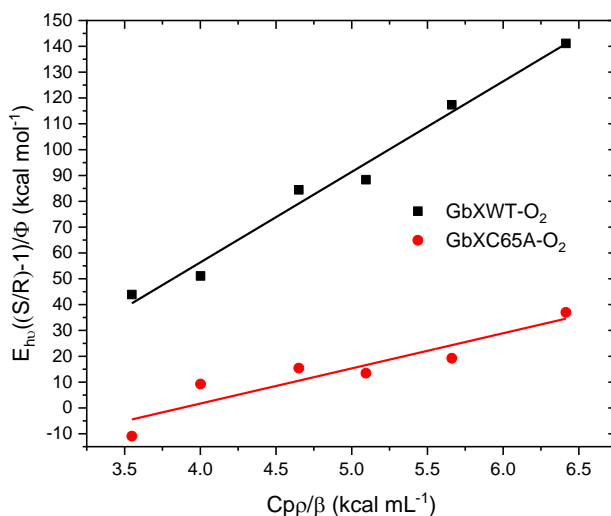


Figure 6.7. Plot of ϕE_{hv} as a function of C_{pp}/β for O₂ photo-release from GbXWT (black), and GbXC65A (red). The associated volume and enthalpy changes were obtained from the slope and intercept of the linear fits, respectively.

The photo-dissociation of O₂ from GbXWT is associated with a ΔV_{str} of 0.8 ± 12 mL mol⁻¹. However, the replacement of Cys65 with Ala has a significant impact on the structure volume change ($\Delta V_{str} = -18.2 \pm 2$ mL mol⁻¹) likely because of a larger

structural reorganization of the distal pocket in this mutant. The total enthalpy change for the photo-dissociation of O₂ from GbXWT is $79 \pm 30 \text{ kcal mol}^{-1}$, and GbXC65A is $60 \pm 3 \text{ kcal mol}^{-1}$.

	Temperature (°C)	ΔH_{total} (kcal mol ⁻¹)	ΔH_{str} (kcal mol ⁻¹)	ΔV_{total} (mL mol ⁻¹)	ΔV_{str} (mL mol ⁻¹)
GbXWT-O ₂	16-30	79±30	65±30	34±12	0.8±12
GbXC65A-O ₂	16-30	60±3	46±3	15±2	-18.2±2
*Mb-O ₂	6-15	11.6±8	-2.4±8	2.5±0.5	-30.7±0.5
*Ngb-O ₂	16-35	-23±4	-37±4	-9.0±0.7	-42.2

Table 6.5. Thermodynamic parameters associated with O₂ photo-dissociation from GbXWT and GbXC65A. *(Astudillo, 2014)

6.3 Discussion

Our data exhibit several interesting findings on the interaction between O₂ and GbX variants. The UV-vis absorption spectra of O₂ bound GbXC65A is comparable to the O₂ bound GbXWT indicate the electronic structure of the O₂ bound heme is not affected by the presence or disruption of the disulfide bridge. GbX shows an unusual stability towards unfolding as the release of the heme group from the protein matrix occurs at very acidic pH. The enhanced stability of the heme group can be attributed to the presence of the oxygen bond between the distal histidine and the oxygen bound to the heme iron. Interestingly, the stability of the protein in the oxygen bound form is not impacted by the disulfide bridge. Unlike CO, the O₂ binding to the heme iron can be modeled using a single exponential decay. This points towards distinct ligand binding mechanisms for O₂ and CO in this protein. We speculate that several migration pathways are sampled during the CO binding whereas O₂ may sample only a single

migration pathway. However, we cannot exclude that the observed single binding kinetic for O₂ association to the heme iron is due to the low amplitude of the absorption signal due to the small quantum yield for the bimolecular O₂ rebinding. In addition, the activation energy of O₂ binds to GbX variants is comparable to the activation energy for O₂ binding to other globins, demonstrating a similar mechanism for O₂ binding to heme in the globins. However, the activation entropy for O₂ binding to GbX is -16 cal mol⁻¹ K⁻¹. This value is distinct from the activation entropy values determined for O₂ binding to other globins such as human Ngb (2.8 cal mol⁻¹ K⁻¹) or horse heart Mb (-0.9 cal mol⁻¹ K⁻¹) (Uzan et al., 2004). Interestingly, the O₂ rebinding rate determined by transient absorption spectroscopy demonstrate a slower rate constant for O₂ binding to GbXC65A (13.9 ± 0.3 μM⁻¹ s⁻¹) compared to GbXWT (21.2 ± 2.8 μM⁻¹ s⁻¹). Both rate constants are faster than the O₂ rebinding to human Ngb, *Drosophila* Hb and *Arabidopsis* Hb, suggesting a high reactivity of GbX for oxygen molecule (Uzan et al., 2004). Photoacoustic calorimetry data show that the photo-dissociation of O₂ from GbXWT leads to a small positive structure volume change (0.8 ± 12 mL mol⁻¹) but a negative structure volume change (-18.2 ± 2 mL mol⁻¹) was measured for ligand dissociation from GbXC65A. These results indicate that although the enthalpy change for O₂ dissociation is not affected by the presence of the internal disulfide bridge, the volume changes are modulated by the presence of the disulfide bridge. The more negative structural volume change is also observed in Cygb and Ngb when the internal disulfide bridge was reduced (Astudillo, 2014). This clearly indicate that the presence

of the internal disulfide bridge modulates overall structural changes associated with the transition from six-coordinate O₂ bound GbX to five-coordinate deoxyGbX by ~19 mL mol⁻¹. In addition, the total enthalpy changes in O₂ dissociation from GbXC65A ($\Delta H = 60 \pm 3$ kcal mol⁻¹) is similar to ligand dissociation from GbXWT ($\Delta H = 79 \pm 30$ kcal mol⁻¹).

SUMMARY

The results presented here clearly indicate a distinct mechanism of hexa-coordinate globin interactions with diatomic ligands. Specifically, we show that globin X has very low affinity for CN⁻ in the met form and for CO in the deoxy form. The low affinity for CO is achieved by facilitating CO escape from the protein matrix. Interestingly, the affinity for the oxygen is significantly enhanced in GbX compare to other vertebrate globins such as Ngb and Cygb. Also, this protein exhibits an unusual stability towards pH unfolding as the heme group remains attached to the apoprotein at acidic pH. These results indicate that GbX may have physiological function(s) that is distinct from other hexa-coordinate vertebrate globins, such as Ngb and Cygb. Interestingly, the high affinity for O₂ and low affinity for CO and CN⁻ ligands are similar to hexa-coordinate globins found in plants, suggesting that GbX may represent a link between plant and vertebrate globins. Also, fluorescent studies of ZnPPIX reconstituted Ngb and Cygb revealed distinct properties of the heme binding pocket in Ngb and Cygb, although both proteins exhibit an increased heterogeneity of the heme binding pocket that may be characteristic feature of the hexa-coordinate globins.

LIST OF REFERENCES

- Abbruzzetti, S., Viappiani, C., Murgida, D. H., Erra-Balsells, R., & Bilmes, G. M. (1999). Non-toxic, water-soluble photocalorimetric reference compounds for UV and visible excitation. *Chemical Physics Letters*, 304(3–4), 167–172. [https://doi.org/10.1016/s0009-2614\(99\)00306-1](https://doi.org/10.1016/s0009-2614(99)00306-1)
- ALBANI, J., & ALPERT, B. (1987). Fluctuation domains in myoglobin. Fluorescence quenching studies. *European Journal of Biochemistry*, 162(1), 175–178. <https://doi.org/10.1111/j.1432-1033.1987.tb10558.x>
- Anderson, J. L. R., & Chapman, S. K. (2005). Ligand probes for heme proteins. *Dalton Transactions*, 0(1), 13. <https://doi.org/10.1039/b413046d>
- Aono, S., Ohtaka, A., & Okura, I. (1995). The effect of chemical modification of zinc myoglobin on the photoinduced electron transfer with methyl viologen. *Journal of Molecular Catalysis A: Chemical*, 96(1), 87–92. [https://doi.org/10.1016/1381-1169\(94\)00032-8](https://doi.org/10.1016/1381-1169(94)00032-8)
- Arcovito, A., Moschetti, T., D'Angelo, P., Mancini, G., Vallone, B., Brunori, M., & Longa, S. D. (2008). An X-ray diffraction and X-ray absorption spectroscopy joint study of neuroglobin. *Archives of Biochemistry and Biophysics*, 475(1), 7–13. <https://doi.org/10.1016/j.abb.2008.03.026>
- Asahina, K., Kawada, N., Kristensen, D. B., Nakatani, K., Seki, S., Shiokawa, M., Tateno, C., Obara, M., & Yoshizato, K. (2002). Characterization of human stellate cell activation-associated protein and its expression in human liver. *Biochimica et Biophysica Acta (BBA) - Gene Structure and Expression*, 1577(3), 471–475. [https://doi.org/10.1016/s0167-4781\(02\)00477-3](https://doi.org/10.1016/s0167-4781(02)00477-3)
- Astudillo, L. (2014). *Conformational Dynamics Associated with Ligand Binding to Vertebrate Hexa-coordinate Hemoglobins*. <https://doi.org/10.25148/etd.fi14040865>

Astudillo, L., Bernad, S., Derrien, V., Sebban, P., & Miksovská, J. (2010). Probing the role of the internal disulfide bond in regulating conformational dynamics in neuroglobin. *Biophysical Journal*, 99(2), L16-8. <https://doi.org/10.1016/j.bpj.2010.04.033>

Astudillo, L., Bernad, S., Derrien, V., Sebban, P., & Miksovská, J. (2012). Conformational dynamics in human neuroglobin: effect of His64, Val68, and Cys120 on ligand migration. *Biochemistry*, 51(50), 9984–9994. <https://doi.org/10.1021/bi301016u>

Astudillo, L., Bernad, S., Derrien, V., Sebban, P., & Miksovská, J. (2013). Reduction of the internal disulfide bond between Cys 38 and 83 switches the ligand migration pathway in cytoglobin. *Journal of Inorganic Biochemistry*, 129, 23–29. <https://doi.org/10.1016/j.jinorgbio.2013.08.006>

Atkins, P., & Paula, J. de. (2010). *Atkins' Physical Chemistry*. OUP Oxford. <https://books.google.com/books?id=BV6cAQAAQBAJ>

Barboy, N., & Feitelson, J. (1987). Quenching of the zinc-protoporphyrin triplet state as a measure of small-molecule diffusion through the structure of myoglobin. *Biochemistry*, 26(11), 3240–3244. <https://doi.org/10.1021/bi00385a046>

Beckerson, P., Svistunenko, D., & Reeder, B. (2015). Effect of the distal histidine on the peroxidatic activity of monomeric cytoglobin. *F1000Research*, 4, 87. <https://doi.org/10.12688/f1000research.5971.1>

Beckerson, P., Wilson, M. T., Svistunenko, D. A., & Reeder, B. J. (2015). Cytoglobin ligand binding regulated by changing haem-co-ordination in response to intramolecular disulfide bond formation and lipid interaction. *The Biochemical Journal*, 465(1), 127–137. <https://doi.org/10.1042/bj20140827>

Belogortseva, N., Rubio, M., Terrell, W., & Mikšovská, J. (2007). The contribution of heme propionate groups to the conformational dynamics associated with CO

photodissociation from horse heart myoglobin. *Journal of Inorganic Biochemistry*, 101(7), 977–986. <https://doi.org/10.1016/j.jinorgbio.2007.03.009>

Bholah, T. C., Neergheen-Bhujun, V. S., Hodges, N. J., Dyllal, S. D., & Bahorun, T. (2015). Cytoglobin as a Biomarker in Cancer: Potential Perspective for Diagnosis and Management. *BioMed Research International*, 2015, 824514. <https://doi.org/10.1155/2015/824514>

Birukou, I., Schweers, R. L., & Olson, J. S. (2010). Distal histidine stabilizes bound O₂ and acts as a gate for ligand entry in both subunits of adult human hemoglobin. *The Journal of Biological Chemistry*, 285(12), 8840–8854. <https://doi.org/10.1074/jbc.m109.053934>

Blank, M., & Burmester, T. (2012). Widespread occurrence of N-terminal acylation in animal globins and possible origin of respiratory globins from a membrane-bound ancestor. *Molecular Biology and Evolution*, 29(11), 3553–3561. <https://doi.org/10.1093/molbev/mss164>

Blank, M., Kiger, L., Thielebein, A., Gerlach, F., Hankeln, T., Marden, M. C., & Burmester, T. (2011). Oxygen supply from the bird's eye perspective: globin E is a respiratory protein in the chicken retina. *The Journal of Biological Chemistry*, 286(30), 26507–26515. <https://doi.org/10.1074/jbc.m111.224634>

Blank, M., Wollberg, J., Gerlach, F., Reimann, K., Roesner, A., Hankeln, T., Fago, A., Weber, R. E., & Burmester, T. (2011). A membrane-bound vertebrate globin. *PLoS One*, 6(9), e25292. <https://doi.org/10.1371/journal.pone.0025292>

Bocahut, A., Derrien, V., Bernad, S., Sebban, P., Sacquin-Mora, S., Guittet, E., & Lescop, E. (2012). Heme orientation modulates histidine dissociation and ligand binding kinetics in the hexacoordinated human neuroglobin. *Journal of Biological Inorganic Chemistry: JBIC: A Publication of the Society of Biological Inorganic Chemistry*, 18(1), 111–122. <https://doi.org/10.1007/s00775-012-0956-2>

Burmester, T., & Hankeln, T. (2009). What is the function of neuroglobin? *Journal of Experimental Biology*, 212(10), 1423–1428. <https://doi.org/10.1242/jeb.000729>

Burmester, T., & Hankeln, T. (2014). Function and evolution of vertebrate globins. *Acta Physiologica*, 211(3), 501–514. <https://doi.org/10.1111/apha.12312>

Burmester, Thorsten, Ebner, B., Weich, B., & Hankeln, T. (2002). Cytoglobin: A Novel Globin Type Ubiquitously Expressed in Vertebrate Tissues. *Molecular Biology and Evolution*, 19(4), 416–421. <https://doi.org/10.1093/oxfordjournals.molbev.a004096>

Burmester, Thorsten, Weich, B., Reinhardt, S., & Hankeln, T. (2000). A vertebrate globin expressed in the brain. *Nature*, 407(6803), 520–523. <https://doi.org/10.1038/35035093>

Butcher, D., Bernad, S., Derrien, V., Sebban, P., & Miksovska, J. (2017). Role of Ionic Strength and pH in Modulating Thermodynamic Profiles Associated with CO Escape from Rice Nonsymbiotic Hemoglobin 1. *The Journal of Physical Chemistry. B*, 121(2), 351–364. <https://doi.org/10.1021/acs.jpccb.6b06933>

Chandra, R., Tiwari, M., Kaur, P., Sharma, M., Jain, R., & Dass, S. (2000). Metalloporphyrins-Applications and clinical significance. *Indian Journal of Clinical Biochemistry : IJCB*, 15(Suppl 1), 183–199. <https://doi.org/10.1007/bf02867558>

Corti, P., Xue, J., Tejero, J., Wajih, N., Sun, M., Stolz, D. B., Tsang, M., Kim-Shapiro, D. B., & Gladwin, M. T. (2016). Globin X is a six-coordinate globin that reduces nitrite to nitric oxide in fish red blood cells. *Proceedings of the National Academy of Sciences of the United States of America*, 113(30), 8538–8543. <https://doi.org/10.1073/pnas.1522670113>

Dewilde, S., Kiger, L., Burmester, T., Hankeln, T., Baudin-Creuzat, V., Aerts, T., Marden, M. C., Caubergs, R., & Moens, L. (2001). Biochemical Characterization and Ligand Binding Properties of Neuroglobin, a Novel Member of the Globin Family. *Journal of Biological Chemistry*, 276(42), 38949–38955. <https://doi.org/10.1074/jbc.m106438200>

- Dou, Y., Olson, J. S., Wilkinson, A. J., & Ikeda-Saito, M. (1996). Mechanism of Hydrogen Cyanide Binding to Myoglobin†. *Biochemistry*, 35(22), 7107–7113. <https://doi.org/10.1021/bi9600299>
- Drew, E. D., Mavridis, L., & Janes, R. W. (2018). PDB2CD: A Web-Based Application for the Generation of Circular Dichroism Spectra from Protein Atomic Coordinates. *Biophysical Journal*, 114(3), 46a. <https://doi.org/10.1016/j.bpj.2017.11.302>
- Dröge, J., & Makałowski, W. (2011). Phylogenetic analysis reveals wide distribution of globin X. *Biology Direct*, 6(1), 54. <https://doi.org/10.1186/1745-6150-6-54>
- Du, W., Syvitski, R., Dewilde, S., Moens, L., & Mar, G. N. L. (2003). Solution 1h NMR characterization of equilibrium heme orientational disorder with functional consequences in mouse neuroglobin. *Journal of the American Chemical Society*, 125(27), 8080–8081. <https://doi.org/10.1021/ja034584r>
- Exertier, C., Milazzo, L., Freda, I., Montemiglio, L. C., Scaglione, A., Cerutti, G., Parisi, G., Anselmi, M., Smulevich, G., Savino, C., & Vallone, B. (2019). Proximal and distal control for ligand binding in neuroglobin: role of the CD loop and evidence for His64 gating. *Scientific Reports*, 9(1), 5326. <https://doi.org/10.1038/s41598-019-41780-3>
- Fago, A., Mathews, A. J., Moens, L., Dewilde, S., & Brittain, T. (2006). The reaction of neuroglobin with potential redox protein partners cytochrome b 5 and cytochrome c. *FEBS Letters*, 580(20), 4884–4888. <https://doi.org/10.1016/j.febslet.2006.08.003>
- Fanelli, A. R., Antonini, E., & Caputo, A. (1958). Studies on the structure of hemoglobin I. Physicochemical properties of human globin. *Biochimica et Biophysica Acta*, 30(3), 608–615. [https://doi.org/10.1016/0006-3002\(58\)90108-2](https://doi.org/10.1016/0006-3002(58)90108-2)
- Flonta, S. E., Arena, S., Pisacane, A., Michieli, P., & Bardelli, A. (2009). Expression and functional regulation of myoglobin in epithelial cancers. *The American Journal of Pathology*, 175(1), 201–206. <https://doi.org/10.2353/ajpath.2009.081124>

Fuchs, C., Burmester, T., & Hankeln, T. (2006). The amphibian globin gene repertoire as revealed by the *Xenopus* genome. *Cytogenetic and Genome Research*, *112*(3–4), 296–306. <https://doi.org/10.1159/000089884>

Garry, D. J., Ordway, G. A., Lorenz, J. N., Radford, N. B., Chin, E. R., Grange, R. W., Bassel-Duby, R., & Williams, R. S. (1998). Mice without myoglobin. *Nature*, *395*(6705), 905–908. <https://doi.org/10.1038/27681>

Gensch, T., & Viappiani, C. (2003). Time-resolved photothermal methods: accessing time-resolved thermodynamics of photoinduced processes in chemistry and biology Dedicated to Professor Silvia Braslavsky, to mark her great contribution to photochemistry and photobiology particularly in the field of photothermal methods. *Photochemical & Photobiological Sciences*, *2*(7), 699. <https://doi.org/10.1039/b303177b>

Gibson, Q. H. (1956). An apparatus for flash photolysis and its application to the reactions of myoglobin with gases. *The Journal of Physiology*, *134*(1), 112–122. <https://doi.org/10.1113/jphysiol.1956.sp005627>

Gorr, T. A., Wichmann, D., Pilarsky, C., Theurillat, J.-P., Fabrizius, A., Laufs, T., Bauer, T., Koslowski, M., Horn, S., Burmester, T., Hankeln, T., & Kristiansen, G. (2010). Old proteins - new locations: myoglobin, haemoglobin, neuroglobin and cytoglobin in solid tumours and cancer cells. *Acta Physiologica (Oxford, England)*, *202*(3), 563–581. <https://doi.org/10.1111/j.1748-1716.2010.02205.x>

Guo, X., Philipsen, S., & Tan-Un, K.-C. (2007). Study of the hypoxia-dependent regulation of human CYGB gene. *Biochemical and Biophysical Research Communications*, *364*(1), 145–150. <https://doi.org/10.1016/j.bbrc.2007.09.108>

Hamdane, D., Kiger, L., Dewilde, S., Green, B. N., Pesce, A., Uzan, J., Burmester, T., Hankeln, T., Bolognesi, M., Moens, L., & Marden, M. C. (2003). The Redox State of the Cell Regulates the Ligand Binding Affinity of Human Neuroglobin and Cytoglobin. *Journal of Biological Chemistry*, *278*(51), 51713–51721. <https://doi.org/10.1074/jbc.m309396200>

Hamdane, D., Kiger, L., Dewilde, S., Uzan, J., Burmester, T., Hankeln, T., Moens, L., & Marden, M. C. (2005). Hyperthermal stability of neuroglobin and cytoglobin: Thermal stability of neuroglobin. *FEBS Journal*, 272(8), 2076–2084. <https://doi.org/10.1111/j.1742-4658.2005.04635.x>

Hanai, S., Tsujino, H., Yamashita, T., Torii, R., Sawai, H., Shiro, Y., Oohora, K., Hayashi, T., & Uno, T. (2017). Roles of N- and C-terminal domains in the ligand-binding properties of cytoglobin. *Journal of Inorganic Biochemistry*, 179, 1–9. <https://doi.org/10.1016/j.jinorgbio.2017.11.003>

HARRISON, S. C., & BLOUT, E. R. (1965). REVERSIBLE CONFORMATIONAL CHANGES OF MYOGLOBIN AND APOMYOGLOBIN. *The Journal of Biological Chemistry*, 240, 299–303.

Hartridge, H., & Roughton, F. J. W. (1923). The Kinetics of Hæmoglobin. II. The Velocity with Which Oxygen Dissociates from Its Combination with Hæmoglobin. *JSTOR*, 104(726), 395–430. www.jstor.org/stable/94180

Hayashi, T., Matsuo, T., Hitomi, Y., Okawa, K., Suzuki, A., Shiro, Y., Iizuka, T., Hisaeda, Y., & Ogoshi, H. (2002). Contribution of heme-propionate side chains to structure and function of myoglobin: chemical approach by artificially created prosthetic groups. *Journal of Inorganic Biochemistry*, 91(1), 94–100. [https://doi.org/10.1016/s0162-0134\(02\)00423-3](https://doi.org/10.1016/s0162-0134(02)00423-3)

Hendgen-Cotta, U. B., Merx, M. W., Shiva, S., Schmitz, J., Becher, S., Klare, J. P., Steinhoff, H.-J., Goedecke, A., Schrader, J., Gladwin, M. T., Kelm, M., & Rassaf, T. (2008). Nitrite reductase activity of myoglobin regulates respiration and cellular viability in myocardial ischemia-reperfusion injury. *Proceedings of the National Academy of Sciences of the United States of America*, 105(29), 10256–10261. <https://doi.org/10.1073/pnas.0801336105>

Holde, K. E. V., Johnson, W. C., & Ho, P. S. (1998). *Principles of Physical Biochemistry*. Prentice Hall. <https://books.google.com/books?id=TrPwAAAAMAAJ>

Hoogewijs, D., Ebner, B., Germani, F., Hoffmann, F. G., Fabrizius, A., Moens, L., Burmester, T., Dewilde, S., Storz, J. F., Vinogradov, S. N., & Hankeln, T. (2011). Androglobin: a chimeric globin in metazoans that is preferentially expressed in Mammalian testes. *Molecular Biology and Evolution*, 29(4), 1105–1114. <https://doi.org/10.1093/molbev/msr246>

Hou, S., Larsen, R. W., Boudko, D., Riley, C. W., Karatan, E., Zimmer, M., Ordal, G. W., & Alam, M. (2000). Myoglobin-like aerotaxis transducers in Archaea and Bacteria. *Nature*, 403(6769), 540–544. <https://doi.org/10.1038/35000570>

Kakar, S., Hoffman, F. G., Storz, J. F., Fabian, M., & Hargrove, M. S. (2010). Structure and reactivity of hexacoordinate hemoglobins. *Biophysical Chemistry*, 152(1–3), 1–14. <https://doi.org/10.1016/j.bpc.2010.08.008>

Karp, D. A., Gittis, A. G., Stahley, M. R., Fitch, C. A., Stites, W. E., & E, B. G.-M. (2007). High Apparent Dielectric Constant Inside a Protein Reflects Structural Reorganization Coupled to the Ionization of an Internal Asp. *Biophysical Journal*, 92(6), 2041–2053. <https://doi.org/10.1529/biophysj.106.090266>

Kelly, S. M., Jess, T. J., & Price, N. C. (2005). How to study proteins by circular dichroism. *Biochimica et Biophysica Acta (BBA) - Proteins and Proteomics*, 1751(2), 119–139. <https://doi.org/10.1016/j.bbapap.2005.06.005>

Khan, A. A., Wang, Y., Sun, Y., Mao, X. O., Xie, L., Miles, E., Graboski, J., Chen, S., Ellerby, L. M., Jin, K., & Greenberg, D. A. (2006). Neuroglobin-overexpressing transgenic mice are resistant to cerebral and myocardial ischemia. *Proceedings of the National Academy of Sciences*, 103(47), 17944–17948. <https://doi.org/10.1073/pnas.0607497103>

Klostermeier, D., & Rudolph, M. G. (2018). *Biophysical Chemistry*. CRC Press. <https://books.google.com/books?id=ZchwDwAAQBAJ>

Koch, J., & Burmester, T. (2016). Membrane-bound globin X protects the cell from reactive oxygen species. *Biochemical and Biophysical Research Communications*, 469(2), 275–280. <https://doi.org/10.1016/j.bbrc.2015.11.105>

Lakowicz, J. R. (2007). *Principles of Fluorescence Spectroscopy*. Springer US. <https://books.google.com/books?id=-PSybuLNxcAC>

Lakowicz, J. R., Laczko, G., Cherek, H., Gratton, E., & Limkeman, M. (1984). Analysis of fluorescence decay kinetics from variable-frequency phase shift and modulation data. *Biophysical Journal*, 46(4), 463–477. [https://doi.org/10.1016/s0006-3495\(84\)84043-6](https://doi.org/10.1016/s0006-3495(84)84043-6)

Larsen, R. W., & Mikšovská, J. (2007). Time resolved thermodynamics of ligand binding to heme proteins. *Coordination Chemistry Reviews*, 251(9–10), 1101–1127. <https://doi.org/10.1016/j.ccr.2006.08.018>

Laufs, T. L., Wystub, S., Reuss, S., Burmester, T., Saaler-Reinhardt, S., & Hankeln, T. (2004). Neuron-specific expression of neuroglobin in mammals. *Neuroscience Letters*, 362(2), 83–86. <https://doi.org/10.1016/j.neulet.2004.02.072>

Lechauve, C., Rezaei, H., Celier, C., Kiger, L., Corral-Debrinski, M., Noinville, S., Chauvierre, C., Hamdane, D., Pato, C., & Marden, M. C. (2009). Neuroglobin and prion cellular localization: investigation of a potential interaction. *Journal of Molecular Biology*, 388(5), 968–977. <https://doi.org/10.1016/j.jmb.2009.03.047>

Li, H., Hemann, C., Abdelghany, T. M., El-Mahdy, M. A., & Zweier, J. L. (2012). Characterization of the mechanism and magnitude of cytoglobin-mediated nitrite reduction and nitric oxide generation under anaerobic conditions. *The Journal of Biological Chemistry*, 287(43), 36623–36633. <https://doi.org/10.1074/jbc.m112.342378>

Liang, Z.-X., Nocek, J. M., Huang, K., Hayes, R. T., Kurnikov, I. V., Beratan, D. N., & Hoffman, B. M. (2002). Dynamic Docking and Electron Transfer between Zn-

myoglobin and Cytochrome b 5. *Journal of the American Chemical Society*, 124(24), 6849–6859. <https://doi.org/10.1021/ja0127032>

Liu, H.-X., Li, L., Yang, X.-Z., Wei, C.-W., Cheng, H.-M., Gao, S.-Q., Wen, G.-B., & Lin, Y.-W. (2019). Enhancement of protein stability by an additional disulfide bond designed in human neuroglobin. *RSC Advances*, 9(8), 4172–4179. <https://doi.org/10.1039/c8ra10390a>

Liu, J., Yu, Z., Guo, S., Lee, S.-R., Xing, C., Zhang, C., Gao, Y., Nicholls, D. G., Lo, E. H., & Wang, X. (2009). Effects of neuroglobin overexpression on mitochondrial function and oxidative stress following hypoxia/reoxygenation in cultured neurons. *Journal of Neuroscience Research*, 87(1), 164–170. <https://doi.org/10.1002/jnr.21826>

Liu, X., El-Mahdy, M. A., Boslett, J., Varadharaj, S., Hemann, C., Abdelghany, T. M., Ismail, R. S., Little, S. C., Zhou, D., Thuy, L. T. T., Kawada, N., & Zweier, J. L. (2017). Cytoglobin regulates blood pressure and vascular tone through nitric oxide metabolism in the vascular wall. *Nature Communications*, 8(1), 14807. <https://doi.org/10.1038/ncomms14807>

Livesey, A. K., & Brochon, J. C. (1987). Analyzing the Distribution of Decay Constants in Pulse-Fluorimetry Using the Maximum Entropy Method. *Biophysical Journal*, 52(5), 693–706. [https://doi.org/10.1016/s0006-3495\(87\)83264-2](https://doi.org/10.1016/s0006-3495(87)83264-2)

Mach, H., Middaugh, C. R., & Lewis, R. V. (1992). Statistical determination of the average values of the extinction coefficients of tryptophan and tyrosine in native proteins. *Analytical Biochemistry*, 200(1), 74–80. [https://doi.org/10.1016/0003-2697\(92\)90279-g](https://doi.org/10.1016/0003-2697(92)90279-g)

Makino, M., Sawai, H., Shiro, Y., & Sugimoto, H. (2011). Crystal structure of the carbon monoxide complex of human cytoglobin. *Proteins*, 79(4), 1143–1153. <https://doi.org/10.1002/prot.22950>

Makino, M., Sugimoto, H., Sawai, H., Kawada, N., Yoshizato, K., & Shiro, Y. (2006). High-resolution structure of human cytoglobin: identification of extra N- and C-termini

and a new dimerization mode. *Acta Crystallographica Section D Biological Crystallography*, 62(6), 671–677. <https://doi.org/10.1107/s0907444906013813>

Mathai, C., Jourdeuil, F. L., Lopez-Soler, R. I., & Jourdeuil, D. (2020). Emerging perspectives on cytoglobin, beyond NO dioxygenase and peroxidase. *Redox Biology*, 32, 101468. <https://doi.org/10.1016/j.redox.2020.101468>

McRonal, F. E., Liloglou, T., Xinarianos, G., Hill, L., Rowbottom, L., Langan, J. E., Ellis, A., Shaw, J. M., Field, J. K., & Risk, J. M. (2006). Down-regulation of the cytoglobin gene, located on 17q25, in tylosis with oesophageal cancer (TOC): evidence for trans-allele repression. *Human Molecular Genetics*, 15(8), 1271–1277. <https://doi.org/10.1093/hmg/ddl042>

Mikšovská, J., Day, J. H., & Larsen, R. W. (2003). Volume and enthalpy profiles of CO rebinding to horse heart myoglobin. *JBIC Journal of Biological Inorganic Chemistry*, 8(6), 621–625. <https://doi.org/10.1007/s00775-003-0457-4>

Mikšovská, J., Horsa, S., Davis, M. F., & Franzen, S. (2008). Conformational Dynamics Associated with Photodissociation of CO from Dehaloperoxidase Studied Using Photoacoustic Calorimetry †. *Biochemistry*, 47(44), 11510–11517. <https://doi.org/10.1021/bi8012033>

Moore, J. C., Battino, R., Rettich, T. R., Handa, Y. P., & Wilhelm, E. (1982). Partial molar volumes of gases at infinite dilution in water at 298.15 K. *Journal of Chemical & Engineering Data*, 27(1), 22–24. <https://doi.org/10.1021/je00027a005>

Naito, N. R., Huang, H., Sturgess, A. W., Nocek, J. M., & Hoffman, B. M. (1998). Binding and Electron Transfer between Cytochrome b 5 and the Hemoglobin α - and β -Subunits through the Use of [Zn, Fe] Hybrids. *Journal of the American Chemical Society*, 120(44), 11256–11262. <https://doi.org/10.1021/ja982009v>

Nakatani, K., Okuyama, H., Shimahara, Y., Saeki, S., Kim, D.-H., Nakajima, Y., Seki, S., Kawada, N., & Yoshizato, K. (2003). Cytoglobin/STAP, its unique localization in

splanchnic fibroblast-like cells and function in organ fibrogenesis. *Laboratory Investigation*, 84(1), 91–101. <https://doi.org/10.1038/labinvest.3700013>

Nienhaus, G. U. (2010). *Protein-Ligand Interactions: Methods and Applications*. Humana Press. <https://books.google.com/books?id=2RatcQAACAAJ>

Oleksiewicz, U., Liloglou, T., Field, J. K., & Xinarianos, G. (2011). Cytoglobin: biochemical, functional and clinical perspective of the newest member of the globin family. *Cellular and Molecular Life Sciences: CMLS*, 68(23), 3869–3883. <https://doi.org/10.1007/s00018-011-0764-9>

Olson, J. S., Mathews, A. J., Rohlfs, R. J., Springer, B. A., Egeberg, K. D., Sligar, S. G., Tame, J., Renaud, J.-P., & Nagai, K. (1988). The role of the distal histidine in myoglobin and haemoglobin. *Nature*, 336(6196), 265–266. <https://doi.org/10.1038/336265a0>

Peters, K. S., Watson, T., & Logan, T. (1992). Photoacoustic calorimetry study of human carboxyhemoglobin. *Journal of the American Chemical Society*, 114(11), 4276–4278. <https://doi.org/10.1021/ja00037a035>

Picotti, P., Dewilde, S., Fago, A., Hundahl, C., Filippis, V. D., Moens, L., & Fontana, A. (2009). Unusual stability of human neuroglobin at low pH - molecular mechanisms and biological significance: Unusual acid stability of human neuroglobin. *FEBS Journal*, 276(23), 7027–7039. <https://doi.org/10.1111/j.1742-4658.2009.07416.x>

Poulos, T. L. (2014). Heme enzyme structure and function. *Chemical Reviews*, 114(7), 3919–3962. <https://doi.org/10.1021/cr400415k>

Reuss, S., Saaler-Reinhardt, S., Weich, B., Wystub, S., Reuss, M. H., Burmester, T., & Hankeln, T. (2002). Expression analysis of neuroglobin mRNA in rodent tissues. *Neuroscience*, 115(3), 645–656. [https://doi.org/10.1016/s0306-4522\(02\)00536-5](https://doi.org/10.1016/s0306-4522(02)00536-5)

Roesner, A., Fuchs, C., Hankeln, T., & Burmester, T. (2004). A Globin Gene of Ancient Evolutionary Origin in Lower Vertebrates: Evidence for Two Distinct Globin Families in Animals. *Molecular Biology and Evolution*, 22(1), 12–20. <https://doi.org/10.1093/molbev/msh258>

Rohlf, R. J., Mathews, A. J., Carver, T. E., Olson, J. S., Springer, B. A., Egeberg, K. D., & Sligar, S. G. (1990). The effects of amino acid substitution at position E7 (residue 64) on the kinetics of ligand binding to sperm whale myoglobin. *The Journal of Biological Chemistry*, 265(6), 3168–3176.

Rosenheck, K., & Doty, P. (1961). THE FAR ULTRAVIOLET ABSORPTION SPECTRA OF POLYPEPTIDE AND PROTEIN SOLUTIONS AND THEIR DEPENDENCE ON CONFORMATION. *Proceedings of the National Academy of Sciences*, 47(11), 1775–1785. <https://doi.org/10.1073/pnas.47.11.1775>

Ross, J. A., & Jameson, D. M. (2008). Time-resolved methods in biophysics. 8. Frequency domain fluorometry: applications to intrinsic protein fluorescence. *Photochemical & Photobiological Sciences: Official Journal of the European Photochemistry Association and the European Society for Photobiology*, 7(11), 1301–1312. <https://doi.org/10.1039/b804450n>

Sawai, H., Kawada, N., Yoshizato, K., Nakajima, H., Aono, S., & Shiro, Y. (2003). Characterization of the Heme Environmental Structure of Cytoglobin, a Fourth Globin in Humans †. *Biochemistry*, 42(17), 5133–5142. <https://doi.org/10.1021/bi027067e>

Schaberle, F. A., Nunes, R. M. D., Barroso, M., Serpa, C., & Arnaut, L. G. (2010). Analytical solution for time-resolved photoacoustic calorimetry data and applications to two typical photoreactions. *Photochemical & Photobiological Sciences: Official Journal of the European Photochemistry Association and the European Society for Photobiology*, 9(6), 812–822. <https://doi.org/10.1039/c0pp00025f>

Schuresko, D. D., & Webb, W. W. (1978). Carboxylation kinetics of hemoglobin and myoglobin: linear transient response to step perturbation by laser photolysis. *Biophysical Journal*, 24(1), 382–383. [https://doi.org/10.1016/s0006-3495\(78\)85390-9](https://doi.org/10.1016/s0006-3495(78)85390-9)

Sheftel, A. D., Mason, A. B., & Ponka, P. (2011). The long history of iron in the Universe and in health and disease. *Biochimica et Biophysica Acta*, 1820(3), 161–187. <https://doi.org/10.1016/j.bbagen.2011.08.002>

Shivapurkar, N., Stastny, V., Okumura, N., Girard, L., Xie, Y., Prinsen, C., Thunnissen, F. B., Wistuba, I. I., Czerniak, B., Frenkel, E., Roth, J. A., Liloglou, T., Xinarianos, G., Field, J. K., Minna, J. D., & Gazdar, A. F. (2008). Cytoglobin, the newest member of the globin family, functions as a tumor suppressor gene. *Cancer Research*, 68(18), 7448–7456. <https://doi.org/10.1158/0008-5472.can-08-0565>

Singh, S., Manda, S. M., Sikder, D., Birrer, M. J., Rothermel, B. A., Garry, D. J., & Mammen, P. P. A. (2009). Calcineurin activates cytoglobin transcription in hypoxic myocytes. *The Journal of Biological Chemistry*, 284(16), 10409–10421. <https://doi.org/10.1074/jbc.m809572200>

Smagghe, B. J., Sarath, G., Ross, E., Hilbert, J., & Hargrove, M. S. (2006). Slow Ligand Binding Kinetics Dominate Ferrous Hexacoordinate Hemoglobin Reactivities and Reveal Differences between Plants and Other Species†. *Biochemistry*, 45(2), 561–570. <https://doi.org/10.1021/bi0519021>

Steinbach, Peter J. (2012). Filtering artifacts from lifetime distributions when maximizing entropy using a bootstrapped model. *Analytical Biochemistry*, 427(1), 102–105. <https://doi.org/10.1016/j.ab.2012.04.008>

Steinbach, Peter J., Ionescu, R., & Matthews, C. R. (2002). Analysis of Kinetics Using a Hybrid Maximum-Entropy/Nonlinear-Least-Squares Method: Application to Protein Folding. *Biophysical Journal*, 82(4), 2244–2255. [https://doi.org/10.1016/s0006-3495\(02\)75570-7](https://doi.org/10.1016/s0006-3495(02)75570-7)

Steinbach, P.J. (1996). Two-dimensional distributions of activation enthalpy and entropy from kinetics by the maximum entropy method. *Biophysical Journal*, 70(3), 1521–1528. [https://doi.org/10.1016/s0006-3495\(96\)79714-x](https://doi.org/10.1016/s0006-3495(96)79714-x)

Steinbach, P.J., Chu, K., Frauenfelder, H., Johnson, J. B., Lamb, D. C., Nienhaus, G. U., Sauke, T. B., & Young, R. D. (1992). Determination of rate distributions from kinetic experiments. *Biophysical Journal*, *61*(1), 235–245. [https://doi.org/10.1016/s0006-3495\(92\)81830-1](https://doi.org/10.1016/s0006-3495(92)81830-1)

Storz, J. F., & Moriyama, H. (2008). Mechanisms of hemoglobin adaptation to high altitude hypoxia. *High Altitude Medicine & Biology*, *9*(2), 148–157. <https://doi.org/10.1089/ham.2007.1079>

Tangar, A., Derrien, V., Lei, R., Estevez, M. J. S., Sebban, P., Bernad, S., & Miksovska, J. (2019). Utility of fluorescent heme analogue ZnPPIX to monitor conformational heterogeneity in vertebrate hexa-coordinated globins. *Metallomics*, *11*(5), 906–913. <https://doi.org/10.1039/c8mt00332g>

Teale, F. W. J. (1959). Cleavage of the haem-protein link by acid methylethylketone. *Biochimica et Biophysica Acta*, *35*, 543. [https://doi.org/10.1016/0006-3002\(59\)90407-x](https://doi.org/10.1016/0006-3002(59)90407-x)

Tejero, J., Sparacino-Watkins, C. E., Ragireddy, V., Frizzell, S., & Gladwin, M. T. (2015). Exploring the mechanisms of the reductase activity of neuroglobin by site-directed mutagenesis of the heme distal pocket. *Biochemistry*, *54*(3), 722–733. <https://doi.org/10.1021/bi501196k>

Thuy, L. T. T., Thuy, T. T. V., Matsumoto, Y., Hai, H., Ikura, Y., Yoshizato, K., & Kawada, N. (2016). Absence of cytoglobin promotes multiple organ abnormalities in aged mice. *Scientific Reports*, *6*(1), 24990. <https://doi.org/10.1038/srep24990>

Totzeck, M., Hendgen-Cotta, U. B., Luedike, P., Berenbrink, M., Klare, J. P., Steinhoff, H.-J., Semmler, D., Shiva, S., Williams, D., Kipar, A., Gladwin, M. T., Schrader, J., Kelm, M., Cossins, A. R., & Rassaf, T. (2012). Nitrite regulates hypoxic vasodilation via myoglobin-dependent nitric oxide generation. *Circulation*, *126*(3), 325–334. <https://doi.org/10.1161/circulationaha.111.087155>

Trent, J. T., & Hargrove, M. S. (2002). A Ubiquitously Expressed Human Hexacoordinate Hemoglobin. *Journal of Biological Chemistry*, 277(22), 19538–19545. <https://doi.org/10.1074/jbc.m201934200>

Tsujino, H., Yamashita, T., Nose, A., Kukino, K., Sawai, H., Shiro, Y., & Uno, T. (2014). Disulfide bonds regulate binding of exogenous ligand to human cytoglobin. *Journal of Inorganic Biochemistry*, 135, 20–27. <https://doi.org/10.1016/j.jinorgbio.2014.02.011>

Uddin, R. G. E.-J. (2012). *The Use of Spectrophotometry UV-Vis for the Study of Porphyrins* (p. Ch. 6). IntechOpen. <https://doi.org/10.5772/38797>

Uzan, J., Dewilde, S., Burmester, T., Hankeln, T., Moens, L., Hamdane, D., Marden, M. C., & Kiger, L. (2004). Neuroglobin and Other Hexacoordinated Hemoglobins Show a Weak Temperature Dependence of Oxygen Binding. *Biophysical Journal*, 87(2), 1196–1204. <https://doi.org/10.1529/biophysj.104.042168>

Valeur, B. (2001). *Molecular Fluorescence*. 155–199. <https://doi.org/10.1002/3527600248.ch6>

Vallone, B., Nienhaus, K., Matthes, A., Brunori, M., & Nienhaus, G. U. (2004). The structure of carbonmonoxy neuroglobin reveals a heme-sliding mechanism for control of ligand affinity. *Proceedings of the National Academy of Sciences*, 101(50), 17351–17356. <https://doi.org/10.1073/pnas.0407633101>

Vetromile, C. M., Miksovská, J., & Larsen, R. W. (2011). Time resolved thermodynamics associated with ligand photorelease in heme peroxidases and globins: Open access channels versus gated ligand release. *Biochimica et Biophysica Acta*, 1814(8), 1065–1076. <https://doi.org/10.1016/j.bbapap.2011.01.009>

Voet, D., & Voet, J. G. (2010). *Biochemistry, 4th Edition*. J. Wiley & Sons.

Wakasugi, K., Nakano, T., Kitatsuji, C., & Morishima, I. (2004). Human neuroglobin interacts with flotillin-1, a lipid raft microdomain-associated protein. *Biochemical and*

Biophysical Research Communications, 318(2), 453–460.
<https://doi.org/10.1016/j.bbrc.2004.04.045>

Wakasugi, K., Nakano, T., & Morishima, I. (2003). Oxidized Human Neuroglobin Acts as a Heterotrimeric G α Protein Guanine Nucleotide Dissociation Inhibitor. *Journal of Biological Chemistry*, 278(38), 36505–36512.
<https://doi.org/10.1074/jbc.m305519200>

Wakasugi, K., Nakano, T., & Morishima, I. (2004). Association of Human Neuroglobin with Cystatin C, a Cysteine Proteinase Inhibitor †. *Biochemistry*, 43(18), 5119–5125.
<https://doi.org/10.1021/bi0495782>

Wang, W.-H., Lu, J.-X., Yao, P., Xie, Y., & Huang, Z.-X. (2003). The distinct heme coordination environments and heme-binding stabilities of His39Ser and His39Cys mutants of cytochrome b5. *Protein Engineering Design and Selection*, 16(12), 1047–1054. <https://doi.org/10.1093/protein/gzg134>

Weber, G., & Teale, F. J. W. (1959). Electronic energy transfer in haem proteins. *Discussions of the Faraday Society*, 27(0), 134. <https://doi.org/10.1039/df9592700134>

Weinacht, T. C., & Pearson, B. J. (2018). *Time-Resolved Spectroscopy*. 63–72.
<https://doi.org/10.1201/9780429440823-4>

Worsfold, Paul. J., & Zagatto, Elias. A. G. (2005). *Spectrophotometry | Overview* (P. Worsfold, A. Townshend, & C. Poole, Eds.; p. 5000). Elsevier.

Xu, J., Li, L., Yin, G., Li, H., & Du, W. (2009). Ligand orientation of human neuroglobin obtained from solution NMR and molecular dynamics simulation as compared with X-ray crystallography. *Journal of Inorganic Biochemistry*, 103(12), 1693–1701. <https://doi.org/10.1016/j.jinorgbio.2009.09.016>

Xu, J., Yin, G., Huang, F., Wang, B., & Du, W. (2009). Molecular dynamics simulation of a carboxy murine neuroglobin mutated on the proximal side: heme displacement and

concomitant rearrangement in loop regions. *Journal of Molecular Modeling*, 16(4), 759–770. <https://doi.org/10.1007/s00894-009-0581-3>

Yu, Z., Xu, J., Liu, N., Wang, Y., Li, X., Pallast, S., Leyen, K. van, & Wang, X. (2012). Mitochondrial distribution of neuroglobin and its response to oxygen-glucose deprivation in primary-cultured mouse cortical neurons. *Neuroscience*, 218, 235–242. <https://doi.org/10.1016/j.neuroscience.2012.05.054>

Zhang, S., Li, X., Jourd'heuil, F. L., Qu, S., Devejian, N., Bennett, E., Jourd'heuil, D., & Cai, C. (2017). Cytoglobin Promotes Cardiac Progenitor Cell Survival against Oxidative Stress via the Upregulation of the NFκB/iNOS Signal Pathway and Nitric Oxide Production. *Scientific Reports*, 7(1), 10754. <https://doi.org/10.1038/s41598-017-11342-6>

VITA

RUIPENG LEI

2014-present Ph. D. student (Biochemistry) Florida International University, FL
(GPA: 3.72)

2009-2012 B.S. (Biotechnology) Huaiyin Normal University, Huai an, Jiangsu

PUBLICATIONS AND SELECTED CONFERENCE PRESENTATIONS

Ren Y, Lai Y, Laverde EE, Lei R, Rein HL, et al. (2017) Modulation of trinucleotide repeat instability by DNA polymerase β polymorphic variant R137Q. *PLOS ONE* 12(5): e0177299.

Antonija Tangar; Vale´rie Derrien; Ruipeng Lei; Maria Jose Santiago Estevez; Pierre Sebban; Sophie Bernad and Jaroslava Miksovska. “Utility of fluorescent heme analogue ZnPPIX to monitor conformational heterogeneity in vertebrate hexa-coordinated globins”. *Metallomics*. 2019 May 22;11(5):906-913. doi: 10.1039/c8mt00332g.

Wen, Zhiwei; Tuttle, Paloma; Howlader, A. Hasan; Vasilyeva, Anna; Gonzales, Laura; Tangar, Antonija; Lei, Ruipeng; Laverde, Eduardo; Liu, Yuan; Miksovska, Jaroslava; Wnuk, Stanislaw. “Fluorescent 5-Pyrimidine and 8-Purine Nucleosides Modified with N-unsubstituted 1,2,3-Triazol-4-yl Moiety”. *The Journal of Organic Chemistry*. **2019** Mar 15;84(6):3624-3631. doi: 10.1021/acs.joc.8b03135. Epub 2019 Mar 6.

Yanhao Lai, Ruipeng Lei*, Yaou Ren, Yuan Liu. “Methods to Study Trinucleotide Repeat Instability Induced by DNA Damage and Repair”. *Methods Mol Biol*. 2019;1999:87-101. doi: 10.1007/978-1-4939-9500-4_5.

Judy L. Vasquez, Yanhao Lai, Thirunavukkarasu Annamalai, Zhongliang Jiang, Manqi Zhang, Ruipeng Lei, Zunzhen Zhang, Yuan Liu, Yuk-Ching Tse-Dinh, Irina U. Agoulnik. “Inhibition of base excision repair by natamycin suppresses prostate cancer cell proliferation”. *Biochimie*. 2020 Jan;168:241-250. doi: 10.1016/j.biochi.2019.11.008. Epub 2019 Nov 19.

*Co-first author

Jaroslava Miksovska, Ruipeng Lei, Sophie Bernad, Valerie Derrien. Distinct mechanism of oxygen and carbon monoxide interactions with heme protein. 62nd Biophysical society meeting, Feb 17-21, 2018, San Fransisco, CA.

Jaroslava Miksovska, Ruipeng Lei, Sophie Bernad, Valerie Derrien. Distinct mechanism of oxygen and carbon monoxide interactions with heme protein. 94th Florida Annual Meeting and Exposition (FAME) conference, May 3-5, 2018, Palm Harbor, FL.

Ruipeng Lei, David Butcher, Sophie Bernad, Valerie Derrien, Jaroslava Miksovska. Mutation of Residues in CD Loop and Distal Pocket Impact Protein Stability of Human Neuroglobin. 63rd Biophysical society meeting, Mar 02-06, 2019, Baltimore, MD.

Ruipeng Lei, David Butcher, Sophie Bernad, Valerie Derrien, Jaroslava Miksovska. Mutation of Residues in CD Loop and Distal Pocket Impact Protein Stability of Human Neuroglobin. ACS 2019 spring national meeting&Exposition, Mar 31-Apr 04, 2019, Orlando, FL.

Ruipeng Lei, David Butcher, Sophie Bernad, Valerie Derrien, Jaroslava Miksovska. Mutation of Residues in CD Loop and Distal Pocket Impact Protein Stability of Human Neuroglobin. 2019 Annual BSI Research Symposium, April 12, 2019, Miami, FL.

Ruipeng Lei, Maria Jose Santiago Estevez, Pierre Sebban, Sophie Bernad, Valerie Derrien, Jaroslava Miksovska. Study the Accessibility of the Heme Cavity In Hexacoordinate Globins By Using Fluorescent Heme Analog. 95th Florida Annual Meeting and Exposition (FAME) conference, May 9-11, 2019, Palm Harbor, FL.

Ruipeng Lei, David Butcher, Sophie Bernad, Valerie Derrien, Jaroslava Miksovska. Mutation of Residues in CD Loop and Distal Pocket Impact Protein Stability of Human Neuroglobin. FIUMASS event, July 19th, 2019, Miami, FL.

Ruipeng Lei, Maria Jose Santiago Estevez, Manuel Picon, Isa Sabir, Valerie Derrien, Sophie Bernad, Jaroslava Miksovska. Impact of the internal disulfide bond on the ligand migration in globin X. 64th Biophysical society meeting, Feb 15-19, 2020, San Diego, CA.